EVOLUTION OF ALLOYS AND RADIONUCLIDE SEQUESTRATION BY FIRST-PRINCIPLES CALCULATIONS

By

SHUBHAM PANDEY

A DISSERTATION PRESENTED TO THE GRADUATE SCHOOL
OF THE UNIVERSITY OF FLORIDA IN PARTIAL FULFILLMENT
OF THE REQUIREMENTS FOR THE DEGREE OF
DOCTOR OF PHILOSOPHY

UNIVERSITY OF FLORIDA

2020

To my family and friends

ACKNOWLEDGMENTS

Although, merely thanking the people as an acknowledgement would be an understatement, but I would first like to express my sincere appreciation to my advisor, Prof. Simon R. Phillpot. He has been a substance of genius who convincingly guided and encouraged me throughout my graduate study. His passion towards science has always kept me motivated. His great sense of humor, exuberance, patience with his students, and optimistic personality has made my graduate journey simplified and absolutely wonderful. His style of gradual progression towards any problem and encouragement to think independently has been invaluable. He has been immensely supportive, both professionally and personally, and I couldn't have asked for a better advisor than him.

I would like to thank my collaborators, Prof. Natalia Shustova, Prof. Scott Misture, Prof. Hui Wang, and all the other members of the EFRC-CHWM group, with whom I have got a chance to work on the interesting problem of nuclear waste sequestration. In particular, I feel indebted to Prof. Natalia Shustova and group, for their active collaboration and enthusiasm, and to also to have me over to South Carolina for two weeks to work closely with them. She is one of the most passionate and ambitious people I have met, and I feel fortunate to have worked with her. I would also like to thank Dr. D. S. Aidhy and group for their active collaboration on multiple projects which resulted in few publications. He has also been an inspiration for me to work hard and to be competitive.

I would like to thank my committee, Prof. Richard Hennig, Prof. Yong Yang, Prof. Michele Manuel, and Prof. Youping Chen. In particular, I am grateful to Prof. Richard Hennig to teach me quantum methods in computational materials science, which was a stepping stone towards my graduate study.

I would also like to thank the members of the FLAMES group, for their constant support and warm friendship. In particular, I would like to thank Michele Fullarton for her kindness, moral support, caring attitude, and for often baking some delicious cakes and sharing it with everyone. I would also like to thank Dr. Eugene Ragasa for his discussions on interesting scientific ideas, and Dr. Brian Demaske to help me with the project of MOFs. I would also like to thank Linyuan and Ximeng for organizing exciting Chinese Hotpot gatherings.

I would like to take this opportunity and thank friends from my Cricket group, Corry Cricket Club, who have been like a family away from home. Playing Cricket and socializing with them has been a great source of motivation for me.

This journey of my graduate life would not have been possible without the selfless support and love of my family. My parents gave me a strong foundation and have been very supportive of my dreams and ambitions. They have always let me make my own decisions and choose my career path independently. All my family, including my Grandfather, late Grandmother, Dad, and Mom have given me a comfortable upbringing and the right moral values. My sister and cousins have always been by my side and their constant support is invaluable. I am greatly indebted to all my family.

Finally, I would like to thank the Almighty for making this journey easy and worthwhile.

TABLE OF CONTENTS

page

LIST OF TABLES

LIST OF FIGURES

LIST OF ABBREVIATIONS

ATAT	Alloy Theoretic Automated Toolkit
CI-NEB	Climbing Image Nudge Elastic Band Method
DFT	Density Functional Theory
DOS	Density of States
GGA	Generalized Gradient Approximation
LDA	Local Density Approximation
MEP	Minimum Energy Path
MOF	Metal-Organic Framework
SCAN	Strongly Constraint and Appropriately Normed Semilocal Density Functional
SQS	Special Quasirandom Structure
VASP	Vienna Ab Initio Simulation Package

Abstract of Dissertation Presented to the Graduate School
of the University of Florida in Partial Fulfillment of the
Requirements for the Degree of Doctor of Philosophy

EVOLUTION OF ALLOYS AND RADIONUCLIDE SEQUESTRATION BY FIRST-PRINCIPLES CALCULATIONS

By

Shubham Pandey

May 2020

Chair: Simon R. Phillpot
Major: Materials Science and Engineering

Thermodynamic stability and kinetics in Cu-Au alloys are elucidated using first-principles calculations. In particular, the Au-rich compositions lying extremely close to the convex-hull are investigated to establish a structure-property relationship. Multiple metastable states were found to be superstructures of the layered L_{10} $Cu_{0.5}Au_{0.5}$ ground state. The effects of epitaxy on the ordered ground states of Cu-Au phases are examined with Au as the underlying substrate. The Cu-rich phases are found to destabilize, while the Au-rich phases remaining stable, depending on the growth plane. These results are related to the dealloying phenomenon and nucleation of Au-rich phases observed experimentally. Nudged Elastic Band calculations in both the ordered and disordered Cu-Au phases are performed to determine the activation energies for diffusion. The ordered phases show unique minimum energy paths due to uniform local environment of the species, while the disordered phases show a distribution of transition states, governed by the local bonding environments of diffusing species.

The high porosity, modularity, and synthetic diversity of metal-organic frameworks (MOFs) make them attractive candidate materials for selective sensing, separation, and sequestration of the radionuclides present in the nuclear wastes. Density Functional Theory

(DFT) calculations are used to determine the favorability of ion-exchange at the metal node of Tc, U, Th, Am, and Cm in Zr-, U-, and Th-based MOF clusters. A range of DFT methods, including several exchange-correlation functionals, DFT+*U* technique, relativistic effects, and magnetic effects are employed to establish robustness in the results. Various reference states of ions including the vacuum, continuum water medium and explicit water molecules surrounding ions are also explored. Substitution of Tc, Am, Cm, and Th is found to be energetically favorable in all the MOFs using ions surrounded by explicit water molecules as a reference.

While the fundamental thermodynamic properties, such as the substitution energies determine the favorability of isolation of a radionuclide in the MOF, the electronic properties of MOFs are equally important to understand the role of *d*-, and *f*-electrons in the actinides and transition metals. DFT calculations are performed to investigate the electronic structures of Zr-, Th-, and U-MOFs, including their electronic band structures and, where appropriate, their magnetic properties. Various DFT methods including DFT+*U*, collinear spin-polarization, spin-orbit coupling, and different flavors of exchange-correlation functionals are employed to assess the robustness to the specific exchange-correlation functional. Unlike the Zr-, and Th-MOFs, the U-MOF is found to be sensitive to electron localization and spin; hence we explore the magnetic structure of the U-MOF in further detail.

CHAPTER 1
INTRODUCTION

1.1 General Overview

Simulation, defined as computational physics-based modeling, has emerged as a complementary approach to theory and experiments for examining physical systems. Such modeling has become a fundamental tool for scientific research in many disciplines, including materials science [1]. Materials modeling can be classified into different levels in a *multiscale hierarchy* depending on the length and time scales as illustrated in Fig. 1-1. *Ab initio* models based on quantum mechanics are the lowest in the hierarchy with typical length and time scales of 0.1–10 nm and 0.1–100 ps respectively. Atomistic methods such as molecular dynamics (MD) and Monte Carlo (MC) are the next level in the hierarchy above *ab initio* models, with length scales of 1–1000 nm and time scales of about 1ps–10 ns. Mesoscale approaches, such as dislocation dynamics and phase-field methods, the next higher level, cover a length scale of about 10 nm–10 μm and time scales of 1 ns–100 ns. Continuum mechanics lies at the top of the hierarchy with even longer scales. The lower bounds of these models are determined by the physical approximations, while the upper bounds are determined by computational limitations [1].

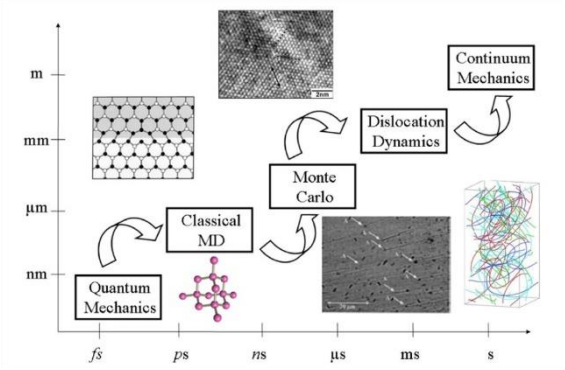

Figure 1-1. Hierarchy in length and time scales of materials models. Five primary models are presented. (Adapted from G. Makov et al., Modelling Simul. Mater. Sci. Eng. 17, 2009 [1])

Materials science, being an interdisciplinary field, is related to condensed matter physics and chemical physics, both of which also utilize modeling approaches successfully. The larger scales of modeling, such as physics-based continuum mechanics and mesoscale modeling can conveniently model dislocation stress fields and associated interactions at this limit. The finite element method can be applied to model the deformation of metals at the mesoscale and can thus be used to study the microstructure and texture evolution. However, accurate description of many fundamental materials' properties like ground state thermodynamics, migration barriers for diffusion, and electronic bandstructure, require quantum mechanical approaches. Although, MD simulations can describe some of these fundamental properties, they rely on classical potentials which often constructed with input from quantum mechanical calculations. Electronic structure-based *ab initio* modeling automatically captures bond breaking and formation, atomic rearrangements and chemical specificity which are not captured with high fidelity in the larger scales of modeling. The simplest *ab initio* methods involve computations of electronic orbitals, where the instantaneous Coulombic electron-electron repulsions are specifically not taken into account, and only the mean field (average) effects are included. Sometimes, a distinction is made between first principles and *ab initio* methods, such as the Hartree-Fock method, and empirical or semiempirical methods such as Density Functional Theory (DFT). The *ab initio* methods are guided by the variational principle which guarantees an approximate solution whose energy is an upper bound to the ground state energy. By contrast the empirical methods require an experimental parameterization and thus their accuracy is less systematically controlled [2]. However, in practice, the above difference is not very significant for materials modeling because, both approaches lead to valuable approximate solutions for any reasonably complex system, and

the *ab initio* solutions are not necessarily superior to those obtained using the more empirical approaches.

In this work, we apply both empirical/semi-empirical DFT and Hartree-Fock based *ab initio* methods, to study the thermodynamics, lattice diffusion, band-structure, magnetic properties, electron localization in a bimetallic alloy and in selected Metal-Organic Frameworks (MOFs). The ground state ordered phases of the Cu-Au system are explored using DFT calculations and a structure-energy relation is established. The ordered phases are also modeled on Au as a substrate, to investigate the effects of epitaxy. Transition state theory is then used to calculate the migration barriers for both Cu and Au in the lattice. Disordered phases are also modeled to investigate kinetics in the solid-solution of Cu-Au. All these findings are related to experimental results on the thermodynamic and kinetic factors, that govern the presence of any phase in the experiments. DFT calculations are also performed on the MOF systems, to predict the favorability of isolation of five important radionuclides (Tc, U, Th, Am and Cm) at the metal nodes of MOFs. A systematic hierarchy of DFT methods including different flavors of exchange-correlation (XC) functionals, van-der-Waals (vdW) interactions, electron localization effects, spin-polarization effects, relativistic effects, and hydration effects are explored to establish robustness in the results. Similarly, a range of DFT methods are applied to systematically investigate the electronic structure of transition metal-, and actinide-based MOF systems. Electron localization, magnetic ordering, and spin-polarization are found be critical for the accurate prediction of band gaps for the U-MOFs. All these thermodynamic and the electronic structure results are also benchmarked against the experimental findings, where available.

1.2 Motivation of Problems

1.2.1 MOFs For Radionuclide Sequestration

Nuclear energy is one of the major sources of electricity generation, which benefits from zero emission of greenhouse gases. The nuclear power plants contribute almost 11% of the World's electricity. The generation of nuclear power is achieved through fission, which involves splitting of ^{235}U atoms from an impact by slow neutrons (n). An example reaction is shown as follows,

$$^{235}_{92}\mathrm{U} + {}^{1}_{0}\mathrm{n} \rightarrow {}^{141}_{56}\mathrm{Ba} + {}^{92}_{36}\mathrm{Kr} + 3{}^{1}_{0}\mathrm{n} + 200\ \mathrm{MeV} \quad (1\text{-}1)$$

in which ^{235}U forms two smaller atoms (Ba and Kr), which are unstable, and these smaller atoms include fission products and minor actinides which are highly radioactive [3].

The scientific and technological challenges for the management of nuclear waste byproducts of nuclear power generation and medical isotope production have been one of the major barriers for the rapid development of nuclear energy utilization. These challenges arise because of the extreme complexity of the spent nuclear fuel which comprises of more than 400 radionuclides (representing more than 40 elements) [4]. The closed nuclear fuel cycle is currently a concept widely accepted by most countries to minimize the volume of radioactive wastes and maximize the use of fissile materials. This requires the recycling and elimination of the actinides and some fission products with long-term radioactivity in the used nuclear fuel (Fig. 1-2). Generally, a Plutonium and Uranium Reduction EXtraction (PUREX) process is used to recycle uranium and plutonium. Minor actinides like Am and Cm can also be separated using soft ligands containing sulfur or nitrogen, driven by the solvent extraction technique [5–7]. These actinides are then sent to an accelerator driven system-based reactor for their transmutation to short-lived or stable isotopes [8]. Removal of other hazardous radionuclides like ^{137}Cs and ^{90}Sr

can be achieved by macrocyclic supramolecular-based extracting agents or by inorganic ion-exchange materials [4,9,10]. The anionic exchange resin has proved to be an effective scavenger for several anionic radionuclides like $^{99}TcO_4^-$ [11].

Although multiple feasible techniques have been developed for the purpose of radionuclide isolation and separation, considerable improvement is still required. Some of the obvious drawbacks of the solvent extraction technique are third phase formation, use of volatile and toxic solvents, slow sorption rate and poor stability of traditional ion-exchange resins under a strong radiation field, and low uptake capacity of the inorganic ion-exchange materials under highly acidic conditions. Thus, a fundamental understanding of potential isolating material systems is required.

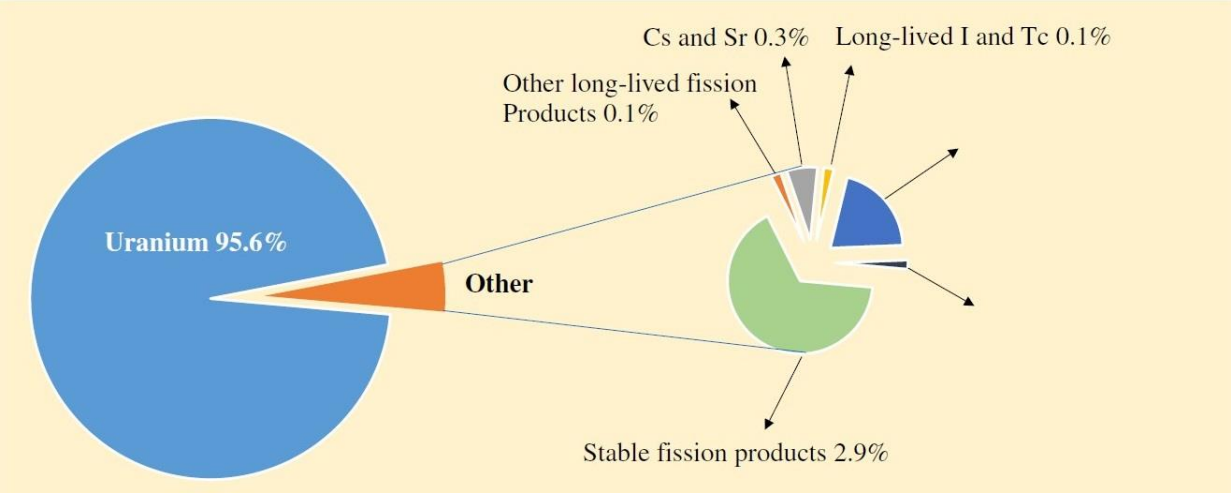

Figure 1-2. Chemical composition of the used nuclear fuel, showing fission products. (Adapted from the book by Sujit K. Ghosh, 2019. Metal-Organic Frameworks for Environmental Applications (page 356, Fig. 11.1). Elsevier. [4]).

Metal-Organic Frameworks (MOFs) are a class of nano-porous materials, consisting of an assembly of functional organic linkers and metal nodes [12]. MOFs are characterized by high specific surface areas, tunable pore diameter, and easy postmodification, all of which endows them with unique performances in catalysis, gas separation, adsorption, optical and biomedical

applications [13–16]. Recently, interest has emerged for utilization of MOFs for radionuclide separation as well [17–20]. In particular, since the rise of third generation of MOFs (soft porous crystals) there has been development of MOFs for applications based on host-guest chemistry [21]. Their ability to have guest-responsive structural dynamics has further motivated their capacity to operate as functional solids with a high precision and selectivity of guest recognition and accommodation response.

The radioactive species in a nuclear fuel cycle can be categorized into three groups: (1) cationic radionuclides, such as, $^{137}Cs^{+}$, $^{90}Sr^{2+}$, $^{232}Th^{4+}$ and $^{238}UO_2^{2+}$; (2) anionic radionuclides, such as, $^{99}TcO_4^{-}$, $^{129}I^{-}$, $^{79}SeO_3^{2-}$ and $^{79}SeO_4^{2-}$; and (3) gas phase radionuclides, such, ^{133}Xe, ^{85}Kr, and $^{129}I_2$. Strong and specific interactions between the host framework and guest radionuclides are highly desirable to achieve a reasonable amount of uptake of a given radionuclide. These include electrostatic interactions, hydrogen bond interactions, and hydrophobic interactions. The design strategies for uptaking into MOFs depends on the unique coordinating behaviors of different types of radionuclides. For example, for efficient removal of cationic radionuclides, a framework with a net negative charge (Fig. 1-3(a)) is required to achieve strong electrostatic interactions. Additionally, chelating groups such as -COOH, -PO_3H_2. can be implanted into the framework to enhance the coordinating ability towards high-valent cationic radionuclides. Similarly, anionic radionuclides can be effectively isolated by those MOFs with net positive charge on the extended framework (Fig. 1-3(b)). Moreover, the hydrogen atoms present in the organic ligands are critical for the formation of dense hydrogen bonds, thus contributing to the host framework/anion interaction. The pore size of the MOFs largely determines the separation properties for the cases of gaseous radionuclides uptake, especially for the inert noble gases, ^{133}Xe and ^{85}Kr. Suitable functionalization with reactive and

polarizable groups, nanoparticles and open metal sizes can further improve the separation factors or sequestration ability of the MOFs [22,23].

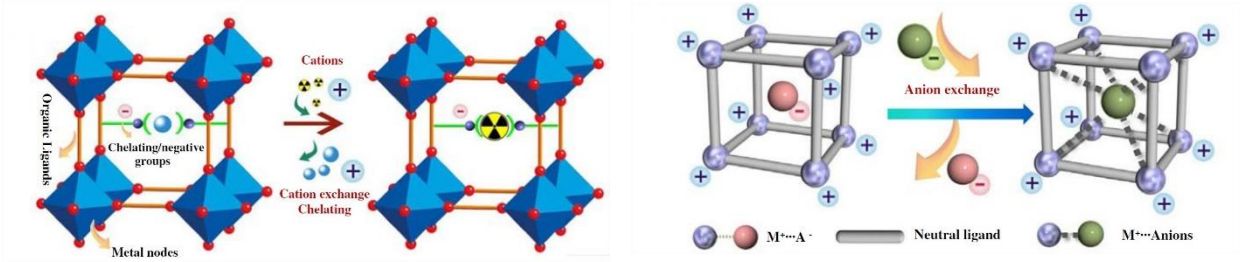

(a) **(b)**

Figure 1-3. Design principles of MOFs for sequestering (a) cationic (b) anionic radionuclides. (Adapted from the book by Sujit K. Ghosh, 2019. Metal-Organic Frameworks for Environmental Applications (page 357, Fig. 11.2). Elsevier. [4])

Uranium is most commonly present in the radioactive waste stream as UO_2^{2+}, which needs to be separated from natural water systems because of its combined radiotoxicity and chemotoxicity. The uranium extraction from seawater also contributes to the need for uranium sorbents [24,25]. So far, more than 20 MOF systems have been analyzed for their uptake capabilities of UO_2^{2+}. The use of MOFs for UO_2^{2+} extraction from aqueous solution was reported by Lin et al. [26]. Postmodification of MOFs with external ligands can immensely enhance their uptaking capabilities. For example, a high sorption capacity of 217 mg g^{-1} of UO_2^{2+} was observed with the UiO-68 MOF after it was covalently modified with phosphorylurea groups [26]. A critical weakness of MOFs is their limited stability in water. The radioactive waste containing uranium is highly acidic in some cases, and therefore it is extremely challenging to synthesize MOF sorbents to sequester UO_2^{2+} from highly acidic solutions.

The investigation of thorium (^{232}Th) separation by solid sorbent materials receives less attention as compared to uranium, as the fissile material in most current nuclear reactors is uranium rather than thorium. However, thorium is more abundant than uranium in nature and is

emerging for use as a core part of molten salt reactors. Thorium also exists as intergrowths with earth elements in the ores, and thus it needs to be removed from rare earth waste residues to avoid radioactive pollution during earth mining. The most stable oxidation state of thorium is Th(IV) which can also serve as a relevant surrogate for transuranic cations Np(IV) and Pu(IV), providing valuable knowledge on proper treatment of these highly radiotoxic radionuclides. The first case of Th(IV) sequestration by MOFs from an acidic solution was reported by Shi et al. [27]. Their findings indicate a decrease in pore volumes and specific surface areas with the attachment of carboxyl groups onto the UiO-66 MOF, however significantly improving the sorption properties toward Th(IV).

The primary anionic radionuclides in radioactive wastewaters are $^{99}TcO_4^-$, $^{129}I^-$, $^{79}SeO_3^{2-}$ and $^{79}SeO_4^{2-}$, all of which have long-term radioactivity. For example, ^{99}Tc has a half-life of 211,000 years. These anions have substantial solubility in aqueous solutions and most of them cannot be efficiently blocked by natural minerals, thus resulting in high mobility in the environment. Although there have been cationic framework materials reported to be effective for capture of anionic contaminants, such materials have limited sorption capacity [28]. Ion-exchange resins exhibits high sorption capacity and excellent distribution coefficients for radioactive anions; however, they have slow sorption kinetics and are unstable under high basicity and radiation. Numerous cationic MOFs have been reported for the isolation of anionic pollutants, but only few have been used for the removal of radioactive $^{99}TcO_4^-$. ReO_4^- is reported to be an excellent surrogate for TcO_4^- for the sorption or ion-exchange process. An example of ReO_4^- uptake by a MOF (SLUG-21) has been reported by Oliver et al. [29], with a high sorption capacity of 602 mg g^{-1}.

In summary, MOFs exhibit tunable porosity, ultrahigh surface area, and flexible postmodification, equipping them with outstanding properties to effectively sequester radioactive wastes. With the development of immense computational power and optimized simulation algorithms, quantum mechanical simulations can be initially used to establish the structure-property relationships in MOFs. In this work, Zr-, U-, and Th-based MOFs will be investigated for their favorability of ion-exchange of radionuclides such as Tc, U, Th, Am and Cm.

1.2.2 Nanoparticles for Waste Immobilization

Metallic nanoparticles can be classified as either monometallic (single elements), bimetallic (two different metallic elements) or multimetallic (more than two different elements). Bimetallic or multimetallic nanoparticles usually have enhanced stability compared to their monometallic counterparts [30–32]. The bimetallic and multimetallic nanoparticles can adopt a variety of structural architectures, such as solid-solution alloys, core–shell structures, and intermetallic compounds [33,34]. The concept of nanoparticles to be used as a waste form aims to optimize such systems structurally, architecturally and compositionally, to contain highly mobile elements, such as ^{137}Cs and ^{99}Tc, thereby suppressing their leaching and avoiding their volatilization. The development of such nanoparticles as a stable and processable waste-form, requires an understanding of the science underlying their formation and stability. Surrogates can be used in the initial stages to strategically work out the fundamental science, and eventually synthesizing the new waste-forms by incorporating the mobile radionuclides.

The nuclear fission generated nuclear wastes are composed of a wide variety of elements, many of which are transition metals that are vulnerable to oxidative etching under an environment accessible by water, oxygen, acids or salts. Oxidation of metal species like Tc and I, can trigger leaching of radionuclides from their storage matrices to the environment, which is a

serious challenge to nuclear waste processing, storage and management [35]. Thus, the structural robustness and architectural tunability of multimetallic nanoparticles can be utilized to accommodate multiple radionuclides in the same nanoscale body, through which enhanced stability and processability can be achieved. The issue of miscibility of metals needs to be explored to gauge the solid solubility in nanoparticles, which can range from partial to full miscibility.

The formation of bimetallic or multimetallic nanoparticles containing radionuclides like Tc, Cs and Re is a central interest. In the model systems such as Cu-Au nanoparticles, [32,36,37] alloying can occur well below the elemental melting point. Also, their low temperature processing is more efficient which can avoid the problem of the loss of volatile radioisotopes. Such simple systems can be first investigated to lay the fundamentals of nuclear waste storage in nanoparticles.

The reduced length scale of nanoparticles makes them convenient for study using computational simulations at the atomic scale. In particular, DFT is a very powerful tool to probe the effects of epitaxial strain on the stability of formation of alloys, and to model diffusion in the alloys and across the interfaces. DFT structure optimizations can also be integrated with pair distribution functions (PDF) and X-ray diffraction (XRD) measurements, to understand the microstructure, and local and average atomic structures of alloy nanoparticles better.

1.3 Outline

This dissertation is organized as follows. Chapter 2 discusses the various DFT methods and their applications to the calculations performed in this work. Chapter 3 discusses the thermodynamics and kinetics of the bimetallic Cu-Au system. The focus is to investigate the phase diagram of Cu-Au, particularly the Au-rich region, where numerous phases lie close to the

convex-hull, and thus to characterize these phases to establish a structure-property relationship. Epitaxial calculations on Au as a substrate are also discussed in this chapter and related to experimental observations. Chapter 3 also discusses the kinetics of Cu-Au ordered and disordered alloys in terms of migration barriers and activation energies for diffusion. Chapter 4 discusses the thermodynamics of ion-exchange of radionuclides in MOFs, using various DFT methods. The radionuclides discussed are Tc, Th, U, Am, and Cm. Different reference states of the participating ions (vacuum, continuum water media and hydrated ions) are also discussed. The favorability of ion-exchange is then related to the available experimental results. Chapter 5 discusses a DFT hierarchy to establish electronic structures of MOFs. DFT methods including, DFT+*U*, spin-polarization, relativistic effects and hybrid XC-functionals are employed to thoroughly investigate the bandstructure of MOFs. Various magnetic configurations of the magnetic U-MOF are investigated for their relative stabilities and band gaps, using two different levels of XC-functionals. The origin of band gap in MOFs is also discussed by considering truncated models of the extended MOF structures. Chapter 6 discusses band-gap engineering in MOFs, by modifying their metal nodes and organic linkers connecting metal nodes, and extension of a metal node. Chapter 7 presents a collective summary of results and discusses ideas for future work.

CHAPTER 2
SIMULATION METHODOLOGY

Thermodynamics and diffusion mechanisms in Cu-Au alloys will be investigated using first-principles DFT calculations. The structures of disordered Cu-Au alloys are modeled using Speical Quasirandom Structures (SQS). The ion-exchange and electronic structures of MOFs are also modeled in DFT calculations using two different suites of basis sets, plane-wave and orbital basis sets.

2.1 Density Functional Theory

Density functional theory (DFT) is a quantum mechanics method, which is presently the most successful approach to compute the electronic structure of extended matter. The applicability of DFT ranges from atoms, molecules and solids, to nuclei and quantum fluids such as superconductors. The original formulation of DFT provides the ground state properties of a system, utilizing the concept of electron density. Most approaches in solid state physics and quantum chemistry are ultimately based on the time-independent, non-relativistic Schrödinger equation, as shown in Equation 2-1 below,

$$\widehat{H}\Psi_i\left(\vec{x}_1, \vec{x}_2, \dots, \vec{x}_N, \vec{R}_1, \vec{R}_2, \dots, \vec{R}_M\right) = E_i\Psi_i\left(\vec{x}_1, \vec{x}_2, \dots, \vec{x}_N, \vec{R}_1, \vec{R}_2, \dots, \vec{R}_M\right) \quad (2\text{-}1)$$

where $\widehat{H}$ is the Hamiltonian for a system consisting of M nuclei and N electrons, Ψ_i is the eigenstate wavefunction and E_i is the eigenvalue.

The nuclei move much slower than the electrons due to their heavy masses, and thus, the electrons can be considered as moving in a field of fixed nuclei. This leads to the first key approximation towards understanding quantum mechanics: in the Born-Oppenheimer approximation [38] according to which the nuclear kinetic energy is zero and the nuclear potential energy has a time dependent value. This is a result of the assumption that the electron

wavefunctions are always equilibrated with respect to the nucleus. The reduced electronic Hamiltonian, $\hat{H}_{elec}$, can be expressed as follows as per the above approximation,

$$\hat{H}_{elec} = \left[-\frac{\hbar^2}{2m_e} \sum_i^N \nabla_i^2 + \sum_{i,I} \frac{Z_I e^2}{|r_i - R_I|} + \frac{1}{2} \sum_{i \neq j} \frac{e^2}{|r_i - r_j|} \right] = \hat{T} + \hat{V}_{Ne} + \hat{V}_{ee} \tag{2-2}$$

where, the subscripts i and j denote the N electrons in the system, and I denote the nuclei in the system. m_e is the mass of electron, and Z_I is the atomic number of the nuclei. $\vec{r_i}$ and $\overrightarrow{R_I}$ are spatial coordinates of the electrons and nuclei, respectively. The Hamiltonian, $\hat{H}_{elec}$, in Eq. 2-2 basically consists of three terms. The first term represents the kinetic energy, $\hat{T}$, of the of the electrons. The second term represents the electrostatic interaction between electrons and nuclei, $\hat{V}_{Ne}$. The third term represents the repulsive potential acting between two electrons, $\hat{V}_{ee}$. The equations above are expressed in terms of wavefunction, which is not an observable quantity by itself. The dependence of the Hamiltonian on the total number of electrons suggest that a useful physical observable would be electron density. The electron density, ρ, when integrated over all space, gives the total number of electrons, N, as follows,

$$N = \int \rho(\mathbf{r}) d\mathbf{r} \tag{2-3}$$

The electron density $n(r)$ can be defined as the probability of finding an electron within a given volume, at a particular position in space, and is expressed as,

$$n(r) = \sum_i \Psi_i^* (r) \Psi_i(r) \tag{2-4}$$

where, Ψ_i^* is the complex conjugate of the wavefunction Ψ_i.

2.1.1 Hohenberg and Kohn Theorems

The foundation of DFT lies in the two Hohenberg-Kohn theorems; the Existence Theorem and the Variational Theorem [39]. The Existence Theorem states that the external potential v_{ext} of an *N*-electron system is a unique functional of the ground state electron density

n_0. In the uniform electron gas, the external potential is the uniformly distributed positive charge, while in a molecule, the external potential is the attraction to the nuclei. Thus, the total energy can now be expressed as follows,

$$E[\rho] = E_{Ne}[\rho] + T[\rho] + E_{ee}[\rho] \tag{2-5}$$

The Variational Theorem states that, the functional that delivers the ground state energy of the system, delivers the lowest energy if and only if the input density is the true ground state density, i.e., $E_0 \leq E[\tilde{\rho}]$. This means that, for any candidate density $\tilde{\rho}$, which satisfies the necessary boundary conditions, the energy obtained from the functional of Eq. 2-5 represents an upper bound to the true ground state energy E_0.

2.1.2 Kohn-Sham Equations

Kohn and Sham realized that the solution to the ground state energy would be considerably simpler if the Hamiltonian operator were one for a system of *non-interacting electrons*. Such a Hamiltonian can be expressed as a sum of one-electron operators, has eigenfunctions that are Slater determinants of the individual one-electron eigenfunctions, and the obtained eigenvalues are simply the sum of the one-electron eigenvalues. The Kohn-Sham equations [40] can be expressed as follows,

$$\left[-\frac{\hbar^2\nabla^2}{2m} + v_{ext}(\boldsymbol{r}) + v_H(\boldsymbol{r}) + v_{xc}(\boldsymbol{r})\right]\phi_i(\boldsymbol{r}) = \varepsilon_i\phi_i(\boldsymbol{r}) \tag{2-6}$$

where, ϕ_i are the single particle orbitals of the non-interacting system. The Hartree potential $v_H = e^2 \int \frac{n(r)}{|r-r'|} d^3r'$ represents the Coulomb repulsion between the particles. The non-classical corrections to the electron-electron repulsion energy are contained in the exchange-correlation potential $v_{xc} = \delta E_{xc}[n]/\delta n$.

The Kohn-Sham DFT (KS-DFT) is the most popular electronic structure method because of its computational efficiency and reasonable accuracy. The ground-state total energy and

electron density would be delivered in the exact form by KS-DFT if the exact exchange-correlation energy were given. However, the exchange-correlation energy, E_{xc}, is not known and has to be approximated [41–43]. The next section discusses various approximations to exchange-correlation energy.

2.1.3 Exchange-Correlation Functionals

One of the approaches to KS-DFT is the development of approximate functionals from first principles which incorporates known exact-constraints. All physical properties will themselves come out accurately if enough constraints are satisfied. To impose the maximum number of constraints on a functional, it becomes important to expand the list of its local ingredients beyond the electron density, and thus to include other quantities constructed from the KS orbitals and their derivatives. A hierarchy of density functionals based on the type of these ingredients has been established. "Jacob's ladder" [42] begins with the Hartree level of theory and ascends to levels that have chemical accuracy, which is generally considered to be errors of less than 1 kcal/mol. An illustration of this hierarchy is shown in Fig. 2-1.

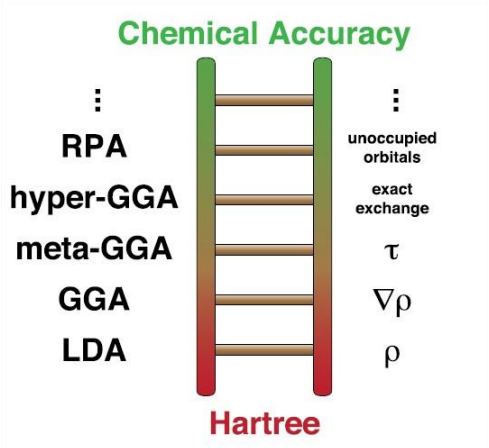

Figure 2-1. Jacob's ladder framework describing the different levels of sophistication of E_{xc}. (Adapted from E.B. Issacs et al., Phys. Rev. Materials 2, 063801, 2018 [44]).

The first three rungs of "Jacob's ladder" can be represented by,

$$E_{xc}[n_\uparrow, n_\downarrow] = \int d^3\, r\; n\; \varepsilon_{xc}\left(n_\uparrow, n_\downarrow, \nabla_{n_\uparrow}, \nabla_{n_\downarrow}, \tau_\uparrow, \tau_\downarrow\right) \tag{2-7}$$

where, $n_\uparrow$ and $n_\downarrow$ are the electron spin densities and ε_{xc} is the exchange-correlation energy density per volume. $n(\mathbf{r}) = n_\uparrow(\mathbf{r}) + n_\downarrow(\mathbf{r})$ is the total density, and $\tau_\sigma(\mathbf{r}) = \sum_i^{occup} \frac{1}{2} |\nabla \Psi_{i\sigma}(\mathbf{r})|^2$ is the kinetic energy density for the occupied KS orbitals $\Psi_{i\sigma}(\mathbf{r})$. These KS orbitals are the nonlocal functionals of the density $n_\sigma(\mathbf{r})$. The first rung, local spin density approximation (LSDA) [40,45–47], is obtained by dropping the ∇_{n_σ} and τ_σ dependencies in Eq. 2-7. The LSDA approximation is just an extension of the local density approximation (LDA), with distinct up-, and down-spin densities are The LDA is derived to be exact for any uniform electron gas and tends to minimize the inhomogeneity of the electron densities of real materials, however, is known to overestimate the strengths of all bonds near equilibrium.

The generalized gradient approximation (GGA) [41,48,49] , the second rung, was then developed by dropping only the τ_σ dependence in Eq. 2-7, which softens the bonds. The GGA cannot be accurate for structures and energies simultaneously, depending on how the electron density gradient is built [50]. Thus, it suffers from the limitation of not satisfying all the known exact constraints appropriate to a semi-local functional, where the exchange-correlation energy is systematically evaluated as a single integral over three-dimensional space. For example, the GGA cannot simultaneously satisfy the slowly varying density limit for extended systems and the tight lower bound on the exact exchange energy of single-orbital systems and still deliver accurate exchange energies [43]. Among the GGA functionals, such as, Perdew-Wang91 (PW91) [47], Perdew-Burke-Ernzerhof (PBE) [41], AM05 [51,52], the PBE scheme gives a balanced description for structures and energies, and generally a significant improvement over LDA.

The third rung of the ladder, the meta-GGA methods, utilizes all the ingredients of Eq. 2-7. Introduction of the kinetic energy density within the meta-GGAs, circumvents the dilemma of

"structure or energy" as in the case of GGAs. The kinetic energy density for a uniform electron gas is represented as, $\tau_\sigma^{unif}(\mathbf{r}) = (\frac{3}{10})(3\pi^2)^{2/3}n^{5/3}$, and for single-orbital systems, $\tau_\sigma^W(\mathbf{r}) = |\nabla n_\sigma|^2/8n_\sigma$, which is known as the von Weizsäcker kinetic energy density for real orbitals [42]. Using the dimensionless variable $\alpha = (\tau - \tau^w)/\tau^{unif}$, the meta-GGAs can identify the slowly varying densities ($\alpha \sim 1,$ for metallic bonds) and single-orbital systems ($\alpha = 0,$ for covalent single bonds) and thus reduce to the various GGAs for these two different limits [53–55]. Some of the meta-GGAs, such as, Tao-Perdew-Staroverov-Scuseria (TPSS) [42] and M06L [56] utilizes other dimensionless variables built from τ. However, they show strong numerical instability for single bonds and miss the van der Waals interaction, due to the inability of such variables to distinguish among different chemical bonds.

The Strongly Constrained and Appropriately Normed (SCAN) meta-GGA [55] has the advantage over other meta-GGAs, of satisfying all the 17 constraints appropriate to a semilocal functional. Moreover, the SCAN meta-GGA uses the appropriate norms, which sufficiently localizes the exact exchange-correlation hole near its electron (for example, the hydrogen atom). The key difference between SCAN and other meta-GGAs on the other hand, and the PBE functional on the other, arises from the exchange enhancement factor used in constructing their exchange and correlation energies. The exchange energy for spin-density n, can be represented as,

$$E_x[n] = \int d^3r n\varepsilon_x^{unif}(n)F_x(s,\alpha) \tag{2-8}$$

where, $\varepsilon_x^{unif} = -(\frac{3}{4\pi})(3\pi^2 n)^{1/3}$ is the exchange energy per particle of a uniform electron gas, $F_x(s,\alpha)$ is the exchange enhancement factor, and $s = |\nabla n|/[2(3\pi^2)^{\frac{1}{3}}n^{\frac{4}{3}}]$ is a dimensionless density gradient. The F_x for SCAN follows the strongly tightened bound limit of $F_x \leq 1.174$ [57]

for all α, while the F_x for other meta-GGAs (TPSS and revised-TPSS) and the GGA-PBE is 1.804 [55]. The semi-local feature in the computation of meta-GGAs also makes them much more computationally efficient than hybrid GGAs, which form the fourth rung of the ladder.

The hybrid functionals forming the fourth rung of the ladder, make use of either full or short-range (SR) Hartree-Fock (HF) exchange. Their exchange-correlation can be represented as.

$$E_{xc}^{hybrid} = E_{xc}^{SL} + \alpha_x\left(E_x^{(SR-)HF} - E_x^{(SR-)SL}\right) \tag{2-9}$$

where, E_{xc}^{SL} is the semi-local approximation, $\alpha_x(\in [0,1])$ is the fraction of HF exchange energy $E_x^{(SR-)HF}$ which is a double integral and can be represented as follows,

$$E_x^{(SR-)HF} = -\frac{1}{2}\sum_{i=1}^{N}\sum_{j=1}^{N}\delta\sigma_i\sigma_j \iint \Psi_i^*(\mathbf{r})\Psi_j(\mathbf{r})v(|\mathbf{r}-\mathbf{r}'|)\Psi_j^*(\mathbf{r}')\Psi_i(\mathbf{r}')d^3r d^3r' \tag{2-10}$$

where, the indices i and j run over the occupied orbitals and v is the Coulomb potential. Some of the most commonly used hybrid functionals are the screened hybrid functional of Heyd, Scuseria, and Ernzerhof (HSE) [58,59], B3LYP [60], and PBE0 [61]. These hybrid functionals were designed to minimize the electron delocalization effects in many *d*-, and *f*-electron systems, so as to accurately describe the electronic structure of a material with respect to the experiments [59]. In addition to the hybrid functionals, an approximation of adding a Hubbard term to the Hamiltonian, called the DFT+*U* method, was also developed to overcome the delocalization effects. This DFT+*U* approximation is described in the next section.

2.1.4 DFT+*U* Approximation

While conventional DFT has been successful in many cases, it often fails for the treatment of insulating states of compounds containing partly filled *d*-, and *f*-shells. For example, the conventional LSDA solutions incorrectly predict that uranium dioxide is a metal, where the uranium ions contain partly filled *f*-shells [62]. The band theory fails when the inter-site quantum

hopping (tunneling) of electrons is suppressed by the on-site Coulomb repulsion between electrons [63]. The motion of electrons in a crystal becomes strongly correlated, when the amplitude of hopping is comparable or smaller than the Hubbard *U* term (where, *U* is the energy of repulsion between electrons occupying the same atomic shell). The LSDA+*U* approximation was then developed to describe the Coulomb interaction between 5*f* electrons of uranium ions in UO_2 or between 3*d* electrons of nickel ions in NiO [63,64].

To realistically describe the Coulomb interaction between *f* or *d* electrons, the orbital degeneracy of the *f*-, and *d*-shells is taken into account, and the following Hamiltonian is used,

$$\hat{H} = \frac{\bar{U}}{2} \sum_{m,m',\sigma} \hat{n}_{m,\sigma} \hat{n}_{m',-\sigma} + \frac{(\bar{U} - \bar{J})}{2} \sum_{m \neq m',\sigma} \hat{n}_{m,\sigma} \hat{n}_{m',-\sigma} \tag{2-11}$$

where, summation is performed over projections of the orbital momentum ($m, m' = -3, -2 \ldots, 3$ in the case of *f*-electrons) and $\bar{U}$ and $\bar{J}$ are the spherically averaged matrix elements of the screened Coulomb electron-electron interaction [63,64]. The matrix for the effective LSDA+*U* potential can be achieved following the derivation in Dudarev et al. [64], and is shown below,

$$V_{jl}^{\sigma} \equiv \frac{\delta E_{\mathrm{LSDA}+U}}{\delta \rho_{lj}^{\sigma}} = \frac{\delta E_{\mathrm{LSDA}}}{\delta \rho_{lj}^{\sigma}} + (\bar{U} - \bar{J}) \left[\frac{1}{2} \delta_{jl} - \rho_{jl}^{\sigma} \right] \tag{2-12}$$

where, ρ_{lj}^{σ} is the density matrix of electrons occupying a partly filled electronic shell. And the total energy of the solid can be then be expressed in terms of Kohn-Sham eigenvalues $\{\epsilon_i\}$ as,

$$E_{\mathrm{LSDA}+U} = E_{\mathrm{LSDA}}[\{\epsilon_i\}] + \frac{(\bar{U} - \bar{J})}{2} \sum_{l,j,\sigma} \rho_{lj}^{\sigma} \rho_{jl}^{\sigma} \tag{2-13}$$

where, the last term is added to eliminate double counting of electrons. The Hubbard correction to the conventional LSDA potential in Eq. 2-12 affects the dispersion of electronic states and leads to the formation of a band gap in a metallic spectrum of excitations, depending on the value of $\bar{U}$. Moreover, the Hubbard correction term also changes the total energy of the solid, as per

Eq. 2-13, reforming the position of the minimum of the total energy functional and thus altering the predicted equilibrium structure of the solid.

One of the primary challenges of any application of LSDA+*U* approach is the determination of values of $\bar{U}$ and $\bar{J}$ entering the above three equations. The adjustable parameter of $\bar{U} - \bar{J}$ is generally fitted, to relevant experimental data, such as the band gap and lattice parameters.

2.1.5 Basis Sets: Plane-Waves and Gaussian Orbitals

The electronic structure of molecular and extended systems is described by the use of basis sets, which expand the molecular orbitals in wave function or Kohn-Sham density functional methods. Plane-wave basis functions are used for extended systems, as they are best suited for periodic boundary conditions. The use of plane-wave basis sets necessitates the use of pseudopotentials for representing the atomic core electrons. Slater- [65], or Gaussian-type [66] functions are used for the molecular systems, with Gaussian functions preferred over Slater functions for their better computational efficiency [67].

Projector-Augmented Wave (PAW) Method: The one-electron orbitals, Ψ_n, in the projector-augmented wave method [68] can be written as follows,

$$|\Psi_n\rangle = |\widetilde{\Psi}_n\rangle + \sum_i (|\varphi_i\rangle - |\widetilde{\varphi}_i\rangle) \langle \tilde{p}_i | \widetilde{\Psi}_n \rangle \tag{2-14}$$

where, the pseudo (PS) orbitals $\widetilde{\Psi}_n$, are the variational quantities of the PAW method, and are expanded in plane waves. φ_i and $\widetilde{\varphi}_i$ are the all-electron (AE) and pseudo partial waves, which are additional local basis functions that are nonzero only within the PAW spheres centered at the atomic sites. The true one-electron orbitals Ψ_n, are identical to the PS orbitals $\widetilde{\Psi}_n$ in the interstitial region between the PAW spheres. The PS orbitals are only a computational tool inside the PAW spheres and are bad approximations to the true wave functions. The AE partial waves

φ_i are regarded as the solutions of the spherical Schrödinger equation for a non-spin polarized atom at a specific energy ε_i in the valence regime [69]. Outside a core radius r_c, the PS partial waves $\widetilde{\varphi}_i$ are equivalent to their AE counterparts and match continuously onto φ_i inside the radius.

Orbital Basis Sets: The use of contracted Gaussian functions as basis, has proved to be a valuable technique in molecular orbital theory. An unknown one-electron function, such a molecular orbital Ψ_i, can be expanded using a set of known functions φ_μ, and be can be written as linear combination of atomic orbitals (LCAO) as follows,

$$\Psi_i = \sum_\mu c_{\mu i}\varphi_\mu \tag{2-15}$$

where, $c_{\mu i}$ are the variational coefficients. These coefficients are determined by minimizing the total energy, and lead to a matrix eigenvalue problem by traditional methods, which are solved iteratively to obtain a self-consistent field (SCF) solution. In the simplest calculation type, the minimal Gaussian-type orbitals φ are used, consisting of 1s for hydrogen, 1s, 2s, 2p for first row atoms and so forth. The matrix elements consist of multidimensional integrals over basis functions, of which those involving electron-electron interactions dominate the computational efforts.

2.1.6 Spin-Orbit Coupling (SOC)

Spin-orbit coupling (SOC) is an effective method to take the relativistic effects into account, in the first principles calculations. Inclusion of SOC causes the energy of a crystal to depend on the direction of magnetic moment, i.e., rotation of magnetic moments by the same angle results in different energies. SOC thus couples the spin to crystal structure.

Any (semi)-local operator O acting on the one-electron orbitals Ψ_i, can be written within the PAW method as a pseudo operator $\tilde{O}$ acting on the PS orbitals $\widetilde{\Psi}_n$, as follows,

$$\tilde{O} = O + \sum_{ij} |p_i\rangle(\langle\varphi_i|O|\varphi_j\rangle - \langle\tilde{\varphi}_i|O|\tilde{\varphi}_j\rangle)\langle p_j| \quad (2\text{-}16)$$

The spin-orbit coupling acts in the immediate vicinity of the nuclei and its effects are assumed to be negligible outside the PAW spheres. Using this assumption and provided the PS partial waves $\tilde{\varphi}_i$ form a complete basis set within the PAW spheres, the first and third terms of Eq. 2-16 exactly cancel out, and the contribution of the SOC to the PAW Hamiltonian reduces to the AE one-center contribution, as follows,

$$\widetilde{H}_{SO} = \sum_{ij} |p_i\rangle\langle\varphi_i|H_{SO}|\varphi_j\rangle\langle p_j| \quad (2\text{-}17)$$

In the zeroth-order-regular approximation [70], the Hamiltonian is given by $H_{SO}^{\alpha\beta} \propto \vec{\sigma}.\vec{L}$, where, $\vec{\sigma}$ is the Pauli-spin operator, and $\vec{L}$ is the angular momentum operator. The matrix elements of H_{SO} are calculated for the all-electron one-center contributions as,

$$E_{SO}^{ij} = \delta_{R_i}\delta_{R_j}\delta_{l_i l_j} \sum_{\alpha\beta} \left\langle \varphi_i \middle| H_{SO}^{\alpha\beta} \middle| \varphi_j \right\rangle \quad (2\text{-}18)$$

where, an atom is centered at a position R_i and α and β are the spin-up and spin-down components of the two-component spinor wave functions necessary to describe noncollinear magnetism [71].

2.2 Special Quasirandom Structures (SQS)

Accurate modeling of disordered (random) crystalline alloys is very significant to materials science, as many technologically important materials exhibiting tunable properties take the form of disordered alloys. The Special Quasirandom Structures (SQS) approach have proved to be an efficient technique to model such disordered alloys for electronic structure calculations [72,73]. A simple and transparent approach to model a disordered alloy would be merely taking a supercell of atoms and randomly occupying each lattice site. However, this method isn't the most accurate, as there is a large likelihood of deviating from "perfect" randomness in terms of local

correlations between chemical species occupation of nearby lattice sites. The SQS approach provides a significant improvement over this method, as a specified set of correlations between neighboring site occupations in the SQS match the corresponding correlation of the true and fully disordered state.

Selective occupation of N lattice sites by *A* and *B* atoms can generate a periodic SQS structure that mimics the correlation functions of an infinite substitutional random alloy far more closely than does the standard method of random occupation of lattice sites, for a finite N. The construction of SQS's is guided by the principle of close reproduction of the perfectly random network for the first few shells around a given site, thus deferring periodicity errors to more distant neighbors. This principle minimizes the spurious correlations (periodicity errors) beyond a certain distance in a periodic structure.

The algorithm of SQS generation seeks an SQS that perfectly match the maximum number of correlation functions between the candidate SQS and the perfectly disordered state. The algorithm as implemented in the Alloy Theoretic Automated Toolkit (ATAT) [73] is briefly described as follows. Let $\rho_\alpha(\sigma^{rnd})$ be the correlations of the fully disordered state at some composition, while $\rho_\alpha(\sigma)$ denote the correlations of a candidate SQS σ, and let $\Delta\rho_\alpha(\sigma) = \rho_\alpha(\sigma) - \rho_\alpha(\sigma^{rnd})$. The $\rho_\alpha(\sigma^{rnd})$ can be calculated as follows,

$$\rho_\alpha(\sigma^{rnd}) = \langle \prod_i \gamma_{\alpha_i'}, M_i(\sigma_i) \rangle_\alpha = \prod_i \langle \gamma_{\alpha_i'}, M_i(\sigma_i) \rangle_\alpha \tag{2-19}$$

where, α is a cluster of atoms, M_i are distinct chemical species occupying site i, and $\langle \gamma_{\alpha_i'}, M_i(\sigma_i) \rangle_\alpha$ is the cluster function which can directly be computed from the average composition of site i. The objective function to be minimized can be written as follows,

$$Q = -\omega L + \sum_{\alpha \in A} |\Delta \rho_\alpha(\sigma)| \tag{2-20}$$

where, L is the largest l such that $\rho_\alpha(\sigma) = 0$ for all clusters α with diam(α) $\leq l$ (with diam(α) being the length of the largest pair contained in cluster α, A is a user-defined set of clusters, and ω is a user-defined weight. The quality of an SQS is traditionally measured in terms of the number of correlations of the fully disordered it matches exactly, which is reflected by the $-\omega L$ term of the objective function. The second term in Eq. 2-20 adds the absolute difference of the error in the remaining correlations and guides the stochastic search in the correct direction to extend the range of perfect match. The SQS method is applied in Chapter 3 to model the solid-solution alloys of Cu-Au system.

CHAPTER 3
THERMODYNAMICS AND KINETICS OF ORDERED AND DISORDERED COPPER-GOLD ALLOYS[*]

3.1 Background

Formation of multi-metallic nanostructures is driven by interatomic mixing of the monometallic components. Cu-Au bimetallic nanoparticles may adopt either disordered alloy configurations or ordered intermetallic structure [34], thereby representing an interesting class of atomically intermixed bimetallic nanocrystals with tunable structures, compositions and properties. The synthetic routes to achieve Cu-Au bimetallic nanostructures include galvanic-replacement reaction (GRR) [74,75], co-reduction of Au and Cu in solution phase [76] and thermal reduction of Au@Cu_2O core-shell nanoparticles [77].

Although experimental observations have been made in the past confirming the transformation of Cu and Au monometallic nanocrystals into Cu-Au bimetallic nanoparticles and alloys, a fundamental understanding of the underlying thermodynamic, kinetic and mechanistic factors is lacking. Therefore, this chapter probes the thermodynamic and kinetic processes driving the evolution of Cu-Au alloys from their precursors. In particular, the objective is to better understand the structure-stability relationships of the Cu-Au system, especially in the Au-rich region where there are a large number of energetically similar structures. Based on recent work of Li et al. [78] and Koch et al. [77] where Cu-rich phases are etched away or destabilized when the underlying substrate is Au, epitaxial calculations are performed to investigate the effects of imposed lattice strain on the thermodynamic stability of Cu-Au ordered phases.

[*] The work described in this chapter has been published in S. Pandey, R. J. Koch, G. Li, S. T. Misture, H. Wang, S. R. Phillpot, Thermodynamics and kinetics of ordered and disordered Cu/Au alloys from first principles calculations, J. Alloys Comp. 809 (2019) 151615. doi:10.1016/j.jallcom.2019.07.327

The thermodynamic stability and post-synthesis structural remodeling behaviors of Cu-Au bimetallic nanocrystals are sensitively dependent upon the structural ordering and compositional stoichiometries of the nanoparticles. For example, the complex GRR-driven structural transformations of alloy and intermetallic nanoparticles are controlled by the interplay of three fundamental structure-transforming pathways: dealloying [79], Kirkendall diffusion [80], and Ostwald ripening [81]. Li et al. [78] have demonstrated that compositional stoichiometry and structural ordering are the two key factors that define the relative rates of the three-key structure-transforming processes in the colloidal Cu-Au system. In this chapter, diffusion pathways are modeled to explain the Kirkendall diffusion phenomenon driving the nanoscale structural evolution. Defect (vacancy) formation energies and diffusion barriers are calculated using first principles calculations in both intermetallics and disordered alloys.

3.2 Computational Methods

The density functional theory calculations (DFT) were performed using the Vienna *ab initio* simulation package (VASP) [82,83]. The projector-augmented wave (PAW) [68,84] method was used to simplify the treatment of core electrons. The generalized gradient approximation of Perdew, Burke, and Ernzerhof (GGA-PBE) [41] exchange correlation functionals were used for both Au and Cu. The $5d^{10}6s^{1}$ electrons were treated as valence for Au. Two different pseudopotentials were tested for Cu: Cu ($3d^{10}4s^{1}$) and Cu_pv ($3p^{6}3d^{10}4s^{1}$). The pseudopotential with 3s and 4d valence electrons only was found to be accurate enough to determine the formation enthalpies of ordered Cu-Au alloys, as benchmarked against literature [85,86]. The potential which also included the 3p valence electrons was used to model diffusion in the alloys, as this potential predicts the diffusion in Cu single crystal more accurately [87,88] . Unit cells ranging from 4 to 80 atoms were used for geometry optimization and formation

enthalpy calculations in the ordered alloys. Details of the simulation size, lattice constants, and formation enthalpies of the ordered alloys are documented in Table 3-1. A dense *k*-point mesh of 16×16×16 was first used to determine the plane wave cut-off energy of 500 eV, to get converged energies within 2 meV/atom, followed by *k*-point convergence using the same convergence criteria. An automatically generated Γ-centered 12×12×12 Monkhorst-Pack mesh [89] was used to sample the Brillouin zone of the smallest unit cells, while a 12×12×8 mesh was enough for bigger non-cubic supercells. The Methfessel-Paxton (1^{st} order) [90] smearing method was used to treat the partial orbital occupancies and for the integration of Brillouin zone, with a smearing width of 0.1 eV, which kept the electronic entropy term below 1 meV/atom. A conjugate gradient algorithm [91,92] was used for structural relaxations until the maximum force on each atom was <5 meV/Å, with an electronic convergence criterion of 10^{-6} eV. VASP (v5.4.4) was re-compiled with the force matrix in z-direction set to zero, to allow relaxations in the z-direction only and was used to carry out the substrate calculations.

The migration barriers were calculated using the climbing-image nudged elastic band (CI-NEB) method [93,94], with a force tolerance of 5 meV/Å. The Transition State Tools for VASP (VTST) package was used to interpolate the intermediate images and for post-processing purposes. Five intermediate images were used to find the transition states for all the cases. A supercell size of 2×2×2 was used to model the diffusion barriers in both ordered and random structures, with a coarser *k*-point mesh size of 5×5×5 in the Monkhorst-Pack scheme. The random structures were generated using the special quasi-random structure (SQS) method [72], generated using the Alloy Theoretic Automated Toolkit (ATAT) [73] software package.

3.3 Results and Discussions

The Cu-Au phase diagram has been extensively investigated, both experimentally [78,95] and computationally [85,86,96] with Au and Cu atoms being miscible over the entire stoichiometric range above 400° C, and forming intermetallic compounds below 400° C. However, different versions of the phase diagrams are reported, especially in the Au-rich region. For example, according to the phase diagram and the experimental studies in Li et al. [78] and Koch et al. [77] and the experimental formation enthalpies referenced in Zhang et al. [86], $CuAu_3$ (L_{12} type) is not a ground state of Cu-Au system, which is not consistent with a version of phase diagram by Okamoto et al. [95] where $CuAu_3$ is an observed phase.

Table 3-1. Composition, percentage of Au, structure type (L_{12} or L_{10}: most stable configuration), number of atoms in the unit cells (n), lattice constants, and formation enthalpies of fcc based Cu-Au ordered structures

Phase	% Au	Structure type	n	Lattice constants (Å)	Formation enthalpy (meV/atom)
Cu_5Au	16.7	L_{12}	12	a=3.75, b= 3.74, c=11.14	-28.0
Cu_3Au	25.0	L_{12}	4	a=b=c=3.78	-42.6
$Cu_{11}Au_5$	31.2	L_{12}	16	a=b=7.69, c=3.77	-45.3
Cu_2Au	33.3	L_{12}	12	a=3.87, b=3.73, c=11.68	-48.8
CuAu	50	L_{10}	4	a=b=4.03, c=3.68	-56.0
Cu_9Au_{10}	52.6	L_{10}	76	a=b=4.05, c=70.19	-54.5
Cu_8Au_9	52.9	L_{10}	68	a=b=4.04, c=63.13	-54.3
Cu_7Au_8	55.4	L_{10}	60	a=b=4.03, c=55.86	-54.0
Cu_5Au_6	55.5	L_{10}	44	a=b=4.06, c= 40.63	-53.3
Cu_4Au_5	55.7	L_{10}	36	a=b=4.04, c=33.72	-52.8
Cu_3Au_4	57.1	L_{10}	28	a=b=4.05, c=36.22	-52.0
Cu_2Au_3	60.0	L_{10}	20	a=b=4.06, c=18.84	-50.0
Cu_7Au_{11}	61.2	L_{10}	72	a=b=4.07, c=67.88	-46.6
Cu_5Au_8	61.5	L_{10}	52	a=b=4.06, c=49.36	-48.8
Cu_3Au_5	62.5	L_{10}	16	a=b=4.06, c=15.25	-48.1
Cu_4Au_7	64.6	L_{10}	44	a=b=4.04, c=42.70	-46.2
Cu_7Au_{13}	65.0	L_{10}	80	a=b=4.02, c=79.06	-43.8
$CuAu_2$	66.7	L_{10}	12	a=b=4.08, c=11.52	-45.0
Cu_2Au_5	71.4	L_{10}	28	a=b=4.11, c=26.85	-37.6
$CuAu_3$	75.0	L_{10}	8	a=b=4.10, c=7.82	-31.5
$CuAu_4$	80.0	L_{10}	20	a=b=4.13, c=19.65	-27.0
$CuAu_5$	84.3	L_{10}	12	a=b=4.13, c=11.91	-22.3
$CuAu_7$	87.5	L_{10}	16	a=b=4.14, c=16.01	-16.2

Similarly, the reported calculated convex hulls of Cu-Au show disagreements in the Au-rich region. PBE [85,86,96] and the meta-GGA type strongly constrained and appropriately normed semilocal density functional (SCAN) [96] in DFT predicts $CuAu_3$ to lie above the convex hull, whereas the hybrid functional developed by Heyd, Scuseria, and Ernzerhof (HSE) [86] predicts it to lie on the convex hull. The $CuAu_2$ phase is predicted to lie on the convex hull by PBE [86], while HSE [86] predicts it to lie above the hull.

Hence, a detailed study on the thermodynamics of Cu-Au ordered phases is carried out here, with particular emphasis on disentangling the Au rich region of this bimetallic system. PBE level theory is used for all the calculations, the reason for which will become clear in the later sections.

In addition, epitaxy of the Cu-Au ordered phases on the Au substrate is investigated in an attempt to explain the previous experimental studies [77], in which the diffraction measurements indicated that Au-rich bimetallic alloy nucleates simultaneously with the reduction of Cu_2O to metallic Cu, independent of Cu content of the system. Migration barriers for diffusion are also determined for both ordered and disordered phases to analyze the formation of these alloys from a kinetics point of view.

3.3.1 Ordered Structures of Cu-Au

The Cu-Au phase diagram shows two types of ordered structures. The fcc-based L_{10} structure (CuAu) consists of alternating (100) planes of Cu and Au, as shown in Fig. 3-1(a). Because the (010) and (001) planes contain equal numbers of Cu and Au atoms, L_{10} has tetragonal symmetry. The fcc-based L_{12} structure (Cu_3Au) consists of (100) planes of pure Cu, alternating with planes with equal numbers of Cu and Au atoms. This has a cubic symmetry. The PBE calculated lattice parameters are Cu (3.63 Å), Cu_3Au (3.78 Å), CuAu (a=b=4.03 Å, c= 3.68

Å; c/a ratio=0.915), and Au (4.16 Å). The reported crystal structures of $CuAu_2$ and $CuAu_3$ are β-2 tetragonal (L_{10} type) [85,86] and L_{12} [95] respectively.

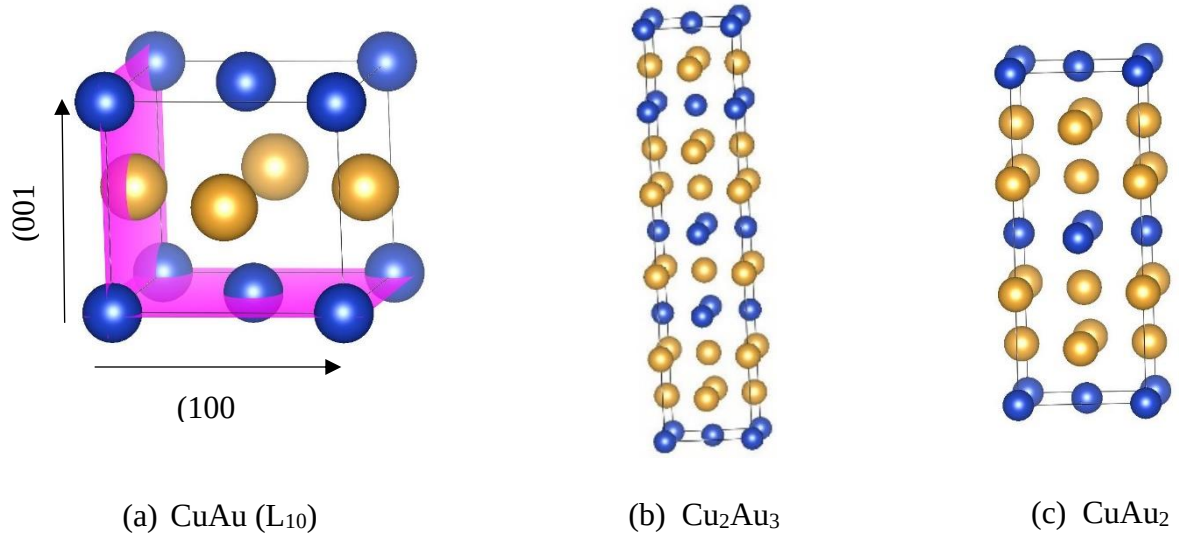

(a) CuAu (L_{10}) (b) Cu_2Au_3 (c) $CuAu_2$

Figure 3-1. Crystal structures of L_{10} and L_{10}-type ground states of Cu-Au. The gold colored atoms are Au and blue colored atoms are Cu. These structures are shown as rotated and tilted for clarity; however, all simulated structures are cubic or tetragonal.

We will examine superstructures of these basic structure types. The L_{10}-type superstructures that we examine (Fig. 3-1(b) and Fig. 3-1(c)) consist of m planes of pure Cu separated by n planes of pure Au in the [100] direction, with m=n=1 being the L_{10} structure itself. We further characterize these superstructures as building blocks of pure Au monolayers and ..$(CuAu)_x$ or L_{10} units as described further in section 3.3.5. The L_{12}-type superstructures in the Cu-rich region consist of L_{12} units separated by either mixed planes of Cu and Au (Fig. 3-2(b)) or pure Cu monolayers (Fig.3-2(c)). We also investigated these structures with pure Cu planes rather than mixed CuAu planes, which resulted to be higher in energies as discussed further in section 3.3.3.

Table 3-2 shows the first nearest neighbors of Cu and Au in L_{10} and L_{12} structures. The local environments of Cu and Au atoms determine the hopping sites for diffusion, as discussed later in section 3.3.6.

Table 3-2. First nearest neighbors of Cu and Au in the L_{10} and L_{12} structures

Species	First nearest neighbors (NN) shell	
	L_{10} (CuAu)	L_{12} (Cu_3Au)
Cu	(4Cu, 8Au)	(8Cu, 4Au)
Au	(8Cu, 4Au)	(12Cu, 0Au)

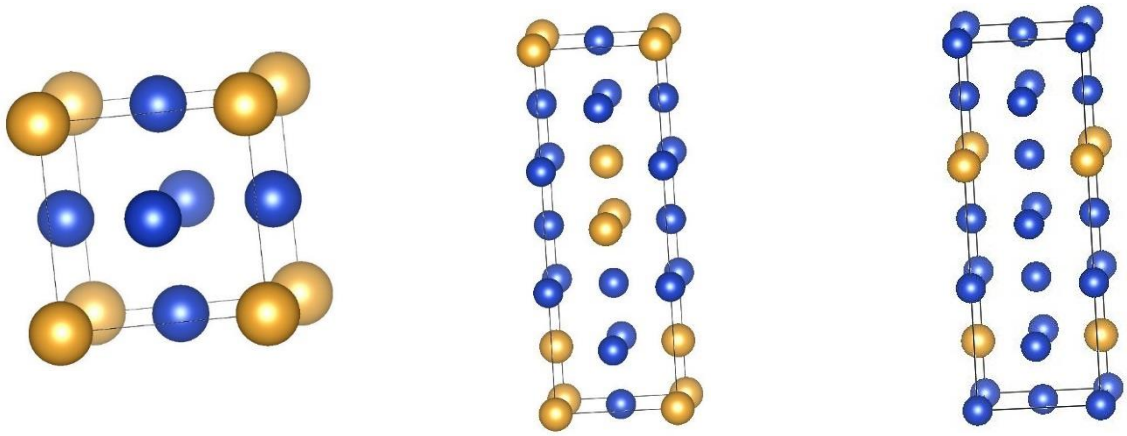

(a) Cu_3Au (L_{12}) (b) Cu_2Au (c) Cu_5Au

Figure 3-2. Crystal structures of L_{12} and L_{12}-type structures of Cu-Au. The gold colored atoms are Au and blue colored atoms are Cu. L_{12} and Cu_2Au are the ground states.

3.3.2 Random (disordered) Structures of Cu-Au

The widely used special-quasi random structure (SQS) approach [72] is used to model the Cu-Au solid solution alloys. SQS structures reproduce the radial distribution functions of a very large random structure of the same composition as accurately as possible for a smaller system size of N atoms; N can be quite small, with typical values ranging from N=8 to N=108. The SQS method calculates the radial distribution functions of the finite cell and comparing it to that of an (essentially) infinite random system. The differences in the correlation functions are then

minimized to give the best possible representation of the random structure. We use the popular ATAT code [73] to build the SQS structures.

In this work, a 32-atom SQS structure has been used to model the Cu-Au random alloys, to be consistent with the size of ordered alloys. The comparison of formation energies of different supercell sizes of Cu_3Au SQS is shown in Table 3-3 to establish thermodynamic robustness of different sizes of SQS structures: this formation energy varies by less than 10% with system size; thus, the 32 atom is used to model Cu-Au SQS structures.

Table 3-3. Free energy of formation (ΔG_f) of Cu_3Au SQS structures for different supercell sizes, showing its relative independence of system size.

Supercell size	No. of atoms	ΔG_f (meV/atom)
2×2×2	32	+8.34
3×3×3	108	+7.68
4×4×4	256	+7.95

3.3.3 Thermodynamics of Cu-Au

The free energy of formation per atom of any phase Cu_xAu_{1-x}, $\Delta G_{f,Cu_{1-x}Au_x}$, is given by

$$\Delta G_{f,Cu_xAu_{1-x}} = G_{Cu_{1-x}Au_x} - \{x(G_{Au}) + (1-x)(G_{Cu})\} \quad (3\text{-}1)$$

where, $G_{Cu_{1-x}Au_x}$ is the free energy (per atom) of Cu_xAu_{1-x} and G_{Cu} and G_{Au} are the free energies per atom of pure Cu and Au.

We have determined the formation energies of various ordered Cu-Au structures at the PBE and SCAN level of theory and compared them to the literature (Fig. 3-3 and Table 3-4). Although the SCAN and HSE formation enthalpies are larger than the PBE enthalpies, and are also closer to experimental values reported in Ref. [86], the relative stability of the phases remains generally the same; however, HSE predicts $CuAu_2$ to be unstable and $CuAu_3$ to be stable which is inconsistent with experiments. The experimentally observed phases of Cu-Au are Cu_3Au and CuAu [77,78] which are also the two of the ground states predicted by PBE and SCAN levels of theory. Although PBE and SCAN incorrectly predicts Cu_2Au, Cu_2Au_3 and

$CuAu_2$ as ground states, all these phases are only marginally stable with respect to the experimental Cu_3Au and CuAu ground states. Cu_2Au lies below the tie-line formed by Cu_3Au and CuAu by less than 1 meV, while Cu_2Au_3 and $CuAu_2$ lies below the tie-line formed by CuAu and pure Au by less than 5 meV. $CuAu_3$ lies above the convex hull in both PBE and SCAN levels of theories, by less than 2 meV. We also calculated a couple of near-hull phases in the Au rich region described in section 3.3.5, using SCAN level of theory to establish qualitative consistency with PBE results. These phases lie above the hull by the same amount in both PBE and SCAN level of theories, as discussed later in section 3.3.5. Thus, we use the PBE level of theory, which is also the least computationally expensive functional and being consistent with experiment, as shown in Fig. 3-3.

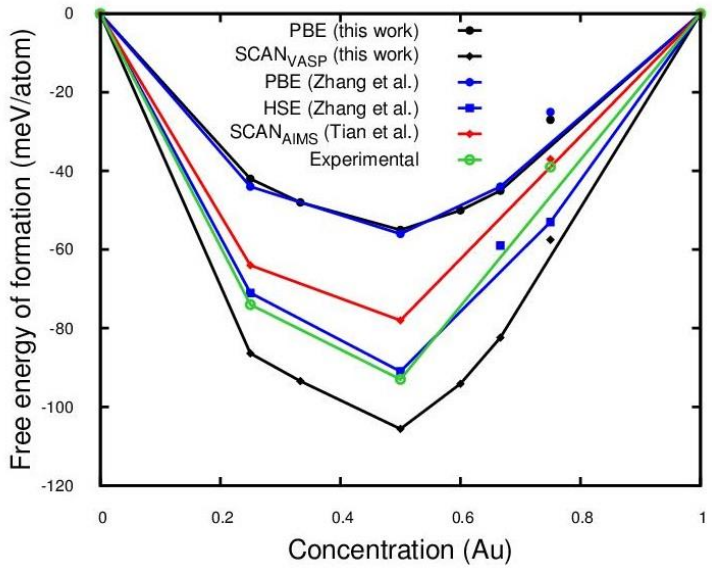

Figure 3-3. Cu-Au convex hulls calculated in this work (PBE and SCAN) and compared to DFT and experimental literature: Zhang et al. [86], Tian et al. [96], and the experimental values are taken as reported in Ref. [86].

There are five ground states on the calculated PBE convex hull, as shown in Fig. 3-4: Cu_3Au (L_{12}), Cu_2Au, CuAu (L_{10}), Cu_2Au_3 and $CuAu_2$. As described in section 3.3.1, the crystal structure of these phases can be either L_{10}-type or L_{12}-type. The Cu-rich L_{12}-type Cu_2Au

structure is orthorhombic with lattice constants *a*=3.87 Å, *b*=3.73 Å and *c*=11.68 Å, while Au-rich $L1_0$-type Cu_2Au_3 and $CuAu_2$ have tetragonal structures with lattice constants [*a*(Å), *c*(Å)= (4.06,18.84) and (4.08,11.52)] respectively.

Table 3-4. Gibbs free energy of formation (ΔG_f) at 0K of various phases of Cu-Au calculated in this work and compared to other DFT and experimental literature.

Phase	ΔG_f (meV/atom)				
	This work (PBE)	PBE (literature)	SCAN (literature)	HSE (literature)	Experiment (literature)
Cu_3Au ($L1_2$)	-42	-43.3 [85], -44 [86], -45 [96]	-64 [96]	-71 [86]	-74 [96]
Cu_2Au ($L1_2$ type)	-48	-50.6 [85]	…	…	…
CuAu ($L1_0$)	-56	-55.1 [85], -56 [86], -57 [96]	-78 [96]	-91 [86]	-93 [96]
Cu_2Au_3 ($L1_0$ type)	-50	-51.5 [85]	…	…	…
$CuAu_2$ ($L1_0$ type)	-45	-46.3 [85], -44 [86]	…	-59 [86]	…
$CuAu_3$ ($L1_2$)	-27	-25 [86], -24 [96]	-37 [96]	-53 [86]	-39 [96]

Table 3-5. Comparison of lattice constants (in Å) of Cu, Cu_3Au, CuAu and Au phases, for GGA-PBE, SCAN, HSE functionals and experimental values.

Phase	PBE (this work)	PBE[96]	SCAN (this work)	SCAN[96]	HSE[86]	Experiment (as reported in ref. [86])
Cu	3.63	3.63	3.55	3.55	3.61	3.61
Cu_3Au	3.78	3.78	3.70	3.69	3.72	3.72
CuAu	4.03	4.03	3.96	3.95	4.00	3.96
Au	4.16	4.16	4.08	4.07	4.08	4.05

The Cu-rich phases were always found to be more stable in $L1_2$-type structures, while Au-rich phases were found to be more stable in $L1_0$-type structures. For example, $L1_2$ Cu_3Au is more stable than as its layered Cu_6Au_2 counterpart, as shown in Fig. 3-4. Similarly, the Au-rich $CuAu_3$ phase is more stable as layered Cu_2Au_6 than as its $L1_2$ $CuAu_3$ counterpart. The crystal structures of $L1_0$ type Cu_3Au and $CuAu_3$ phases are depicted in Fig. 3-5 and can be viewed as a $L1_0$ unit sandwiched between monolayers of either Cu or Au, such as Cu + $L1_0$ + Cu. Thus, there is a high strain energy associated with the $L1_0$ type Cu-rich phases, as bigger Au atoms (atomic radius: 0.144 nm) are inserted between monolayers of smaller Cu atoms (0.128 nm). By contrast, the smaller Cu atoms can easily sit in the same plane as Au atoms which leads to the $L1_2$ type

configuration, and hence a lowering of the strain energy. In the Au-rich region, strain energy is lower for the L_{10} type configuration, as low concentrations of smaller Cu atoms can be easily inserted between high concentration big Au monolayers.

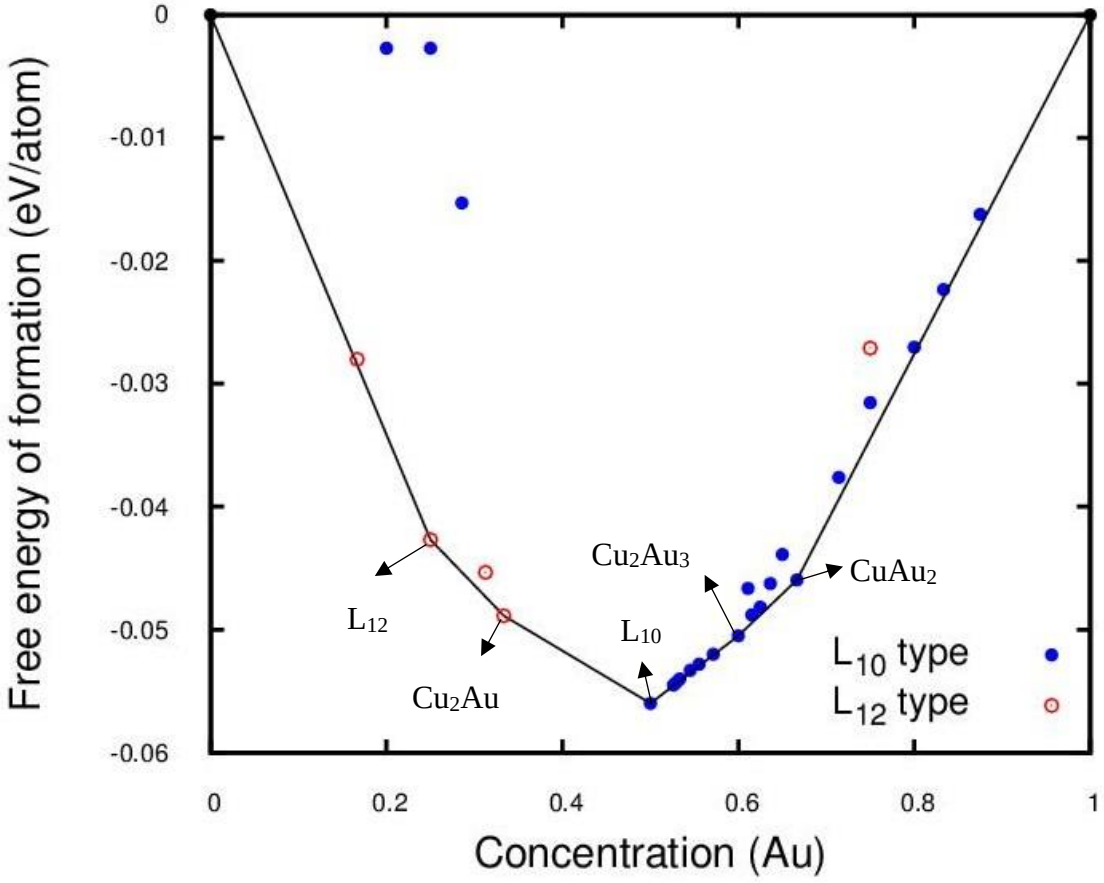

Figure 3-4. Convex-hull of the Cu-Au system, showing Gibb's free energy of formation at 0K of various phases as a function of fractional Au concentration. The solid blue circles correspond to L_{10}-type structures and the open red circles denotes L_{12}-type structures.

Zhang et al. [86], investigated three of the five predicted ground states in the previous studies of Sanati et al. [85], the two additional ground states being Cu_2Au and Cu_2Au_3 identified in this work. As shown in Table 3-4, this work confirms the stability of all five structures and further characterizes all the five ground states reported by Sanati et al.

In addition to the ground states, we find that in the Au-rich region there are numerous structures that, while not lying on the convex hull, lie extremely close to it, as shown in Fig. 3-4. Recalling that room temperature corresponds to 25 meV, these near-hull phases are likely metastable as their formation energies are less than 3 meV/atom greater than the true ground states. These structures are analyzed as superstructures of the neighboring ground states in section 3.3.5.

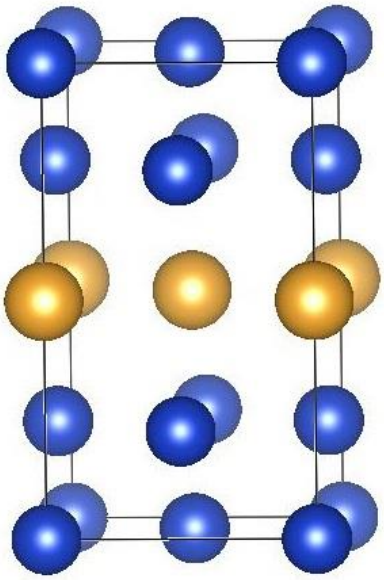

(a) Cu_6Au_2 (Cu + L_{10} + Cu)

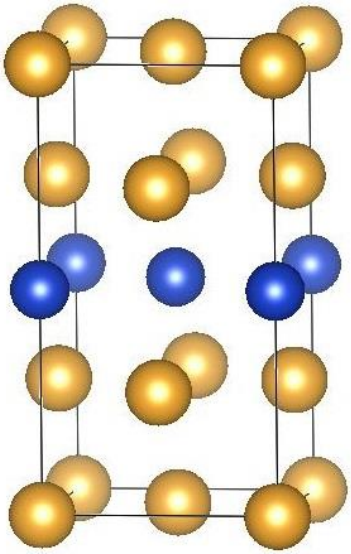

(b) Cu_2Au_6 (Au + L_{10} + Au)

Figure 3-5. L_{10} derived structures of (a) Cu_3Au (b) $CuAu_3$. These structures are compared to their L_{12} derived counterparts (L_{12} type) Cu_3Au and $CuAu_3$, for their energetics.

3.3.4 Epitaxy on Au Substrate

We also analyze the case in which Cu-Au systems are grown on a Au substrate as this corresponds closely to the experimental situation in nanoparticles discussed in the introduction. We anticipate an increase in the energies of structures, with the magnitude depending on their stoichiometries (either Cu-rich or Au-rich) and on the growth planes. The epitaxially strained bulk alloys are modeled here rather than the full Cu/Au interface, as there is no mixing at the

interfaces of these core-shell structures. Such DFT calculations are accomplished by fixing the in-plane lattice parameters of the structures to that of Au (=4.16 Å) and only allowing the z-direction lattice parameter to relax; however, atom positions are allowed to optimize to zero force in all three directions. All three {100} planes are identical for the cubic $L1_2$ Cu_3Au structure but not for other structures, as is evident from Fig. 3-1 and Fig. 3-2. The (001), (100) and (010) planes are distinct from each other for the orthorhombic $L1_2$-type Cu_2Au structure, and hence there are three different growth planes. The tetragonal $L1_0$-type structures ($L1_0$, Cu_2Au_3 and $CuAu_2$) can be grown with either of the structurally distinct (100) or (001) planes as the growth plane. For CuAu, the (001) and (010) planes are identical, whereas for Cu_2Au_3 and $CuAu_2$, the (100) and (010) planes are identical. Thus, three different convex hulls are obtained by doing substrate calculations in this manner: (1) tie-lines joining phases grown along (100) direction (2) tie-lines joining phases along (001) direction and (3) tie lines joining (010) phases grown along (010) direction. These epitaxial convex hulls are compared with the unstrained (free bulk) convex-hull in Fig. 3-6. Bulk pure Cu and pure Au under no stress constraints were used as reference states to calculate the Gibb's free energy of formation by Eq. 3-1.

It can be clearly seen in Fig. 3-6 that the Cu rich phases ($L1_2$ and Cu_2Au) are destabilized when grown on Au substrate. This can be explained by the strain imposed on the small Cu atoms when strained to the lattice parameter of Au. The {100} family of planes of the cubic $L1_2$ Cu_3Au phase are strained by a linear strain of 10.05%, relative to the unstrained structure. This high linear strain leads to a high strain energy of 49.9 meV/atom, and thus the formation energy increasing by >100% relative to the unstrained structure. Similarly, all the three distinct planes of the orthorhombic Cu_2Au phase are under high linear strains of [(100) =9.16%, (010) =10.05% and (001) =10.78%]. This leads to a high strain energy (meV/atom) of =38.6 meV/atom for

(100), 25.0 meV/atom for (010), and 45.1 meV/atom for (001); that is, the formation energies are increased by 79% for the (100) plane, 51% for (010), and 92% for (001).

The tetragonal L_{10} phase and Au-rich phases experience much lower strains and are not destabilized. The (100) plane of L_{10} CuAu phase is under a linear strain of 3.22%, however the lattice parameter perpendicular to this plane relaxes to a value which almost completely compensates for the in-plane strain and leads to almost zero strain energy. Thus, the strained (100) formation energy and unstrained formation energy points essentially lie on top of each other for the L_{10} phase. The (001) and (010) planes are identical for the L_{10} phase, and experience a linear strain of 8.02%, which in turn leads to a strain energy of 47.1 meV/atom. The formation energy thus increases by 90% if the L_{10} phase is grown along (001) or (010) planes. The (001) planes of Cu_2Au_3 and $CuAu_2$ phases are under small linear strains of 2.46% and 1.96% respectively. For both cases, the relaxed z-direction lattice parameters again compensate for the linear strains, leading to small strain energies of Cu_2Au_3 = 2.3 meV/atom and $CuAu_2$ = 1.1 meV/atom. Thus, the formation energies for these two planes are essentially the same as for the unstrained system. The (100) and (010) planes are identical for these two phases and are under linear strains of Cu_2Au_3 = 6.35% and $CuAu_2$ = 5.09%, leading to strain energies of Cu_2Au_3 = 28.6 meV/atom and $CuAu_2$ = 16.3 meV/atom. The formation energies of Cu_2Au_3 and $CuAu_2$ phases thus increase by 59.0% and 36.6% when grown along (100) or (010) planes.

In summary, the L_{10} phase and Au rich phases (Cu_2Au_3 and $CuAu_2$) remain stable, with (100) being the stable orientation for L_{10} and (001) for Cu_2Au_3 and $CuAu_2$. The lattice mismatch continues to decrease as the Au concentration in the phases increases. Thus, the Gibb's free energy of the phases experience less change relative to their unstrained counterparts as we move towards the Au rich phases.

The overall convex hull for the Au substrate, i.e., the lowest of (001), (010) and (100), is shown by dashed lines in Fig. 3-6. No Cu-rich phase lies on the hull, while the L_{10} and Au rich phases lie on the hull when grown along (100) and (001) planes respectively. These results are consistent with the experimental observations of [77] where nucleation of Au rich bimetallic alloy is indicated by the diffraction measurements, with the onset of reduction of cuprite shell to metallic Cu. The Cu-rich phases phase separate to Cu and CuAu as can be seen in Fig. 3-6, and thus are destabilized, which also explains the dealloying phenomenon of selective etching of Cu from Cu-Au alloy as observed in [78].

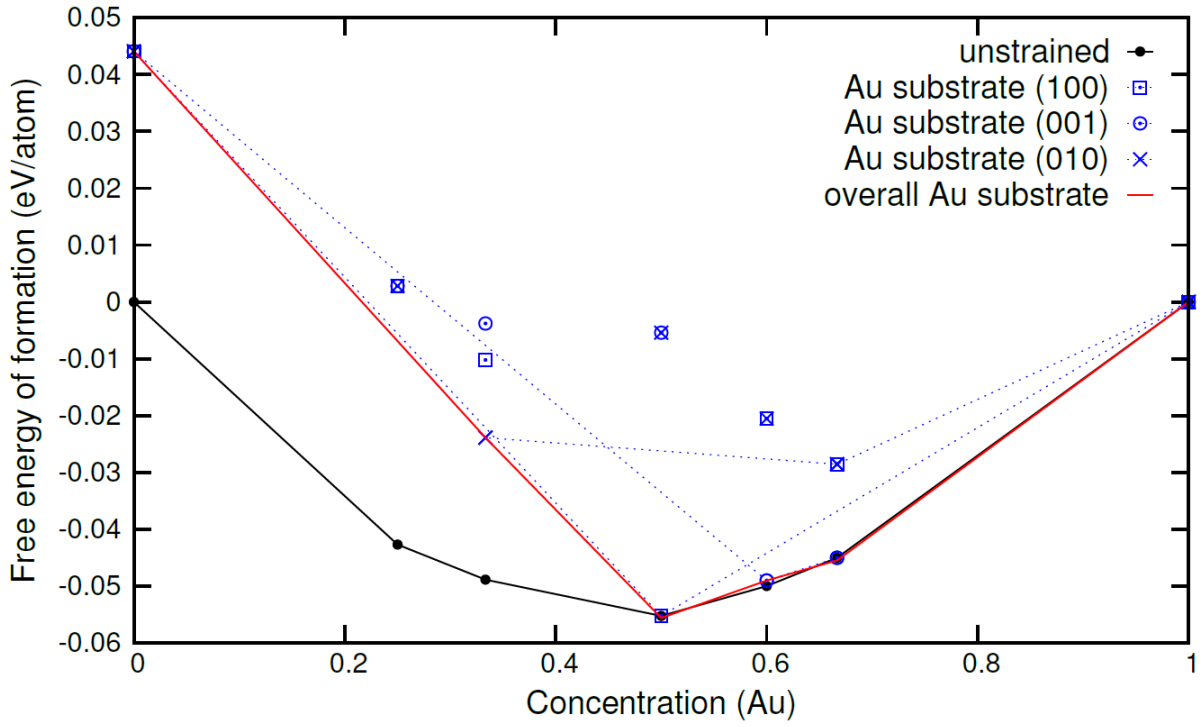

Figure 3-6. Convex-hulls of Cu-Au ground states in unstrained state (black circles), and when grown on Au substrates along (001) planes (blue open circles), (100) planes (blue squares) and (010) planes (blue cross), and overall convex hull on Au substrate (solid red line).

3.3.5 Metastable Cu-Au Phases

The unstrained convex-hull in Fig. 3-4, shows several structures on the Au-rich side of the phase diagram that lie extremely close to the tie-line. This region near the convex hull between two distinct ground states shows some interesting trends. For example, Fig. 3-7(a) shows some of the Au rich phases between the CuAu L_{10} and Cu_2Au_3 ground states, lying above the hull by just ~0.1-0.25 meV/atom. Similarly, Fig. 3-7(b) shows phases between Cu_2Au_3 and $CuAu_2$ ground states. In unstrained conditions, there are multiple states lying above the hull by ~1-3 meV/atom; given that room temperature corresponds to 25 meV and the inherent limits on the accuracy of DFT, these structures are quite likely to be manifested experimentally.

The phases between L_{10} and Cu_2Au_3 phase have a stoichiometry Cu_xAu_{x+1}, such as Cu_9Au_{10}, Cu_8Au_9. Their structures are of the form ….$(CuAu)_x$/Au/$(CuAu)_x$/Au…. or ….$(L_{10})_x$/Au/$(L_{10})_x$/Au…. and are similar to their end ground states in layering sequence. A representative structure of this kind (Cu_3Au_4) is shown in Fig. 3-8(a). It has six L_{10} units separated by monolayers of Au. We have also examined structures of the form …$(L_{10})_{x-1}$/Au(CuCu)Au/$(L_{10})_{x-1}$… .These structures, although having the same overall stoichiometry as the L_{10}-type phases have considerably high energies. For example, the Au/$(L_{10})_2$/Au(CuCu)Au/$(L_{10})_2$/Au sequence of Cu_3Au_4 lies 12 meV/atom above its ground state sequence of Fig. 3-8(a). The smaller size of copper atoms causes them to be highly strained if placed next to each other.

The phases between Cu_2Au_3 and $CuAu_2$ ground states have diverse stoichiometries of Cu_xAu_{x+2}, Cu_xAu_{x+3}, Cu_xAu_{x+4} and Cu_xAu_{x+6} where $3 \leq x \leq 7$. While there is no uniform sequencing of layers, unlike Cu_xAu_{x+1} type structures, all their structures do have several repetitions of two Au monolayers next to each other separating the Cu layers, or repetitions of

Au monolayers separating the two ..(CuAu).. or L_{10} units. Another way of characterizing these structures is to view them as L_{10} units separated by multiple blocks of ..(Au+L_{10}).. in their unit cells, unlike the Cu_xAu_{x+1} structures which have just one such block in their unit cells. A representative structure of this kind (Cu_5Au_8) is shown in Fig. 3-8(b), which can be characterized as $(L_{10})_3/(Au+L_{10})_6/(L_{10})_1$.

After a structure-energy analysis, it is observed that the higher the number of pairs of Au monolayers in a structure, the higher its energy lies above the hull. The Cu_7Au_{13} has the most such pairs (=12) of Au monolayers and its energy lies highest above the hull (3meV/atom), which is also a peak as seen in Fig. 3-7(b). The Cu_7Au_{11} structure has 8 such pairs and its energy lies ~2.8meV/atom above the hull, which is the second peak of Fig. 3-7(b). Similarly, Cu_5Au_8, Cu_3Au_5, and Cu_4Au_7 have 6, 2 and 6 such pairs and their energies lie above the hull by 0.5, 0.5 and 2 meV/atom respectively.

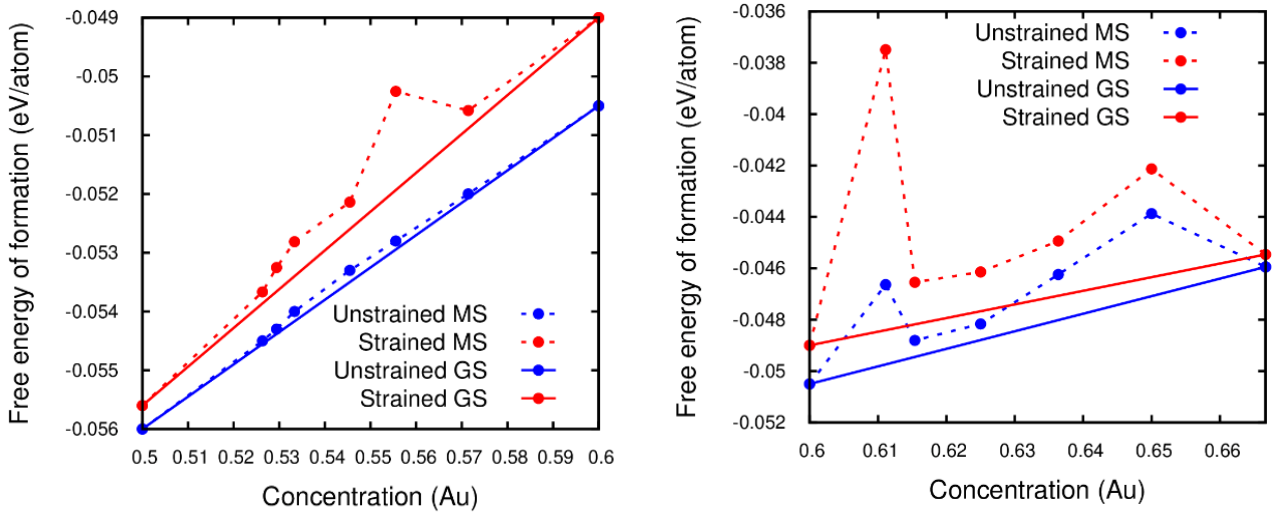

(a) phases between L_{10} and Cu_2Au_3

(b) phases between Cu_2Au_3 and $CuAu_2$

Figure 3-7. Metastable (MS) ordered Cu-Au phases lying close to the hull (a) between L_{10} and Cu_2Au_3 ground states (GS) and (b) between Cu_2Au_3 and CuAu ground states (GS). Blue dots correspond to the unstrained state and red dots denotes strained states on Au substrate

Fig. 3-7(a) and 3-7(b) also show the effect of epitaxy on a Au substrate on the stability of $_2$these phases. They show similar trends to the unstrained phases. The hull formed by the phases grown on Au substrate lie above the unstrained hull by ~1-2.5 meV/atom, between the ground states $L1_0$ and Cu_2Au_3 and by 1-10 meV/atom between the ground states Cu_2Au_3 and $CuAu_2$.

As mentioned above in section 3.3.3, a comparison of formation energies of two near-hull phases (Cu_5Au_6 and Cu_3Au_5) is made using SCAN and PBE functionals. Both these phases are predicted to be metastable by SCAN and PBE level of theories, with their energies lying above the hull by the same amount (<1 meV/atom). Thus, the predictions made by PBE level of theory for the near-hull phases in the Au rich region are robust.

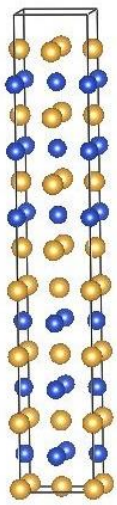

(a) Cu_3Au_4

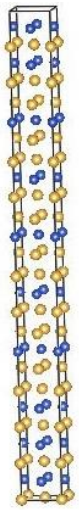

(b) Cu_5Au_8

Figure 3-8. Near-hull (metastable) phases on the Au-rich region between two ground states (a) Cu_xAu_{x+1} type Cu_3Au_4 (b) Cu_xAu_{x+3} type Cu_5Au_8.

In conclusion, epitaxial growth on the Au substrate favors the stability of Au rich phases while destabilizing the Cu rich phases, consistent with the experimental observations of dealloying, and nucleation of Au rich bimetallic alloys during reduction of $Au@Cu_2O$ core-shell nanoparticles [77]. A number of phases lie close to the convex hull on the Au rich region

showing complex energetic trends between each pair of true ground states. The Au rich phases stabilize in the L_{10} type configuration while the Cu rich phases are more stable as L_{12} type structures.

In addition to the thermodynamic stability, diffusion plays a key role in the evolution of alloys. The following sections describes the kinetics of Cu-Au ordered and random alloys. Migration barriers and activation energies are computed to determine the dominant diffusion mechanisms.

3.3.6 Diffusion in Ordered Phases

Vacancy assisted diffusion paths are modeled for Cu-Au alloys as the dominant mechanism of diffusion in fcc structures. L_{12} and L_{10} ground states are chosen to determine the minimum energy paths (MEPs), for these two being the experimentally observed ordered phases. Diffusion of a species depends on its local environment; the first neighbor nearest shells of both Cu and Au in L_{12} and L_{10} are given in Table 3-2. A Cu atom can move to either a Cu or Au vacant site in both L_{12} and L_{10} ordered structures, while a Au atom can move to either a Au or Cu vacant site in L_{10} and can move to only a Cu vacant site in L_{12}. Atomic representations of these jumps are captured in Fig. 3-9.

Figures 3-10(a) and 3-10(b) show vacancy mediated MEPs of Cu and Au in the single crystals, L_{12}, and L_{10} structures respectively. The Cu$\rightarrow v_{Au}$ jump has a lower migration barrier than the Cu$\rightarrow v_{Cu}$ jump in both L_{10} and L_{12} phases and Cu$\rightarrow v_{Cu}$ jump in the pure metal (Fig. 3-10(a)). The lower migration barrier of Cu$\rightarrow v_{Au}$ than Cu$\rightarrow v_{Cu}$ in the L_{10} phase can be attributed to its tetragonality. The Cu atom has to jump along the [001] direction to migrate to a Au vacancy in its 1st NN; these planes are separated by 1.85 Å. By contrast, within the (001) or (010) plane, the interplanar spacing is 2.00 Å. The lower spacing between (100) planes in turn

leads to a lower total migration distance for Cu→v_{Au} (3.02 Å) than for Cu→v_{Cu} (3.45 Å). By contrast, L_{12} is cubic and thus the interplanar spacing among {100} family of planes is same. In this case, the lower migration barrier for Cu→v_{Au} than Cu→v_{Cu} can be attributed to the smaller size of Cu than Au, which makes it easier for the Cu atom to jump into a vacant Au site, than into a vacant Cu site.

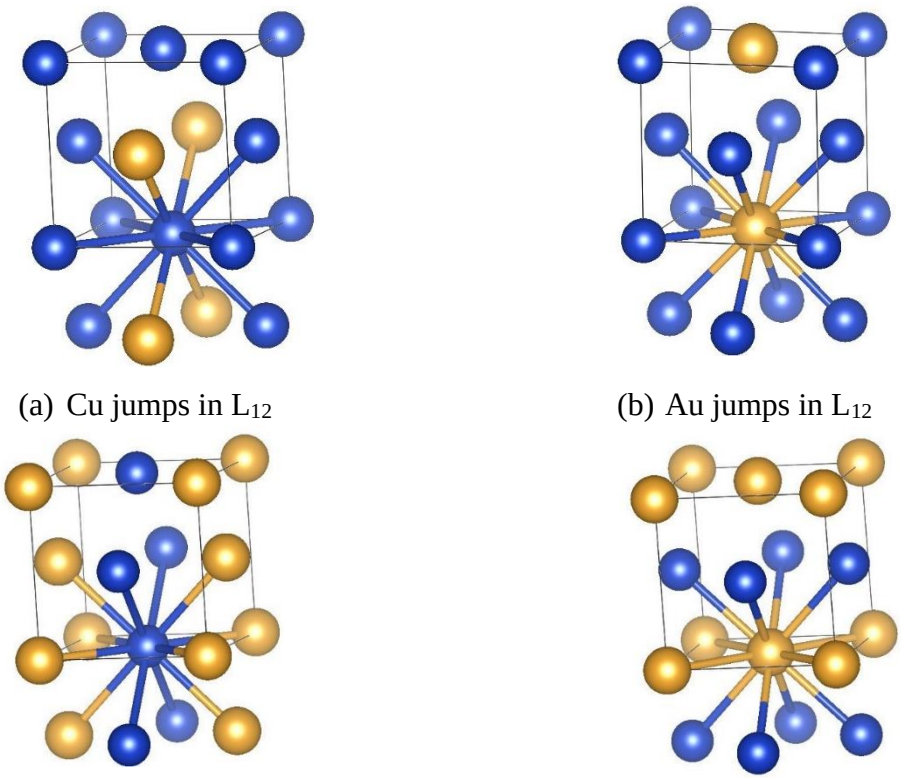

(a) Cu jumps in L_{12} (b) Au jumps in L_{12}

(c) Cu jumps in L_{10} (d) Au jumps in L_{10}

Figure 3-9. Atomic jumps of (a) Cu in L_{12} (b) Au in L_{12} (c) Cu in L_{10} (d) Au in L_{10}. Blue colored atoms are Cu and gold colored atoms are Au.

The lower migration barrier for Cu diffusion in L_{12} and L_{10} phases than in pure Cu could be because of the tensile stress on the Cu atoms in these structures. To isolate these effects of strain from those of the local environment, we determined the migration barriers for Cu→v_{Cu} in pure Cu strained to lattice parameters of L_{12} and L_{10} structures. The self-diffusion migration

barrier of Cu in pure Cu when strained to L_{12} lattice parameters was found to be 0.62 eV which is very similar to the 0.63 eV barrier for Cu→v_{Cu} barrier in L_{12}. The migration barrier of Cu in pure Cu when strained to L_{10} lattice parameters was found to be 0.38 eV which is similar to the 0.34 eV barrier for with Cu→v_{Au} in L_{10}.

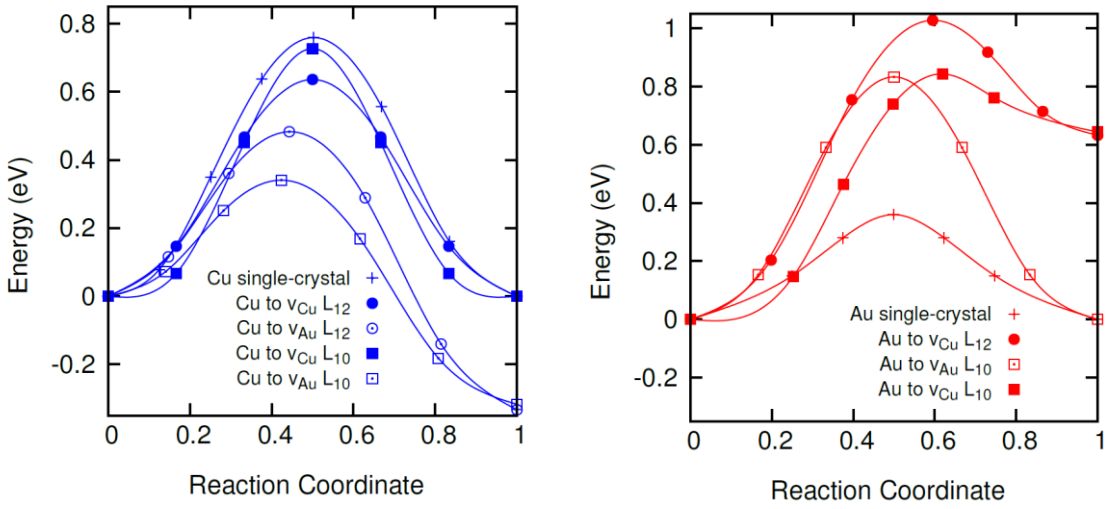

(a) Cu MEPs (b) Au MEPs

Figure 3-10. Minimum energy paths (MEPs) of (a) Cu (b) Au; in their single crystals, L_{12} and L_{10} structures.

The jump of Au to a vacant Au site has a lower migration barrier than for jump to a vacant Cu site in the L_{10} phase (Fig. 3-10(b)); however, the difference is small, 0.01 eV. The higher migration barrier for Au diffusion in L_{12} and L_{10} phases than in pure Au can be attributed to the compressive stress on Au atoms in these phases. In analogy with Cu, we determined the migration barriers of Au self-diffusion in pure Au strained to L_{12} and L_{10} lattice parameters, The migration barrier for Au diffusion in pure Au when strained to L_{12} lattice parameters was found to be 1.50 eV, in comparison to the 1.02 eV barrier for Au→v_{Cu} in L_{12}. The Au→v_{Au} transition is not possible in L_{12} as there is no Au in the 1st NN shell of Au in L_{12}. The migration barrier for Au diffusion in pure Au when strained to L_{10} lattice parameters was found to be 0.82 eV which is

consistent with 0.83 eV for Au→v_{Au} and 0.84 eV for Au→v_{Cu} barriers in L_{10}. This analysis show that the migration barriers in the alloys are predominantly determined by the strain, with the local atomic environment only having a small effect.

The total activation energy for a diffusion process is considered to be the sum of vacancy formation energy (if the vacancy is the dominant mode of diffusion) and the migration barrier. The vacancy formation energies are thus also calculated in the single crystals, L_{12} and L_{10} phases, as,

$$E_{v,i} = E(N-1) - E(N) + \mu_i \quad (3\text{-}2)$$

where, $E_{v,i}$ is the vacancy formation energy of a specie i, $E(N-1)$ is the energy of system with a monovacancy, $E(N)$ is the energy of perfect system, μ_i is the chemical potential of specie i, and N is the total number of atoms in the perfect system. The chemical potential μ_i (for ordered phases and single crystals) in this work, is just taken to be the cohesive energy per atom of fcc Au or fcc Cu. The vacancy formation energies (E_v) and migration barriers (E_m) of Au and Cu in their single crystals, and L_{12} and L_{10} phases are given in Table 3-6.

Table 3-6. Vacancy formation energies (E_v) and Migration barriers (E_m) of Cu and Au in different phases.

Phase	E_v (eV)	E_m (eV)
Cu (this work)	1.08	0.75
Literature (DFT)	1.13 [97] , 1.07 [87]	0.72 [87],
Literature (Experiment)	1.19 [98], 1.27 [99]	0.71 [88], 1.02 [100]
Au (this work)	0.45	0.30
Literature (DFT)	0.42 [101]	0.28 [101]
Literature (Experiment)	0.94 [102]	0.84 [102]
	v_{Cu} = 1.84	Cu_{Cu} → v_{Cu} = 0.63
L_{12} (this work)	v_{Au} = 2.59	Cu_{Cu} → v_{Au} = 0.48
		Au_{Au} → v_{Cu} = 1.02
		Cu_{Cu} → v_{Cu} = 0.72
L_{10} (this work)	v_{Cu} = 0.94	Cu_{Cu} → v_{Au} = 0.34
	v_{Au} = 1.52	Au_{Au} → v_{Cu} = 0.84
		Au_{Au} → v_{Au} = 0.83

Note: v_{Cu} = vacancy at a copper site, v_{Au} = vacancy at a gold site, Cu_{Cu} → v_{Cu}: copper atom migrating to a vacant Cu site and so on

The activation energies for migration (E_a) are then calculated as the sum of vacancy formation energies and migration barriers ($E_a = E_v + E_m$), and are represented by Fig. 3-11(a) and Fig. 3-11(b), for Cu and Au respectively. Cu vacancy mediated diffusion paths of both Cu and Au have lower activation energies than their Au vacancy mediated diffusion paths, in both L_{12} and L_{10} phases (blue bars in Fig. 3-11(a) and 3-11(b) are shorter than red bars in L_{12} and L_{10} phases) and hence, both Cu and Au diffuse via a Cu vacancy rather than by a Au vacancy. The activation energy for Cu vacancy mediated diffusion of Cu in the L_{10} phase is lower than its activation energy for self-diffusion in the single crystal by 0.16 eV; and higher in the L_{12} phase by 0.65 eV than the Cu single crystal. The activation energy for Cu diffusion mediated by a Au in the L_{10} phase is almost the same as its self-diffusion in the Cu single crystal and higher in the L_{12} phase by 1.24 eV than the Cu single crystal.

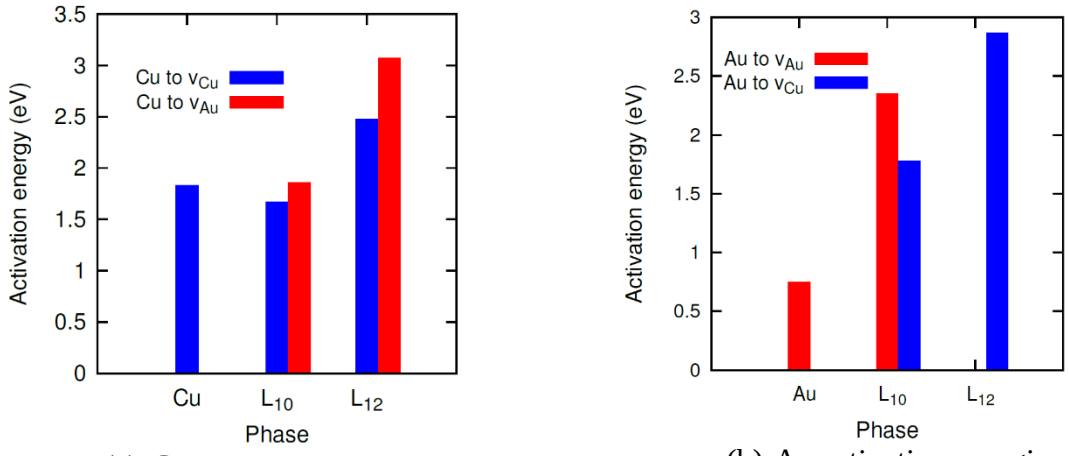

(a) Cu activation energies (b) Au activation energies

Figure 3-11. Activation energies for migration of (a) Cu and (b) in their respective single crystals, L_{12} and L_{10} phases.

The activation energy for Au self-diffusion (0.75 eV) in the single crystal is less than the activation energies for both Cu vacancy mediated and Au vacancy mediated diffusion in the L_{10}

phase, by 1.05 eV and 1.55 eV respectively. The self-diffusion activation energy of Au is also less than the activation energy of the Cu vacancy assisted diffusion path in L_{12} phase.

Although the migration barriers for Au vacancy assisted diffusion of Cu are lower than for Cu vacancy assisted diffusion in both L_{12} and L_{10} phases (Fig. 3-10(a) and Table 3-6), the high vacancy formation energies of Au leads to higher final activation energies for the Au vacancy assisted diffusion paths. Similarly, despite lower migration barrier for Au vacancy assisted diffusion of Au than its Cu vacancy assisted diffusion (Fig. 3-10(b) and Table 3-6) in the L_{10} phase, the final activation energy for Cu vacancy assisted diffusion path is lower because of easy formation of vacancy of Cu (lower vacancy formation energy than Au).

In conclusion, the Cu vacancy assisted diffusion path is the dominant mechanism for both Cu and Au diffusion in the L_{12} and L_{10} phases, while Cu vacancy assisted diffusion is the only possible mechanism of Au diffusion in the L_{12} phase. Also, the Cu vacancies are more diffusive than the Au vacancies in both L_{10} and L_{12} structures. This could be consistent with Kirkendall diffusion, where Cu diffusion is preferred over Au diffusion in the Cu-Au alloys.

3.3.7 Diffusion in Disordered Cu-Au

Cu and Au atoms are miscible over the entire stoichiometric range above 400° C, forming fcc alloy structures. Diffusion in these solid solution alloys are hence modeled using the SQS structures, as they are widely used to represent disordered alloys. The local environment of every atom in an SQS structure is different, unlike in an ordered structure. Diffusion will be via a vacancy mechanism as in the pure metals. The vacancy formation energy in a concentrated alloy is dependent on its local environment. Therefore, the formation energies are classified according to the first nearest neighbor atoms *(m,n)* around the vacancy, where *m* is the number of Cu atoms and *n* is the number of Au atoms. Multiple points are shown for the same *(m,n)* in Fig. 3-12;

these differences presumably arise from differences in the arrangements of each species within the nearest neighbor shells and differences in the numbers and arrangements of Cu and Au atoms in the second neighbor shells and beyond.

It can be seen from Fig. 3-12 that the vacancy formation energies of Cu and Au in $Cu_{0.5}Au_{0.5}$ SQS are comparable, with Au formation energies being only slightly higher than those of Cu. The formation energies are calculated using Eq. 3-2, where the chemical potential from the pure metal reference states is used. The formation energies of Cu and Au exhibits the same trend; that is, they increase as the nearest Au neighbors decrease. These results indicate that both Cu and Au vacancies prefer a Au rich local environment. Also, the vacancy formation energy of Cu is higher and that for Au is lower than in its ordered L_{10} counterpart, as can be seen from Fig. 3-12. This indicates that the solid solution of Cu-Au tends to decrease the vacancy concentration of Cu and increase that for Au than in ordered structure. Moreover, the formation energies are much higher in SQS than those in pure Cu (1.08 eV) and pure Au (0.45 eV) indicating that the formation of alloys makes Cu and Au more resistant to vacancy formation.

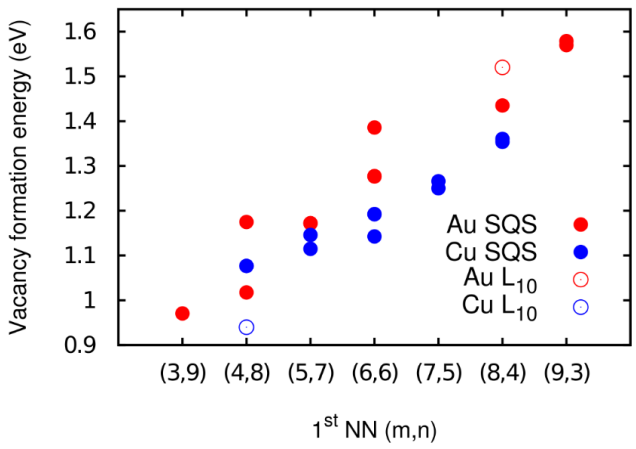

Figure 3-12. Dependence of vacancy formation energies of Cu and Au in the $Cu_{0.5}Au_{0.5}$ SQS-structure on the number of its nearest neighbor pair (m,n), where m is the number of Cu and n is the number of Au atoms in the 1st NN shell of the vacancy. The formation energies in the L_{10} structure are also shown in the corresponding 1st NN shells for a comparison.

Following the formation of a vacancy, there could be 12 distinct migration jumps of either Cu or Au into that vacant site. However, since the structure is disordered, it is not possible to classify vacancies as Au or Cu vacancies.

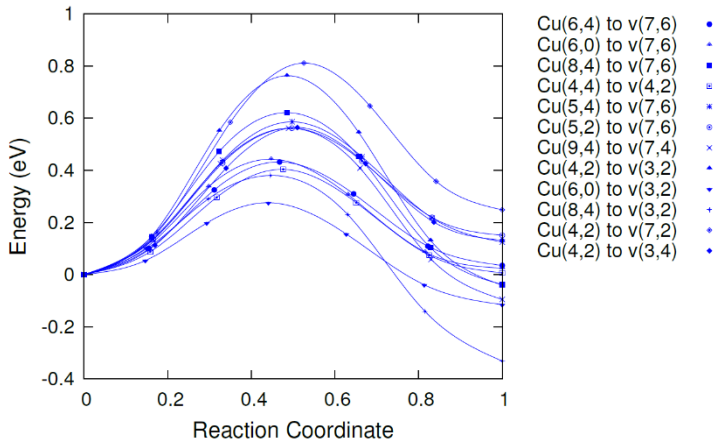

(a) Cu MEPs

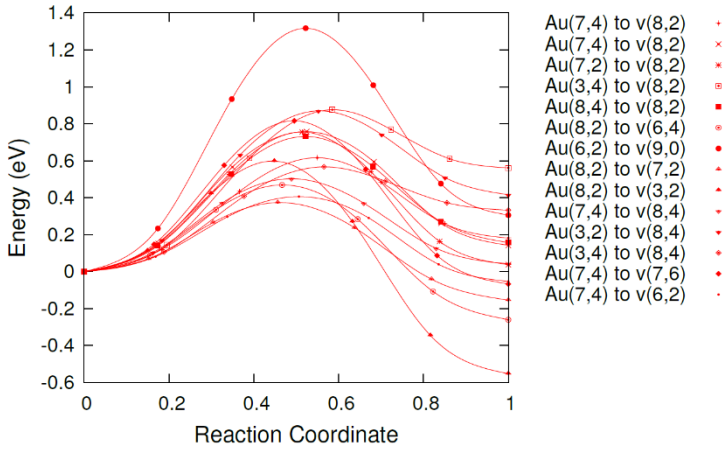

(b) Au MEPs

Figure 3-13. MEPs of (a) Cu and (b) Au in the $Cu_{0.5}Au_{0.5}$ SQS structure. Numbers in brackets denotes the number of Au atoms present in the first and second nearest neighbor shells of the migrating specie and the vacant site the atoms are migrating to.

In this work, a 32-atom $Cu_{0.5}Au_{0.5}$ SQS structure is used to model the MEPs. Since there are 12 different possible vacancy diffusion jumps for each of the 16 atoms of Cu and Au, there are 384 distinct barriers. We have sampled these barriers by performing NEB calculations on a

subset. Representative MEPs for both Cu and Au are represented in Fig. 3-13(a) and Fig. 3-13(b) respectively and categorized by the number of Au atoms present in the first and second nearest neighbor shells of the migrating species and the vacant sites into which the atoms are migrating.

A wide range of migration barriers for both Cu (0.27-0.81 eV) and Au (0.40-1.31 eV) can be clearly seen in Fig. 3-13(a) and Fig. 3-13(b) respectively. Each NEB calculation provides two migration barriers for the vacancies, that is, forward and reverse barriers. The final activation barriers are calculated by adding the migration barriers and vacancy formation energies, for all the cases in Fig. 3-13. The vacancy formation energies for the final and initial states will be different, and thus only the forward states are considered to obtain the activation energies.

The activation energies for both Cu and Au diffusion in the SQS show a normal distribution as can be seen in Fig. 3-14. Interestingly, the mean (μ) and standard deviation (σ) for Cu (μ=1.82, σ=0.21) and Au (μ=1.84, σ=0.23) activation energies are almost identical. This could be a result of the absence of a distinction between self-diffusion and anti-site diffusion of the species, unlike in the ordered alloys. Also, the non-uniform gradient of chemical composition in random alloys leads to a wide range of migration barriers for both Cu and Au vacancies.

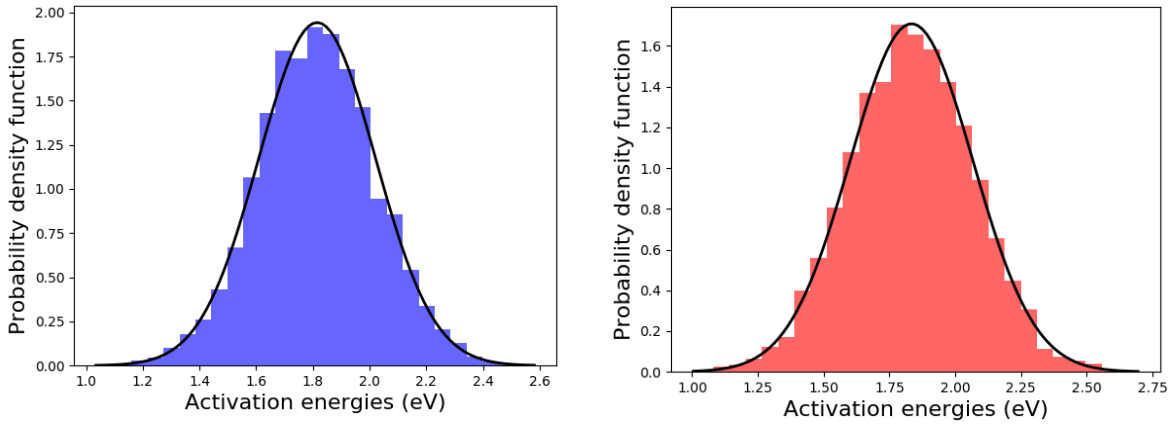

(a) Cu activation energies

(b) Au activation energies

Figure 3-14. Normal distribution fits of (a) Cu activation energies (b) Au activation energies in the $Cu_{0.5}Au_{0.5}$ SQS structure.

In conclusion, the defect energetics and diffusion behavior of Cu and Au are very similar in the solid solution. Both the vacancy formation energies and migration barriers depend on local environment, and the activation energies exhibit a normal distribution. The mean of the activation barriers for Cu and Au diffusion differs by only 17 meV.

3.4 Conclusions

A systematic investigation of thermodynamic and kinetic processes driving the evolution of Cu-Au alloys was carried out using first principles calculations. The ground state predictions of Cu-Au system (Cu_3Au, Cu_2Au, $CuAu$, Cu_2Au_3 and $CuAu_2$) using GGA-PBE level of theory are consistent with previous theoretical results, with Cu_3Au and $CuAu$ also being the experimentally observed phases. Cu rich phases are more stable as L_{12} type structures while Au rich phases stabilize in the L_{10} type configuration. The smaller Cu atoms are highly strained when their planes are placed next to each other i.e. in the L_{10} type layered configuration. This causes their energies to lie far above the hull. Mixed planes of Cu and Au reduces the strain on Cu atoms. In the Au rich domain, bigger Au atoms and smaller Cu atoms can easily be placed as pure alternating layers without any strain penalties.

A thorough investigation was done to disentangle the Au-rich region of the phase diagram and it was found that numerous phases lie extremely close to the hull. All these metastable Au-rich phases were found to be superstructures of the layered L_{10} phase. Metastable phases between each pair of ground states in the Au-rich region were closely studied and it was found that phases between $CuAu$ and Cu_2Au_3 ground states lie above the hull by only 0.25 meV, and those between Cu_2Au_3 and $CuAu_2$ lie above the hull by <3 meV. These phases are quite likely to be manifested experimentally as the room temperature corresponds to 25 meV.

Epitaxial calculations were performed on the Cu-Au ordered ground states with Au as the underlying substrate. Cu rich phases (Cu_3Au and Cu_2Au) destabilize when grown epitaxially on Au substrate, while the CuAu and Au rich phases (Cu_2Au_3 and $CuAu_2$) remain stable depending on the growth plane. These results thus confirm the following two experimental observations: (1) nucleation of Au-rich bimetallic alloy concurrently with the reduction of Cu_2O to metallic Cu, independent of Cu content of the system (2) selective etching of Cu from the Cu-Au intermetallic matrices. There is a transition from (100) to (001) stable growth plane when moving from the L_{10} CuAu phase to other Au rich phases. This transition is a result of the minimization of the strain energies, when the underlying substrate is Au.

Vacancy mediated NEB calculations were performed on the Cu-Au ordered and disordered (SQS) structures to identify the transitions states in each minimum energy path. Moreover, activation energies of diffusion were determined by adding the migration barriers and vacancy formation energies. The activation energies for diffusion of Cu vacancies are lower than those for Au, in both L_{12} and L_{10} phases. This is a clear indication of the unequal rates of diffusion in intermetallic matrices, the Kirkendall effect. Although the migration barriers of Au vacancies are in general lower than those of Cu, the higher vacancy formation energy of a Au vacancy leads to higher activation energies for Au vacancy diffusion than Cu vacancy diffusion. Diffusion is a thermally activated process, and it requires more thermal energy to form Au vacancies than Cu vacancies, in the Cu-Au intermetallics.

The vacancy formation energy of Cu and Au is a distribution of the local environments of a vacancy. The formation energies of both Cu and Au vacancies increases as the number of Au atoms in their 1^{st} NN shell decreases. Also, the formation energy of a Au vacancy is higher than for a Cu vacancy in any given local environment, and the difference could be up to 0.3 eV. In

conclusion, both Cu and Au vacancies prefers a Au rich environment and the thermal activation cost of Au vacancy formation is more than that for Cu vacancy formation. The migration barriers of Cu and Au atoms in the $Cu_{0.5}Au_{0.5}$ disordered alloy (SQS) show a wide distribution with different local environments of vacancies. However, the activation energies for both Cu and Au diffusion show a normal distribution with similar mean values. The non-distinguishable self-diffusion and anti-site diffusion of the species in disordered alloys unlike their ordered counterparts could be a reason for the essentially identical normal distributions for Cu and Au activation energies in $Cu_{0.5}Au_{0.5}$ SQS.

CHAPTER 4
SEQUESTRATION OF RADIONUCLIDES IN METAL-ORGANIC FRAMEWORKS (MOFs)[†]

4.1 Background

The nuclear waste by-products of nuclear power generation and medical isotope production have been one of the most challenging waste types to manage [3]. The radioactivity hazard does reduce over time depending on the decay rate of radionuclides in the waste to stable isotopes; however, this process can take millennia [3]. The nuclear wastes are generally classified into three major categories: low-level waste (LLW), high-level waste (HLW), and transuranic (TRU) waste [3,35]. The focus of this work is on the radionuclides in TRU and on Tc.

The state-of-the-art approaches to radionuclide immobilization such as glass and cement wasteforms [3,35] suffer from a number of limitations. These limitations include volatility, low solubility of constituents and partial crystallization, which compromise the long-term performance of these waste forms. Moreover, off-gas management becomes a problem for waste constituents with high vapor pressures and low melt solubilities [35]. Metal-organic frameworks (MOFs), a class of hybrid materials constructed from inorganic building units and organic linkers, have been recently identified as potential material systems for selective radionuclide sequestration, separation, or sensing [18,35,103,104]. Significant research has been reported on MOFs for gas storage, sensing, and heterogenous catalysis [105–109]; however, radionuclide-incorporated MOFs are relatively unexplored. The unique and desirable properties of MOF structures, including high porosity, modularity, synthetic diversity, high surface area, and low

[†] The work described in this chapter has been published in S. Pandey, Z. Jia, B. Demakse, O.A. Ejegbavwo, W. Setyawan, N. Shustova, S.R. Phillpot, Sequestration of Radionuclides in Metal-Organic Frameworks from Density Functional Theory Calculations, J. Phys. Chem. C. 123 (2019) 26842-26855. doi:10.1021/acs.jpcc.9b08256.

structural density, make them attractive candidates to contain the radionuclides [35]. One of the main advantages of MOFs is also the possibility of post-synthetic modification, i.e., the formation of covalent bonding with guests such as radionuclides, whose leaching from the framework can be significantly impeded [35]. Moreover, the potential for a more homogeneous distribution of radionuclides in their structures should decrease the accumulation of radiation damage caused by the formation of vacancies and defects [35,103].

Radionuclide sequestration in MOFs can occur through three main routes: (1) cation exchange at the metal node, (2) coordination to the organic-linker, and (3) capture in the framework pores (cavity) [18,35,110]. In this chapter, we investigate the thermodynamics of cation exchange in Zr-, U-, and Th-based MOFs using density functional theory (DFT) calculations. The ion-exchange technique referred to in this work differs from the traditional ion-exchange process [111–113], where a guest molecule in the MOF is exchanged by a target molecule. For example, Sheng et al. [111] have reported uptake of aqueous target TcO_4^- anion, which exchanges with NO_3^- and SO_4^{2-} in a Ni^{2+} MOF (SCU-102). These target molecules bind to the open channels in the MOF structure, rather than replacing the metal nodes, as in this work. The binding energy of such target molecules with the MOF have been calculated, whereas, in this work, we calculate substitution energies for the exchange of metallic ions in the MOF with target radionuclides to predict the favorability of ion-exchange.

The radionuclides of interest in this work are Tc, U, Th, Am, and Cm. We analyze the results of various DFT methods in order to establish the robustness of their prediction in the chemistries of these transition metals and actinides. The DFT methods evaluated include (1) exchange-correlation (XC) functionals at various levels, (2) DFT+*U* to account for on-site Coulomb interactions of localized electrons, (3) spin-orbit coupling (SOC) to account for

relativistic effects, and (4) effects of spin-polarization. Moreover, we also investigate various reference states for the exchanged ions (vacuum, continuum dielectric medium, and hydrated ions) so as to provide reliable estimates of ion-exchange reaction enthalpies. Finally, we relate the thermodynamic preferences for substitution of radionuclides in the very stable Zr-, U-, and Th-based MOFs [110,114], to experimental results of Ref. [103,110].

4.2 Structures and Computational Methods

4.2.1 MOF Structures

The studied MOF system consists of M_6 clusters (where M = Zr, Th, or U) coordinated to eight (8-connected) or ten (10-connected) Me_2BPDC^{2-} organic linkers (Me_2BPDC^{2-} = 2,2′ -dimethylbiphenyl-4,4′ -dicarboxylate). The M_6 cluster is also referred to as the metal node or the secondary building unit (SBU). In the case of the 8-coordinated MOF SBU, each metal cluster is connected to eight Me_2BPDC^{2-} linkers and terminal hydroxyl groups in the equatorial plane (Fig. 4-1(a)). This topology provides an opportunity to post-synthetically install the additional linkers, i.e., “capping linkers” [103]. The 10-coorodinated SBU is connected to eight Me_2BPDC^{2-} linkers above and below the equatorial plane, in addition to two Me_2BPDC^{2-} linkers and terminal hydroxyl/nitrate groups in the equatorial plane (Fig. 4-1(b)) [110].

For a simplified description and theoretical analysis of the MOF extended structure, a unit cell consisting of 292 atoms is considered (Fig. 4-2). This unit cell consists of six M_6 clusters, four of which lie in the equatorial plane and are connected above and below to the other two axial clusters (Fig. 4-2). Within each SBU, there are two distinct metal positions (equatorial and axial), each of which possess a different coordination environment. Fig. 4-3 shows the distribution of the six metal atoms present in the SBU across six metal sites. However, axial positions 1 and 2 are equivalent, while equatorial positions 3, 4, 5, and 6 are equivalent too. In

each of the metal clusters, the six metal atoms are coordinated to oxygen atoms of the Me_2BPDC^{2-} carboxylate groups. Thus, the four equatorial metal atoms are coordinated to six oxygen atoms, while the two axial metal atoms are coordinated to eight oxygen atoms (Fig. 4-3). The two axial SBUs are linked to each of the four equatorial SBUs via the carboxylate functionalized Me_2BPDC^{2-} organic linker.

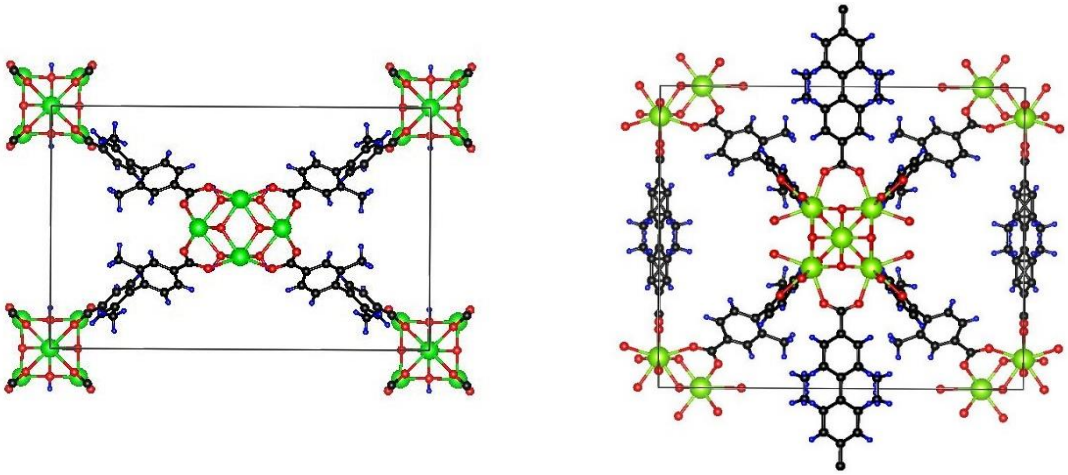

(a) 8-coodinated MOF (b) 10-coordinated MOF

Figure 4-1. Extended MOF structures with the M6 clusters (SBUs) coordinated to (a) eight Me_2BPDC^{2-} linkers (b) ten Me_2BPDC^{2-} linkers. The green, red, black, and blue spheres represent the metal, oxygen, carbon and hydrogen atoms, respectively. The black box denotes the edges of the unit cell.

In our work, we initially focused on the truncated model of the MOF (Fig. 4-3) as it was previously reported in the literature [103]. For that, we replaced the eight or ten Me_2BPDC^{2-} linkers coordinated to the metal cluster with carboxyl groups (−COO−) [103]. The resulting eight- and ten-coordinated SBUs are referred to as M-8 and M-10 SBUs respectively. As shown in Fig. 4-3(a), each of the selected M-8 SBU is composed of 46 atoms, comprising of six metal atoms, two in the axial position (labeled 1 and 2) and bonded to eight oxygen atoms and four in the equatorial position (labeled 3, 4, 5, 6) bonded to six oxygen atoms. Four of the eight oxygen

atoms bonded to the metal atom at position 1, and two out of six oxygen atoms bonded to the metal atom at position 3 are further bonded to carbon atoms, terminated by hydrogen atoms. Thus, all of the ions except the terminating hydrogen atoms are part of the MOF structure. This technique retains the charge neutrality of the MOF as explained later in this section.

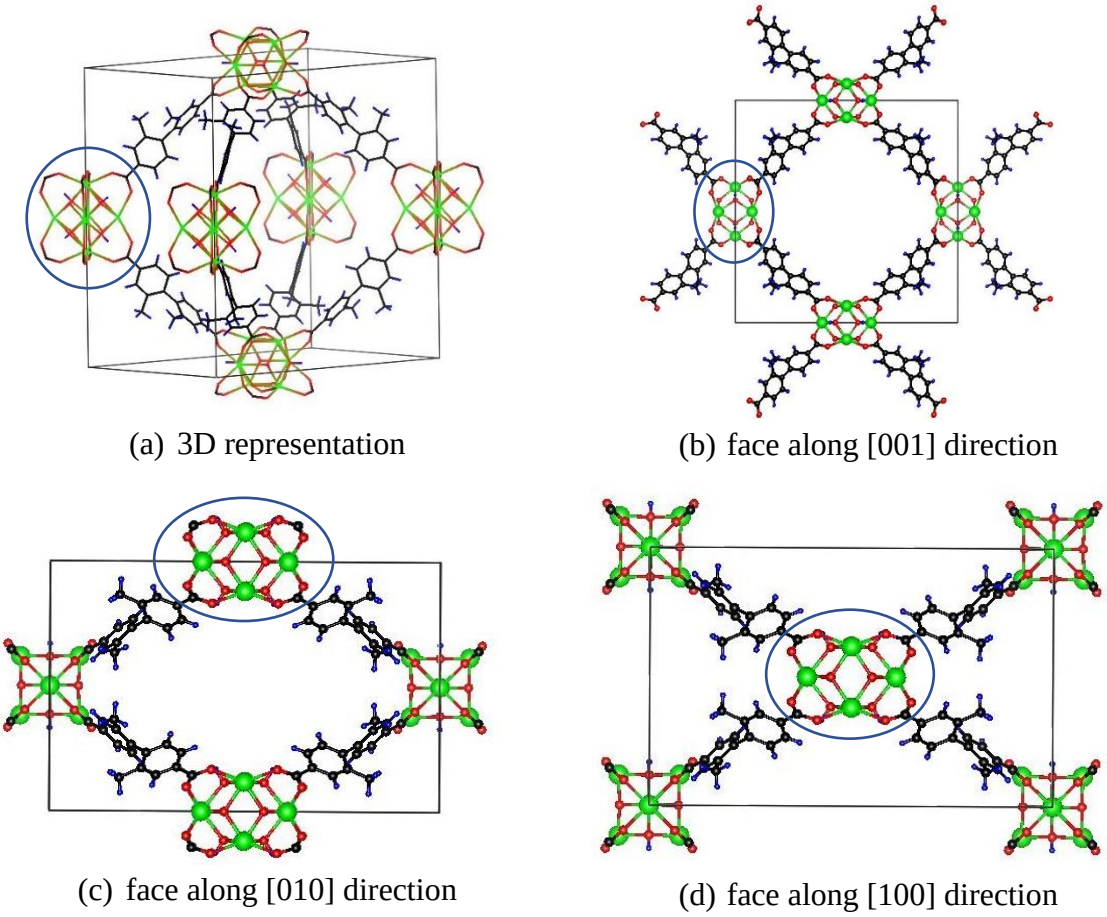

(a) 3D representation (b) face along [001] direction

(c) face along [010] direction (d) face along [100] direction

Figure 4-2. (a) 3D Structural representation of a unit cell of the MOF extended structure consisting of 292 atoms, showing the four equatorially and two axially positioned M6 metal clusters. (b) The MOF unit cell faced along [001] direction (c) faced along [010] direction (d) faced along [100] direction, also along the direction of the pore. The SBUs are encircled in each figure. The green, red, black, and blue spheres represent the metal, oxygen, carbon and hydrogen atoms, respectively. The black box denotes the edges of the unit cell.

A corresponding process for the M-10 cluster also allows for the selection of a suitable SBU. The M-10 SBU (Fig. 4-3(b)) is composed of 56 atoms in total, of which six are metals: two

metal atoms are bonded to eight oxygen atoms and four metal atoms are bonded to seven oxygen atoms. It can be described as an M-8 structure with two additional –(COO)– groups attached to the six coordinated metal atoms of M-8 SBUs. Thus, four parent MOF SBUs: Zr-8, U-8, Th-8, and Th-10 will be discussed in the presented studies.

All the considered SBUs are charged neutral and for simplicity can be viewed as a combination of M^{4+} metal ions, units of –(COO)– formic acid, hydroxyl $(OH)^-$ functional groups, and O^{2-}. Indeed, the neutral M-8 SBU is a combination of 6 M^{4+} (charge = +24), 8 –(COO)– units (charge= –8) and 8 O^{2-} anions (charge = –16). Similarly, the neutral M-10 MOF SBU is a combination of 6 M^{4+} metal ions (charge= +24), 10 –(COO)– units (charge = –10), 2 $–(OH)^-$ units (charge= –2), and 6 O^{2-} anions (charge= –12). Thus, one formula unit (f.u.) stoichiometries of M-8 and M-10 SBUs are $M_6(COOH)_8O_8$ and $M_6(COOH)_{10}(OH)_2O_6$, respectively.

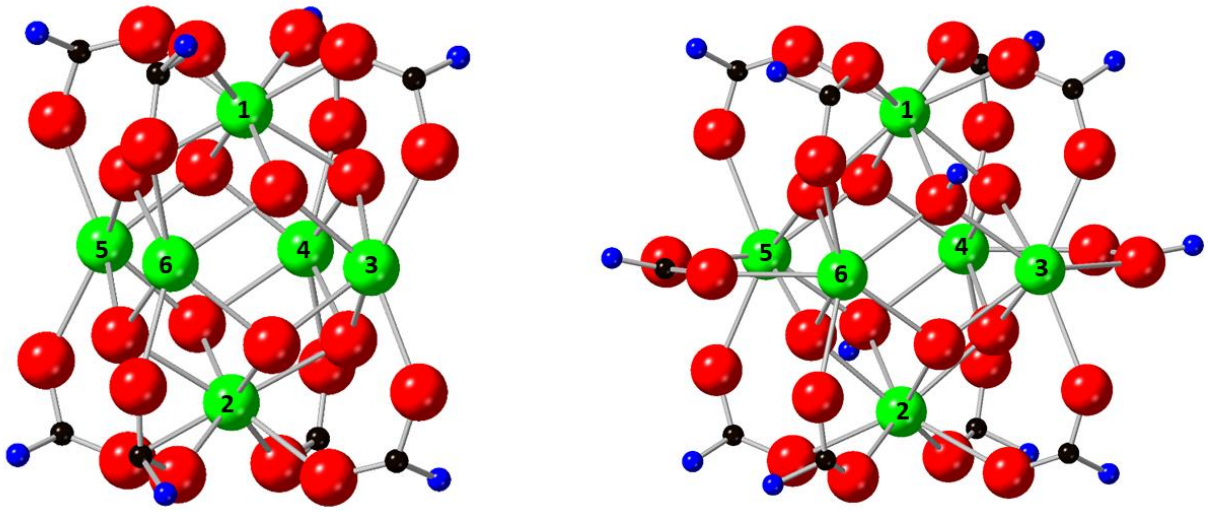

(a) M-8 SBU (b) M-10 SBU

Figure 4-3. The models of SBUs: (a) M-8 (b) M-10. The green, red, black, and blue spheres represent M, O, C, and H, respectively. The metal atoms located in 1 and 2 positions possess the same coordination environment, and the metal atom positions in 3,4,5, and 6 possess the same coordination environment too.

To assess the reliability of calculations for the SBU, we replicated a MOF structure with an 8-connected SBU through connection of metal nodes with parts of organic linkers as shown in Fig. 4-4. Each of metal node connects to eight Me_2BPDC^{2-} but instead of the structure of the Me_2BPDC^{2-} linker, we have utilized only a part of it to decrease a number of atoms. In this truncated MOF structure, the metal cluster (SBU) is coordinated to eight linkers, each of which contains just one phenyl ring (Fig. 4-4). From now on, we are going to refer this truncated model as "truncated MOF-2." Truncated MOF-2 consists of 150 atoms and can be described as an extension of the terminal carbons of 46 atom SBU with one benzene ring each. These extra benzene rings are further terminated by hydrogens to saturate the carbons.

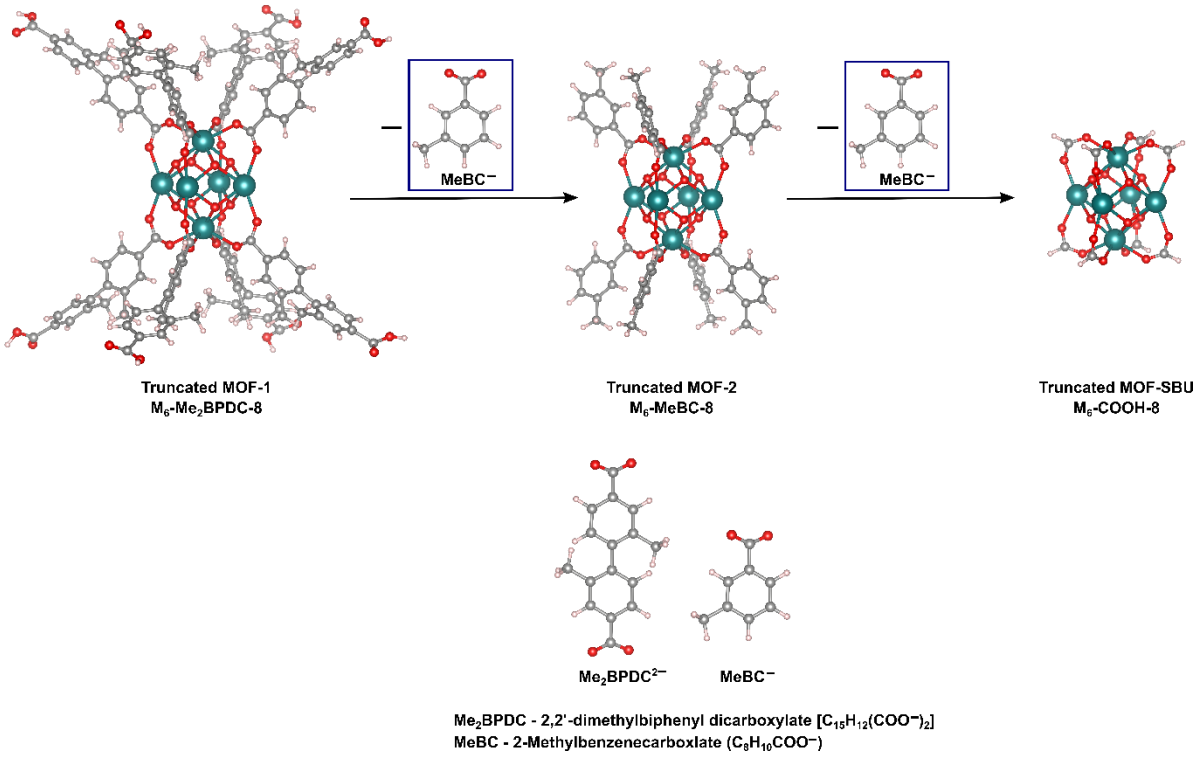

Figure 4-4. Strategic design for retaining MOF structural components (SBU and linker) while reducing the number of atoms per unit for effective theoretical calculations.

4.2.2 DFT Methods

The DFT calculations were performed using the Vienna *ab initio* simulation package (VASP) [82,83] with plane-wave basis sets. Projector-augmented wave (PAW) [68,84] pseudopotentials were employed, with the electrons described explicitly being Zr ($4s^2 5s^2 4p^6 4d^2$), U ($6s^2 7s^2 6p^6 6d^1 5f^3$), Th ($6s^2 7s^2 6p^6 6d^1 5f^1$), Tc ($4d^5 5s^2$), Am ($6s^2 7s^2 6p^6 6d^1 5f^6$), Cm ($6s^2 7s^2 6p^6 6d^1 5f^7$), C ($2s^2 2p^2$), O ($2s^2 2p^4$) and H (1s); that is 12, 14, 12, 7, 17, 18, 4, 6 and 1 electron, respectively. All these potentials were taken from the potpaw_PBE.54 library of VASP. The plane-wave energy cutoff was set to 520 eV and all calculations were performed at the Γ-only. Structural optimization was performed until the forces on each ion were less than 25 meV/Å, using 0.0001 eV as the energy tolerance for each electronic step. Gaussian smearing with a width of 0.05 eV was applied to all optimizations. A conjugate-gradient algorithm [91,92] was used to relax all the ions. Both spin-polarized and non-spin polarized calculations were performed in order to determine the effect of spin on the energetics of substitution and electronic structure. The relativistic effects were investigated using spin-orbit coupling calculations [69]. Various levels of exchange-correlation functionals were used, these are, in approximately increasing order of sophistication and computational cost: GGA-PBE [41], meta-GGA (TPSS [115], rTPSS [115] and SCAN [55]) and hybrids (B3LYP [60] and PBE0 [61]) to evaluate the robustness of the results for the Zr-MOF. Following this, GGA-PBE was found to be adequate for the defect energetics calculations. Therefore, all the other structures were optimized using only GGA-PBE. The van der Waals (vdW) interactions were taken into account using the dispersion correction formula in the PBE-D3, B3LYP-D3, etc. functionals by Grimme et al. [116] with Becke-Johnson damping [117], and the rVV10 [118] vdW formalism for the SCAN functional. Additionally, DFT+*U* corrections were also analyzed using the Dudarev et al.

formalism [64] in order to better describe the strong correlation of *d* and *f* electrons. Atomic charges were determined using the Bader charge analysis code [119–122].

Three types of reference states for ion-exchange were considered: (1) individual metal ions (M^{4+}) isolated in vacuum, (2) M^{4+} ions isolated in a continuum water medium (using the room temperature dielectric constant of water=78.54 [123]), and (3) hydrated M^{4+} ions i.e. ion-water complex $[M(H_2O)_n]^{4+}$. The image charge correction due to periodic boundaries was taken into account for the ions, by calculating the full dipole moment in all directions [124]. A cubic box of size 30 Å was used to isolate the ions. The ions were electronically converged for a single point calculation using the same pseudopotentials as for the corresponding MOF structures. The MOF cluster SBUs were treated as non-periodic and were equilibrated in a box sized 30 Å with vacuum. This method of treating the full crystalline MOFs as their SBUs is well established [125–127] and reduces the computational cost significantly. The box size was varied from 10-30 Å for both ions and MOF clusters to test for convergence.

Hydration energies of the $[M(H_2O)_n]^{4+}$ ion-water clusters were calculated for n=1 to 20, to ascertain the correct trends of the energies of hydrated ions to be used as reference energies. The hydration energies were calculated in both Gaussian09 [128] and VASP software packages to establish robustness in the results. B3LYP level of theory with basis sets of LANL2DZ (Tc, Zr), SARC [129] (U, Th) and 6-31G(d) (O, H) in Gaussian09, and GGA-PBE level of theory with plane-wave basis sets in VASP were used for geometry optimization of the $[M(H_2O)_n]^{4+}$ clusters. The binding energies of the ions with water molecules were then calculated as described below in section 4.3.7.

4.2.3 Energetics of Ion-Exchange

Energies of substitution (substitution energies) are calculated in four parent MOFs: Zr-8, U-8, Th-8, and Th-10, with Tc, Am, Cm, Th and U as the substituting species. All these substitutions occur via a chemical reaction in which the substituting species (4+ metal ions) goes into the parent MOF and replaces its metal ions at various positions. The substitution energy is calculated using the standard difference between the energies of products and reactants. An illustrative example for Th substitution in Zr-8 MOF is,

$$Zr_6(HCO_2)_8O_8 + Th^{4+} \rightarrow ThZr_5(HCO_2)_8O_8 + Zr^{4+} \quad (4\text{-}1)$$

The free energies of substitution, $E_{substitution}$, have been calculated with reference to the isolated ions (in vacuum) in the usual manner [103] according to,

$$E_{substitution} = \left(E_{(An)SBU} - E_{SBU}\right) + N \times \left[E_{parent\ M^{4+}} - E_{substitute\ An^{4+}}\right] \quad (4\text{-}2)$$

where, $E_{(An)SBU}$ = is the energy of the SBU structure with *N* substituted ions, E_{SBU} = energy of the unsubstituted SBU, $E_{\text{parent } M^{4+}}$ is the energy of isolated ion removed from the unsubstituted SBU, and $E_{\text{substitute } An^{4+}}$ is the energy of isolated ion that is substituted into the SBU.

In the case of hydrated ions, the M^{4+} and An^{4+} reference states changed to $[M(H_2O)_n]^{4+}$ and $[An(H_2O)_n]^{4+}$ as described below in section 4.3.7.

4.3 Results: Structural Analysis and Evaluation of DFT Methods

4.3.1 Structural Analysis

The structure optimization of MOFs is discussed from a metal-oxygen bond length analysis. As shown in Table 4-1, in each case the GGA+*U* optimized M-O bond length was longer for the 8-fold coordinate M atoms at position 1 than for the 6-fold coordinated M atoms at position 3. This dependence on coordination is expected. These bond lengths were found to be similar to the bond lengths in the corresponding M-oxides with the same coordinations: ZrO_2,

UO_2, and ThO_2 for 8-fold coordination and the 6-fold coordinate U atoms in U_3O_8 for 6-fold coordination. This strongly suggests that the immediate coordination of metal plays a dominant role to determine the bond length.

Table 4-1. GGA+*U* optimized bond lengths of M-O in MOFs at two different positions, compared to the bond lengths in their corresponding bulk oxides. Numbers in brackets denotes the coordination number of M. [U-J: Zr(4d) =4 eV, U(5f) =4 eV, Th(5f) =6 eV]

M-O	Average M-O bond length (Å)		
	MOF (8 and 6)		Oxide (MO_2); M_3O_8
	position 1	position 3	
Zr-O (Zr-8)	2.23 (8)	2.12 (6)	2.23 (8) [130]
U-O (U-8)	2.38 (8)	2.27 (6)	2.37 (8) [131] ; 2.12 (6) [132]
Th-O (Th-8)	2.46 (8)	2.36 (6)	2.43 (8) [133]
Th-O (Th-10)	2.44 (8)	2.38 (7)	

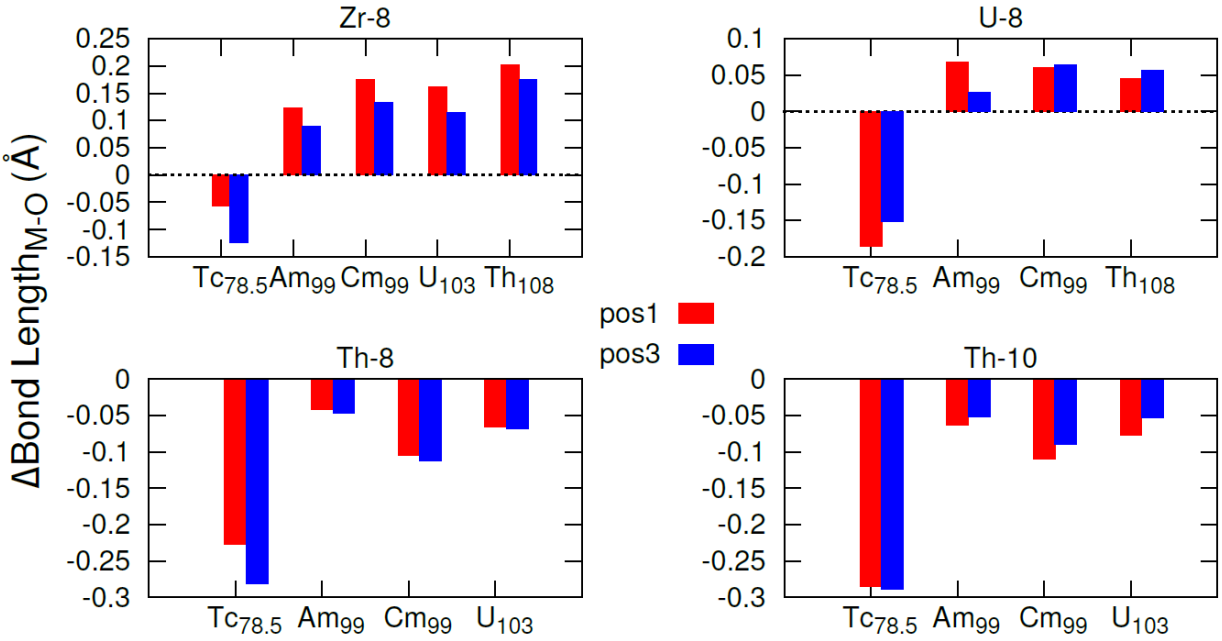

Figure 4-5. Change in M-O bond length after substitution with respect to the M-O bond length in parent MOFs at position 1 and position 3, with the ionic (IV) radius of substituting species. The subscripts on the atom symbols show the ionic radii in pm.

Fig. 4-5 shows the change in the metal-oxygen (M-O) bond length on substitution as a function of the ionic (IV) radius [134] of the substituting species, in the four parent MOFs. The trends in differences are the most prominent in Zr-8 MOF, due to larger differences in sizes of

parent Zr^{4+} ion (86 pm) and substituting species. Tc^{4+} being the smallest ion decreases the bond length the most in all the MOFs, by up to ~0.3 Å. The ionic radii of Am^{4+}, Cm^{4+}, U^{4+}, and Th^{4+} are similar to each other (99-108 pm) and thus shows similar deviations lying in the range of 0.1-0.2 Å in the Zr-8 MOF, and even smaller changes, <0.1 Å, in U and Th MOFs.

The substitution energetics of Zr-8 SBU were first determined using GGA-PBE level of theory and taking Dolgopolova et al. [103] as a reference (Table 4-2). The substitution energies are reproduced within an error of 4%. All of the energies are positive indicating unfavorable substitution of U and Th in the Zr-8 MOF. To characterize the robustness of the results among different flavors of DFT, these formation energy values were also calculated using various exchange-correlation functionals. In approximately increasing level of sophistication, and computational cost, these are GGA-PBE, meta-GGAs (TPSS, rTPSS and SCAN), and hybrid functionals (B3LYP and PBE0), as described in section 4.2.2. The effect of *d*- and *f*-electron localization were characterized using various values of *U*-*J* in DFT+*U* corrections. The effects of spin were characterized using GGA-PBE functionals with and without spin-polarized calculations. Relativistic effects were investigated using spin-orbit coupling calculations.

Table 4-2. GGA-PBE (D3) calculated substitution energies in Zr-8 MOF, compared to the literature for Positions 1 and 3, and when all 6 Zr atoms were replaced by U or Th. Positive substitution energies disfavor substitution.

Actinide	Position type	Substitution energy (eV)	
		This work	Literature [103]
U	1	8.25	7.99
	3	8.80	8.49
	all 6	51.95	50.12
Th	1	9.85	9.61
	3	10.82	10.47
	all 6	63.49	61.65

4.3.2 Effect of System Size on Substitution Energies

To quantify the effects of using only the SBU for calculations, the formation energies for the Zr-8 MOF were calculated in the 292-atom full crystalline MOF, in the 150-atom truncated MOF-2 model and the 46-atom SBU. As Table 4-3 shows for the case of Th substitution, the calculated substitution energy varies by less than 3.5%. While the coordination of the metallic species is the same for all the system sizes, the structural differences, mostly arising from the complexity of benzene rings, are presumably the reason for the different substitution energies. Nevertheless, since the sign of formation energies is robust for different MOF structure sizes and because of the dramatically smaller computational cost, the smallest sized SBUs will be used to systematically investigate the substitution energetics.

Table 4-3. Comparison of GGA-PBE substitution energies of Th (position 1) calculated in the 292-atom unit cell, truncated MOF-2, and SBU structures.

Substituting Species	Substitution energy (eV)		
	Unit cell (292 atoms)	Truncated Zr-8 MOF-2 (150 atoms)	Zr-8 SBU (46 atoms)
Th at position1	9.62	9.96	9.85

4.3.3 Effect of Exchange-Correlation Functional on Substitution Energetics

Fig. 4-6 shows the substitution energies for Th in the Zr-8 MOF calculated using various exchange-correlation functionals, including GGA-PBE, meta-GGA, and hybrids. In the absence of vdW interactions, all methods give values within ± 1%, as shown by the blue bars. The vdW dispersion corrections result in a reduction of the predicted substitution energy by ~1-2% for each functional.

For all functionals, the substitution energy into the position 3 site is predicted to be larger than into the position 1 site. Since all functionals give similar substitution energies and similar differences in energies, we use GGA-PBE without vdW corrections, the computationally least expensive method, for subsequent formation energy calculations.

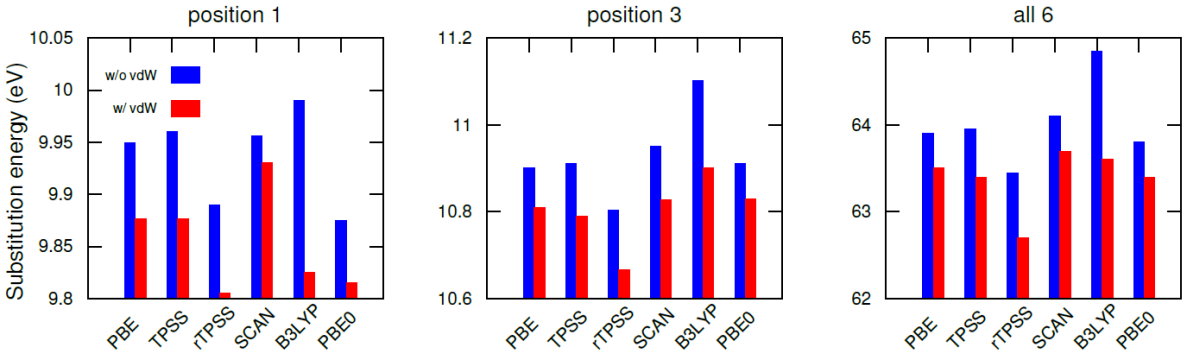

Figure 4-6. Substitution energies for Th in Zr-8 MOF calculated using GGA-PBE, meta-GGA and hybrid XC-functionals, at position 1, position 3 and all 6 positions. Blue bars denote without including van der Waals corrections and red bars with van der Waals corrections and red bars with van der Waals corrections.

4.3.4 Effect of Electron Localization

As indicated by previous studies on the oxides of Zr [130], U [63,135,136], Th [137], Tc [138], Am [137], and Cm [137], DFT+*U* corrections are needed to better describe their strongly correlated *d-*, *f-*, *f-*, *d-*, *f-, and f*-electrons respectively. Based on this argument, on-site Coulomb interaction parameters were added to Zr (4d), U(5f), Th(5f), Tc(4d), Am(5f), and Cm(5f) electrons, in the Dudarev et al. [64] formalism. Metal ions in Zr-MOF and U-MOF were treated with a *U-J* value of 4 eV and those in Th-MOFs with a *U-J* of 6 eV, as per the previous literature [130,135,137]. The substituting ions (Tc, Am, and Cm) were treated with the same *U-J* value as that of the parent ions in the MOF, to maintain consistency.

To investigate the effects of +*U* using GGA-PBE, substitution energies were calculated at position 1 in all the four parent MOFs. As Fig. 4-7 shows, the +*U* corrections could change the magnitude of the energies of various structures by a maximum ±40% in some cases. However, the sign of the substitution energy remains the same for all species. The absolute energy components in Eq. 4-2 increase with the addition of +*U*. However, the change is

essentially independent of the environment. Thus, the effect largely cancels out giving similar formation energies as the calculations without the $+U$ correction.

The degree of delocalization of electrons can be related to the orbital occupancies of metal ions as explained below. The GGA-PBE (U-J=0) calculated orbital occupancies for both up-spin and down-spin channels in Zr-8, U-8 and Th-10 MOFs (Th-8 behaves the same as Th-10) for parent metals and substituted ions (position 1) are given in Table 4-4. We also reproduced the orbital occupancies of Zr in La_2NiZrO_6 as demonstrated in Fuh et al. [138], for their U-J=0 case to establish the reliability of our method. We obtained up-spin and down-spin channel orbital occupancies of 0.83/0.82 which are consistent with their 0.84/0.81 occupancies within an error of 2.5%.

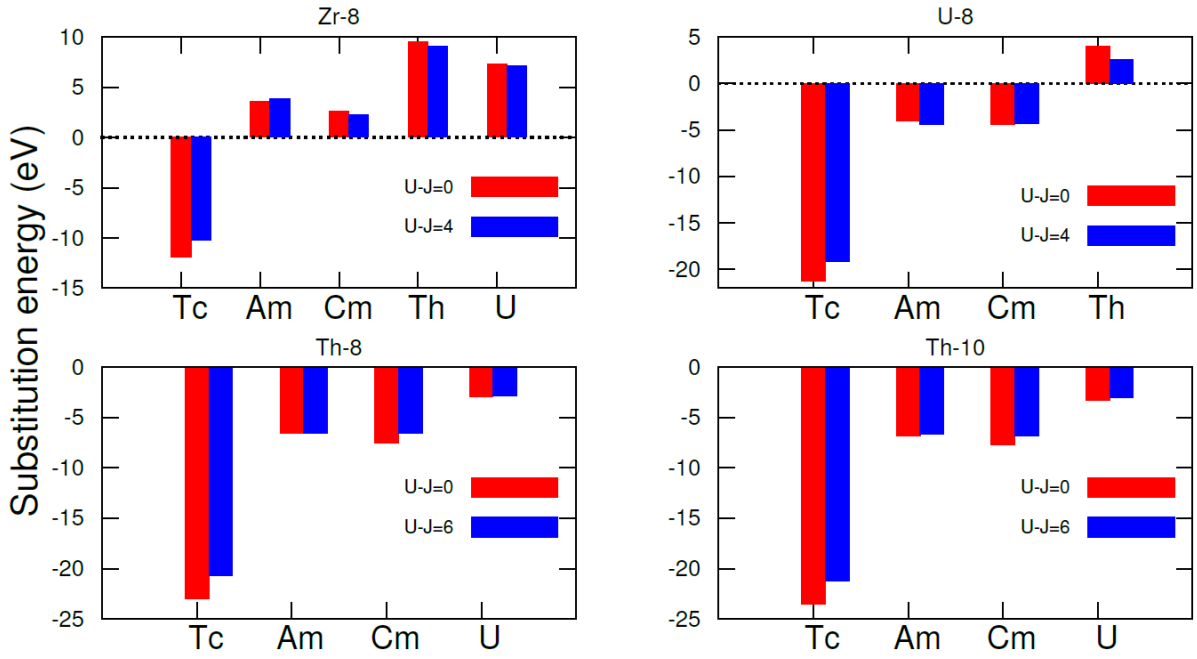

Figure 4-7. Effect of $+U$ corrections on substitution energies at position 1 in Zr-8, U-8 and Th-8 and Th-10 MOFs, using non-spin polarized GGA-PBE XC-functional.

The 4*d* orbitals of Zr atoms to which the *U-J* is applied have 2 valence electrons, indicating a formal valence configuration of Zr^{4+} in $Zr_6(COOH)_8O_8$ (Zr-8 SBU) as $Zr^{4+}(4d^0)$. However, the actual charge configuration of Zr is $Zr^{2.53+}(4d^{1.56})$ as per the calculated orbital occupancies and Bader charge analysis. The 4*d* orbitals of Tc atoms to which the *U-J* is applied have 5 valence electrons, indicating a formal valence configuration of $Tc^{4+}(4d^3)$. However, the actual charge configuration of Tc is $Tc^{1.87+}(4d^{5.13})$ Also, the weaker *d* interaction increases the localization of these orbitals. The change in formation energy for Tc substitution is the least (~9%) in U-8 and the two Th MOFs (~9%) and is the highest in Zr-8 MOF (20%). However, the absolute change is consistent in all the MOFs, increasing by ~2 eV. Similarly, the charge configurations of Am, Cm, U and Th in the Zr-8 MOF are $Am^{2.34+}(5f^{6.04})$, $Cm^{2.30+}(5f^{6.96})$, $U^{2.60+}(5f^{2.72})$ and $Th^{2.78+}(5f^{0.54})$ respectively. The orbital occupancies and charge states in U-8 and Th-10 MOFs can be seen in Table 4-4.

Am substitution shows the maximum change in formation energy in the U-8 MOF which is a decrease by ~10% (0.40 eV decrease), followed by in Zr-8 MOF (increase by 0.30 eV equivalent to 8.40%) and the least in Th MOFs (decrease by 0.03 eV equivalent to 0.4%). Cm substitution shows the maximum change in formation energy in the Th MOFs which is an increase by ~13.20% (1.00 eV increase), followed by in Zr-8 MOF (decrease by 0.40 eV equivalent to 15.00%) and the least in U-8 MOF (increase by 0.1 eV equivalent to 2.27%).

Table 4-4. GGA-PBE (*U-J*=0) calculated magnetic moments (μ_B/f.u.), up-spin and down-spin (↑/↓) orbital occupancies (Zr (*d*), Tc (*d*), Am (*f*), Cm (*f*), U (*f*), Th (*f*)), charge state of ions determined using Bader charge analysis, and difference between spin-polarized and non-spin polarized ($\Delta E_{Spin - non\text{-}spin}$) of parent MOFs (Zr-8, U-8 and Th-10) and position 1 substituted MOFs

System		Magnetic moment (μ_B/f.u.)			Orbital occupancy (↑/↓)		Charge state (Bader analysis)		ΔE (spin – non-spin) (eV)
		Parent M	Substituted ion	Total (net)	Parent M	Substituted ion	Parent M	Substituted ion	
Zr-8		0.00	-	0.00	0.78/0.78	-	+2.53	-	0.00
	Tc @pos1	0.04	2.32	2.78	0.76/0.78	(*d*) 1.43/3.70	+2.53	+1.87	-2.47
	Am @pos1	0.03	5.23	5.01	0.76/0.77	(*f*) 0.40/5.64	+2.53	+2.34	-3.51
	Cm @pos1	0.03	6.35	5.88	0.76/0.77	(*f*) 0.30/6.66	+2.53	+2.30	-5.01
	U @pos1	0.03	1.98	1.95	0.77/0.77	(*f*) 0.34/2.38	+2.53	+2.60	-0.80
	Th @pos1	0.00	0.00	0.00	0.77/0.77	(*f*) 0.27/0.27	+2.53	+2.78	0.00
U-8		11.91	-	11.29	0.43/2.40	-	+2.45	-	-2.37
	Tc @pos1	8.63	-3.07	4.80	0.62/2.18	(*d*) 1.86/3.52	+2.50	+1.61	-0.90
	Am @pos1	8.91	6.12	14.37	0.48/2.28	(*f*) 0.16/6.13	+2.52	+2.10	-5.91
	Cm @pos1	9.06	6.69	15.21	0.45/2.30	(*f*) 0.16/6.86	+2.50	+2.18	-8.34
	Th @pos1	9.86	0.02	9.35	0.40/2.42	(*f*) 0.26/0.27	+2.45	+2.78	-2.01
Th-10		0.00	-	0.00	0.25/0.25	-	+2.78	-	0.00
	Tc @pos1	0.06	2.35	2.80	0.25/0.26	(*d*) 1.41/3.71	+2.78	+1.80	-1.52
	Am @pos1	0.00	5.25	4.98	0.25/0.25	(*f*) 0.42/5.57	+2.78	+2.32	-3.56
	Cm @pos1	0.01	6.20	5.88	0.25/0.25	(*f*) 0.32/6.52	+2.78	+2.30	-4.73
	U @pos1	0.02	1.93	1.89	0.25/0.25	(*f*) 0.33/2.38	+2.78	+2.58	-0.87
Zr^{4+}		0	-	-	0/0	-	-	-	0.00
Tc^{4+}		1.53	-	-	0/2.84	-	-	-	-2.48
Am^{4+}		4.95	-	-	0/4.95	-	-	-	-3.98
Cm^{4+}		5.73	-	-	0/5.95	-	-	-	-5.62
U^{4+}		1.95	-	-	0/1.96	-	-	-	-0.28
Th^{4+}		0	-	-	0/0	-	-	-	0.00

U substitution shows consistent change with $+U$ corrections in Zr-8 and the two Th MOFs which is an increase of ~5% (or at the most 0.5 eV) in the formation energies. Moreover, the weak *d* interaction in transition metal based Zr-8 MOF decreases the Th substitution formation energy by only 0.9 eV or ~8.5%. This decrease is more significant (1.5 eV or ~37%) in U-8 MOF because of the strong delocalization of 5*f* orbitals of six U atoms before substitution and five after substitution.

Thus, GGA-PBE XC-functional without DFT+U corrections will be used for our subsequent substitution energetics.

4.3.5 Effect of Spin-Polarization

To determine the effects of spin, spin-polarized calculations with the GGA-PBE XC-functional without $+U$ corrections were performed on Zr-8, U-8 and Th-10 (Th-8 behaves same as Th-10) MOF SBUs. Fig. 4-8 shows substitution energies at position 1 in the three parent MOFs. In no case does the inclusion of spin polarization change the sign of the substitution energy. The difference between the energies of spin and non-spin polarized systems (parent and substituted MOFs at position 1 and isolated ions) are given in Table 4-4. These energy differences can be related to the magnetic moments of MOFs and ions, which in turn can be explained by their orbital occupancies and unpaired electrons. The GGA-PBE (U-J=0) magnetic moments (parent metal, substituted ions and total) and orbital occupancies are given in Table 4.

The equal up-spin and down-spin channel orbital occupancies (0.78/0.78) of Zr 4*d* orbitals leads to zero magnetic moment and thus leads to no change in the energy of Zr-8 MOF with spin-polarization. Similarly, the zero orbital occupancies of both up-spin and down-spin channels in Zr^{4+} ion leads to zero magnetic moment which causes no change in the energy with spin-polarization.

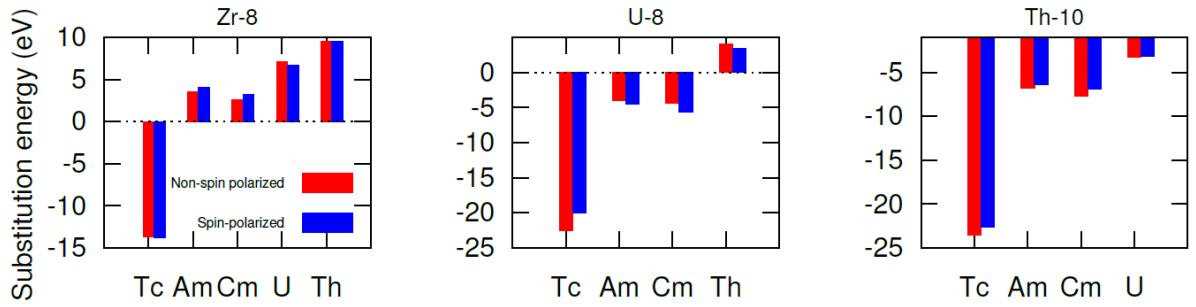

Figure 4-8. Effect of spin polarization on substitution energies at position 1 in Zr-8, U-8 and Th-10 MOFs, using GGA-PBE (*U*-*J*=0) XC-functional.

Tc substitution induces a net magnetic moment of 2.78 μ_B in the Zr-8 MOF, which originates from the 4*d* partial orbital magnetic moment of Tc (2.32 μ_B) as a result of its unequal up-spin and down-spin orbital occupancies (1.43/3.70). The energy of Tc substituted Zr-8 MOF thus decreases by 2.47 eV with spin-polarization. Similarly, unequal orbital occupancies of up-spin and down-spin channels (0/2.84) of 4*d* orbitals in Tc^{4+} ion results in a magnetic moment of 1.53 μ_B, decreasing its energy by 2.48 eV. The differences in the energies with and without spin essentially cancel out and the overall substitution energy is only 0.05 eV when calculated using spin polarization.

Similarly, the different up-spin and down-spin channel 5*f* orbital occupancies of Am, Cm, U, and Th gives rise to non-zero magnetic moments (except Th, which has equal occupancies and thus zero local magnetic moment), which in turn determine the magnitude of reduction in their energies. Am and Cm are the most magnetic moment inducing species, followed by Tc and then Th and Zr which does not result in magnetism at all. This analysis and those in the two previous subsections establish the robustness of the results for various levels of DFT. In future calculations, we thus use non-spin polarized GGA-PBE without any DFT+*U*.

4.3.6 Relativistic Effects: Spin-Orbit Coupling (SOC)

Spin-orbit interactions were investigated using the GGA-PBE XC-functional to determine the relativistic effects on the substitution energies. Fig. 4-9 shows the substitution energies (position 1) with and without SOC in Zr-8, U-8 and Th-10 MOFs.

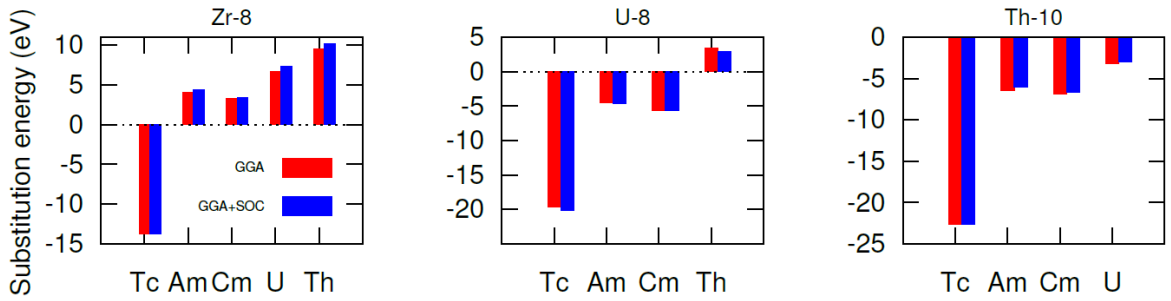

Figure 4-9. Effect of spin-orbit coupling on substitution energies at position 1 in Zr-8, U-8 and Th-10 MOFs, using GGA-PBE (*U*-*J*=0) XC-functional.

The inclusion of SOC changes the magnitude of substitution energies by of maximum of ±15%, however, the favorability of substitution remains the same. The absolute energies of the parent and substituted MOFs, and the reference ions do decrease with SOC, however the final differences to obtain the substitution energies do not change significantly due to cancellation of the effects for the reactants and products. Table 4-5 shows the difference between SOC and non-SOC absolute energies, $E_{absolute\ (SOC\ –\ non\text{-}SOC)}$, of parent and substituted MOFs (position 1), as well as those of isolated ions in vacuum. Final differences in substitution energies with and without SOC, $E_{substitution\ (SOC\ –\ non\text{-}SOC)}$, are also shown.

The magnitude of reduction of the energies of MOFs and reference ions depends on the atomic mass of the metal ions. Generally, heavier metals have the greatest contribution to the SOC energy. As can be seen from Table 4-5, systems containing Cm (247 amu) and Am (243 amu), the heaviest metal ions, show the most significant reduction in the energies in with the inclusion of SOC, followed by U (238 amu) and Th (232 amu). Zr (92 amu) and Tc (98 amu)

contributes the least to the SOC energy (Table 4-5). We thus conclude that the substitution energies do not substantially change when SOC interactions are included; hence, SOC will not be used in further analyses.

Table 4-5. GGA-PBE (*U*-*J*=0) calculated differences in absolute energies $E_{absolute}$ (SOC – non-SOC) with and without SOC of the parent and substituted MOFs (position 1), and isolated ions in vacuum. Differences in final substitution energies with and without SOC ($E_{substitution\ (SOC - non\text{-}SOC)}$) are also shown.

System	$E_{absolute\ (SOC - non\text{-}SOC)}$ (eV)	$E_{substitution\ (SOC - non\text{-}SOC)}$ (eV)
Zr-8	-0.40	-
Tc @pos1	-0.36	+0.04
Am @pos1	-4.24	+0.26
Cm @pos1	-4.42	+0.17
U @pos1	-2.63	+0.67
Th @pos1	-0.96	+0.62
U-8	-16.79	-
Tc @pos1	-14.44	-0.55
Am @pos1	-18.16	-0.17
Cm @pos1	-18.06	0.00
Th @pos1	-15.56	-0.50
Th-10	-8.00	-
Tc @pos1	-6.89	+0.01
Am @pos1	-10.57	+0.36
Cm @pos1	-10.79	+0.22
U @pos1	-9.65	+0.15
Zr^{4+}	-0.05	-
Tc^{4+}	-0.06	-
Am^{4+}	-4.16	-
Cm^{4+}	-4.34	-
U^{4+}	-2.96	-
Th^{4+}	-1.23	-

4.3.7 Reference States: Vacuum, Continuum Water Medium, and Hydrated Ions

In determining the free energy of substitution, an understanding of where the ion being substituted in come from and where the ion being substituted out goes to; we refer to these as the reference ions. To this point, it has been assumed that these are bare ions in vacuum, and all of the substitution energies discussed above in the technical studies of the appropriate DFT methods have made this assumption. However, the use of these bare ions isolated in vacuum results in the

abnormally high magnitude of substitution energies (calculated as per Eq. 4-2), which are of the order of 10-20 eV, as can be seen from Fig. 4-6 to Fig. 4-9. There are two components to Eq. 4-2: (1) difference in energy between substituted MOF and parent MOF ($E_{An(SBU)} - E_{SBU}$) and (2) difference in energy between parent ion and substituting ion ($E_{parent\ M}^{4+} - E_{substituting\ An}^{4+}$). As an illustration, these two components are shown and compared in Table 4-6 for the Zr-8 MOF. The high magnitude of the substitution energies originates from the energy differences of the reference ions rather than from energy differences in the substituted and parent MOFs itself. Thus, the use of the bare ions in vacuum as a reference state is unsatisfactory in both leading to physically unreasonable substitution energies and is not reflecting the aqueous environments in which these substitution reactions actually take place. Therefore, two additional types of reference states for solvation are considered: (1) a continuum water medium and (2) hydration of ions by an explicit number of water molecules (hydrated ions).

Table 4-6. Difference between (1) energies of substituted (position 1) and parent Zr-8 MOF (2) energies of Zr^{4+} and substituting ion (An^{4+}) calculated using non-spin polarized GGA-PBE level of theory without DFT+*U* corrections and without SOC.

Substituting ion (An)	$E_{An(SBU)} - E_{SBU}$ (eV)	$E_{parent\ Zr}^{4+} - E_{substituting\ An}^{4+}$ (eV)
Tc	6.69	-19.12
Am	-2.18	5.80
Cm	-2.46	5.10
U	-1.80	9.00
Th	-1.37	10.88

The substitution energies when the ions treated in continuum water medium and in vacuum are the same. This is because the energies of the ions increase by exactly the same amount when treated in a water medium, with reference to vacuum. The dielectric constant simply scales the energies of the ions without affecting their differences in energies. However, when the ions are explicitly surrounded by a discrete number of water molecules, the structures

and resulting energies for the various ions differ from each other, with correspondingly different hydration energies.

The binding energies, $E_{binding}$, of the ion-water complex $[M(H_2O)_n]^{4+}$ are calculated as described in Pavlov et al. [139] using

$$E_{binding} = E(M^{4+}) + nE(H_2O) - E\{M(H_2O)_n^{4+}\} \quad (4\text{-}3)$$

where, $E(M^{4+})$ is the energy of isolated 4+ ion, n is the number of water molecules surrounding the ion, $E(H_2O)$ is the energy of a single water molecule, and $E\{M(H_2O)_n^{4+}\}$ is the energy of the ion-water complex. We first reproduced the binding energy of $[Be(H_2O)]^{2+}$ complex using the same method in Pavlov et al. and achieved a value of 147.5 kcal/mol which is only 1% different from their values of 146.1 kcal/mol.

We started out with the calculation of binding energies of the ion-water complexes of interest in this work i.e. $[Zr(H_2O)_n]^{4+}$, $[Tc(H_2O)_n]^{4+}$, $[Am(H_2O)_n]^{4+}$, $[Cm(H_2O)_n]^{4+}$, $[U(H_2O)_n]^{4+}$, and $[Th(H_2O)_n]^{4+}$ in the Gaussian software package using the methods and basis sets described in section 4.2.2. We found that the order of binding energies of Am^{4+} and Cm^{4+} ions with water molecules are abnormally higher than those for Zr^{4+}, Tc^{4+}, U^{4+}, and Th^{4+}. To verify the accuracy of these calculations on elements that are not widely studied using quantum chemistry techniques, we also calculated the binding energies of Zr^{4+}, Tc^{4+}, U^{4+}, and Th^{4+} with water in VASP using GGA-PBE level of theory and compared them with Gaussian results to establish robustness. This binding energy comparison of VASP and Gaussian is shown in Fig. 4-10 for n=1 to n=10. All the water molecules are placed in the 1st shell around the ions for simplicity. Different configurations (different shells) of the water molecules around the ions are also explored below. The binding energies calculated in VASP and Gaussian are reasonably consistent with each other for all the ions. Thus, binding energies for Am^{4+} and Cm^{4+} are

calculated in VASP are used in subsequent analyses. However, since Gaussian calculated binding energies of Zr, Tc, U, and Th show a smoother variation with n than the corresponding VASP values, we will continue to use Gaussian to model the hydrated ions for these ions.

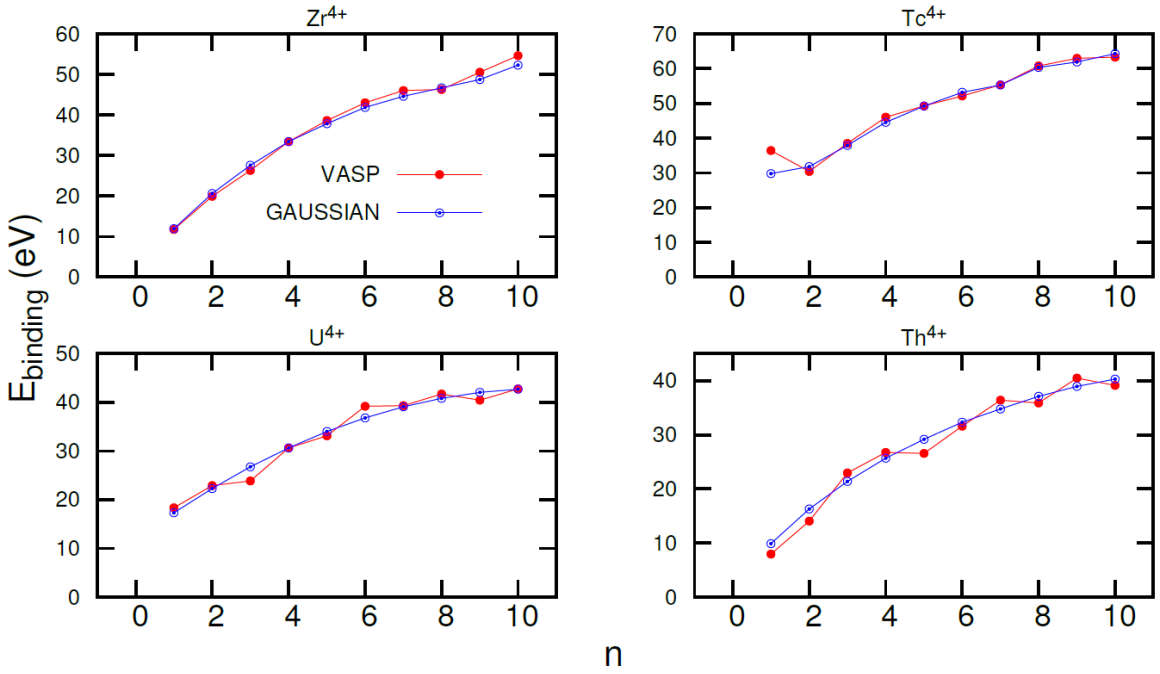

Figure 4-10. Binding energies ($E_{binding}$) of the $[M(H2O)_n]^{4+}$ complex for M=Zr, Tc, U, and Th and n=1 to n=10, calculated using VASP (GGA-PBE) and Gaussian09 (B3LYP/6-31G(d) (O,H)/LANL2DZ (Zr,Tc)/SARC (U, Th)) level of theories.

We further investigated different configurations of water molecules around the ions, rather than placing all of them in the 1st shell. We also considered up to *n*=20 with an anticipation of achieving converged substitution energies with the number of water molecules around the ion, as discussed below. The 1st, 2nd and 3rd nearest-neighbor (NN) shells of Zr^{4+}, U^{4+}, Th^{4+}, Am^{4+}, and Cm^{4+} were found to accommodate 8, 7 and 5 water molecules respectively, whereas the 1st, 2nd and 3rd NN shells of Tc^{4+} were found to accommodate 7, 7 and 6 water molecules respectively. Fig. 4-11(a) shows the binding energies of the $[M(H_2O)_n]^{4+}$ ion-water complexes for M=Zr, Tc, U, Th, Am and Cm and *n*=1 to 20. A geometry-optimized structure of

$[M(H_2O)_n]^{4+}$ for M=Zr and *n*=20 is shown in Fig. 4-11(b) for illustration. The binding energies increase continuously with increasing *n*, with small jumps in the energies as water molecules begin to fill the next shell. Fig. 4-11 also shows polynomial fits to the data. Each shell of water molecules is fitted independently, i.e. *n*=1 to 8, *n* =9 to 15 and *n*=16 to 20, for M= Zr, Tc, U, Th, Am, and Cm, are fitted using three different polynomial fits for each. Similarly, *n*=1 to 7, *n*=8 to 14 and *n* =15 to 20 for M=Tc are fitted independently.

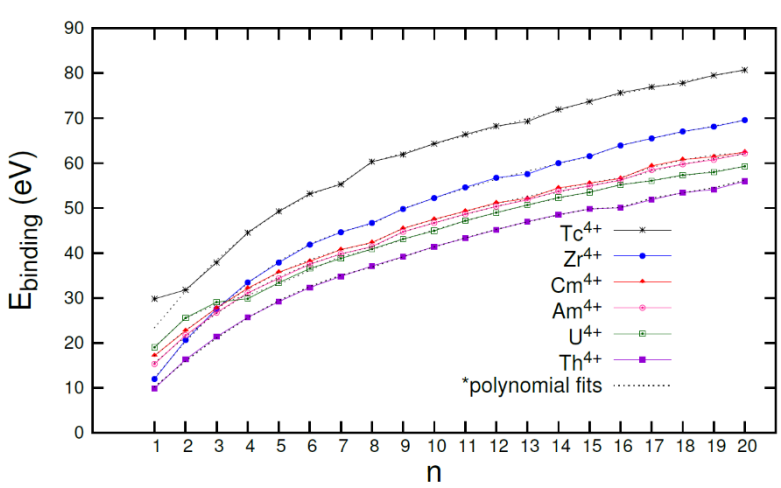

(a) Binding energies of ion-water complex

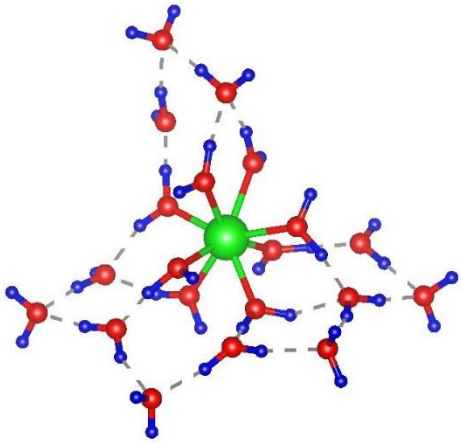

(b) Optimized structure of $[Zr(H_2O)_n]^{4+}$ for *n*=20

Figure 4-11. (a) Binding energies of the ion-water complex $[M(H_2O)_n]^{4+}$ for M=Zr, Tc, U, Th, Am and Cm and *n*=1 to 20, and their polynomial fits (different 1st nearest neighbor shells fitted independently). Binding energies for M=Zr, Tc, U, and Th calculated using Gaussian {B3LYP/6-31G(d)/LANL2DZ (Zr, Tc)/SARC(U, Th)} and for M=Am and Cm calculated using non-spin GGA-PBE without DFT+*U* or SOC. *Note that *n*=1 for M=Tc is excluded from the polynomial fit (b) Geometry-optimized structure of the $[Zr(H_2O)_n]^{4+}$ complex for *n*=20, where *n*=1 to 8 denotes the 1st coordination shell, *n*=9 to 15 denotes the 2nd coordination shell and *n*=16 to 20 denotes the 3rd coordination shell. The green, red, and blue spheres represent M, O, and H, respectively. The solid bonds denote M--O bonds in the 1st coordination shell and dashed bonds denote O--H Hydrogen bonds.

The absolute energies of the ion-water complex i.e. $E\{M(H_2O)_n^{4+}\}$ in Eq. 4-3 are then backed out and used in Eq. 4-2 to determine the substitution energies with hydrated ions as reference. Eq. 4-2 can then be formatted and written as,

$$E_{substitution} = \left(E_{(An)SBU} - E_{SBU}\right) + [N \times \ (E\{M(H_2O)_n^{4+}\} - E\{An(H_2O)_n^{4+}\})] \qquad (4\text{-}4)$$

where, $E\{M(H_2O)_n^{4+}\}$ is the energy of parent hydrated metal ion and $E\{An(H_2O)_n^{4+}\}$ is the energy of substituted hydrated metal ion, with equal *n* number of water molecules.

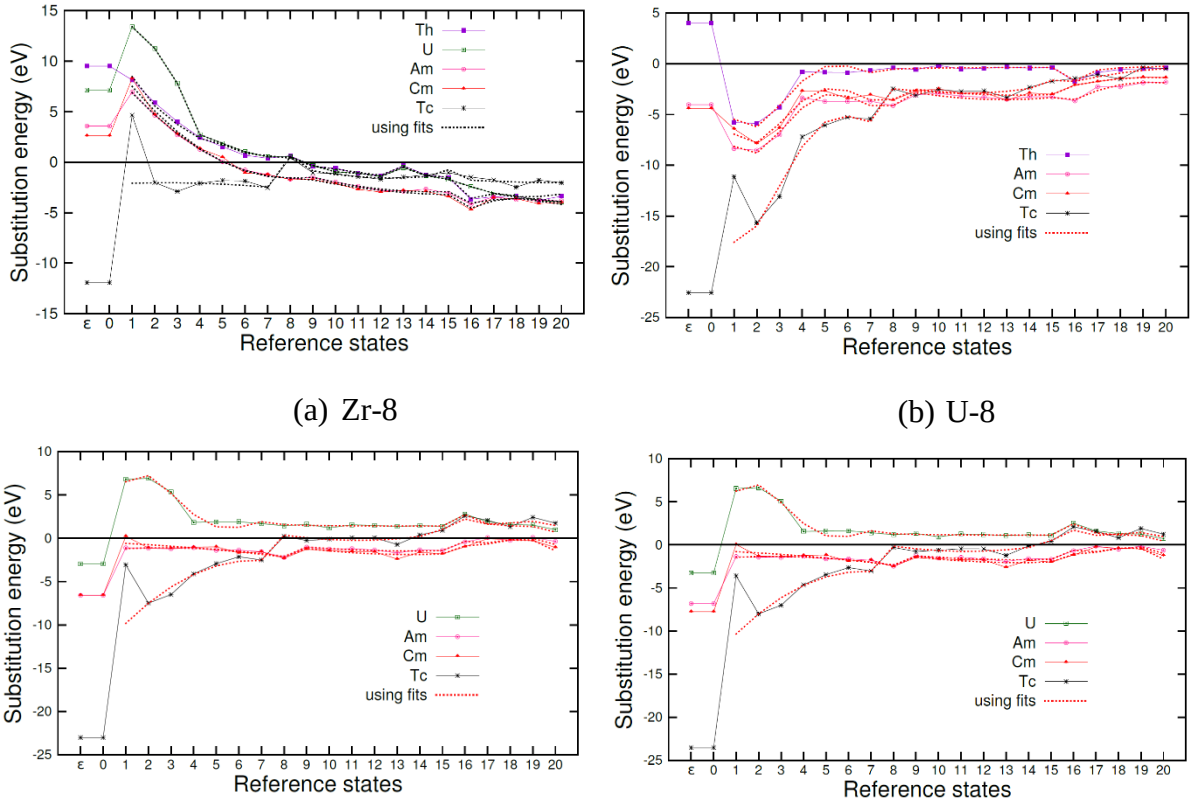

(a) Zr-8 (b) U-8

(c) Th-8 (d) Th-10

Figure 4-12. Substitution energies (position 1) of Tc, U, Th, Am and Cm in (a) Zr-8 (b) U-8 (c) Th-8 and (d) Th-10 MOFs, for various reference states: ions in continuum water medium (ε), ions in vacuum (n=0) and hydrated ions with explicit number of water molecules around them (*n*=1 to *n*=20), using raw and fitted hydration energies.

Fig. 4-12 shows substitution energies at position 1 in Zr-8, U-8, Th-8 and Th-10 MOFs for different reference states of ions, namely, ions treated in a continuum water medium (ε), ions in vacuum (*n*=0), and hydrated ions with *n*=1 to *n*=20. The magnitude of substitution energies is reduced significantly (<5 eV in Zr-8 and <3 eV in U and Th MOFs) when the hydration effects are treated explicitly. The magnitude of the substitution energies converges in each individual

shell of water molecules around the ions, and it shows a small jump as the number of water molecules crosses a shell. The substitution energies typically remain the same after the 1st shells in each MOF. Thus, it can also be concluded that a discrete number of water molecules until the 1st shell can sufficiently determine the preference of substitution in a MOF.

Table 4-7. Comparison of difference between the absolute energies of reference ions in Eq. 4-4, for *n*=0 and *n*=20 cases.

M	$E\{M(H_2O)_n^{4+}\} - E\{An(H_2O)_n^{4+}\}$ (eV)									
	An= Tc^{4+}		An= Am^{4+}		An= Cm^{4+}		An= U^{4+}		An= Th^{4+}	
	n=0	*n*=20	*n*=0	*n*=20	*n*=0	*n*=20	*n*=0	*n*=20	*n*=0	*n*=20
Zr	-19.12	-9.22	5.80	-1.64	5.10	-1.52	9.00	-1.31	10.88	-2.70
U	-28.71	-7.91	-2.56	-0.33	-3.25	-0.21	-	-	2.57	-1.85
Th	-31.28	-6.51	-5.13	1.06	-5.82	0.68	-2.57	1.39	-	-

There is a transition from favorable to unfavorable substitution or vice-versa when the ions are hydrated, in some cases. For example, in Zr-8 MOF, hydration of ions makes the substitution of Am, Cm, Th, and U thermodynamically favorable (*n*=20) (where without hydration it was unfavorable), while Tc substitution remains favorable (Fig. 4-12(a)). These transitions can be attributed to the stabilization of 4+ ions when surrounded by water molecules, which leads to a significant reduction in the magnitudes of the differences in energies of the ions in vacuum and when hydrated as shown in Table 4-7 (*n*= 0 vs. *n*=20). When going from *n*=0 to *n*=20, the energy differences between the parent Zr^{4+} ion of Zr-8 and substituting species changes from positive to negative for Am^{4+}, Cm^{4+}, U^{4+} and Th^{4+} and significantly reducing the magnitude in each case. The energy difference with Tc^{4+} remains negative, however the magnitude of the substitution energy is reduced the most. In the U-8 MOF, the substitution of Tc, Am, and Cm is exothermic even without hydrated ions (Fig. 4-12(b)), however, the magnitude of substitution energies is reduced significantly because of the reduced magnitude of energy differences between the parent U^{4+} ion and substituting ions (Table 4-7). There is a transition from the unfavorable substitution of Th to favorable substitution in the U-8 MOF in going from

n=0 to *n*=20, because of a sign reversal (positive to negative) in the energy difference between U^{4+} and Th^{4+} (Table 4-7). The same sign reversal in the energy difference between Th^{4+} and U^{4+} in going from *n*=0 to *n*=20, have the opposite effect on the U substitution in the two Th-MOFs, where there is a transition from favorable to unfavorable reaction. Although the energy differences between Th^{4+} and Am^{4+}/Cm^{4+} changes from negative to positive with hydration of ions (Table 4-7), their favorable substitution with ions in vacuum remains favorable even after hydration of ions, as the energy differences between substituted and parent Th-MOFs are negative enough to maintain the negative substitution energy. Tc substitution is favorable with ions in vacuum, whereas turns unfavorable for *n*>14, where *n*=15 marks the end of 2nd shell of water molecules. This transition is a result of a significant increase in the energy difference between Th^{4+} and Tc^{4+} ions in going from *n*=0 to *n*=20.

Fig. 4-13 summarizes all of our key results together. The substitution energies are calculated when a substitution occurs at position 1, position 3 or on all six positions of the metallic species, using hydrated ions (*n*=20) as the reference. Tc, Am, and Cm substitution are energetically favorable in all the four MOFs. U substitution is favorable only in Zr-8 MOF, while unfavorable in the Th MOFs, and Th substitution is favorable in both Zr-8 and U-8 MOFs. While favorable Th substitution in U-8 MOF and unfavorable U substitution in Th-8 MOF is consistent with transmetalation reactions performed by Shustova and group [103,110] favorable U and Th substitutions in Zr-8 MOF were found to be experimentally unfeasible [103]. However, Th and U substitutions in Zr-8 MOF are favorable only for *n*>8 and remain unfavorable until *n*=8 (Fig. 4-12(a)). Whereas, Th substitution in U-8 MOF (Fig. 4-12(b)) and U substitution in Th MOFs (Fig. 4-12(c) and Fig. 4-12(d)) is unfavorable and favorable respectively only for *n*=0 (or continuum

water medium) cases. They turn favorable and unfavorable respectively, immediately after being hydrated with explicit water molecules (from *n*=1 to *n*=20).

We also investigated the substitution of Re in Zr-8 and compared it to the Tc case, as Re is popularly used as a surrogate for Tc in experiments [104]. The substitution energy of Re in Zr-8 (position 1) with hydrated reference ions (*n*=20) was found to be -1.02 eV, in comparison to -2.10 eV for Tc. Thus, Tc shows favorable substitution consistent with its surrogate Re.

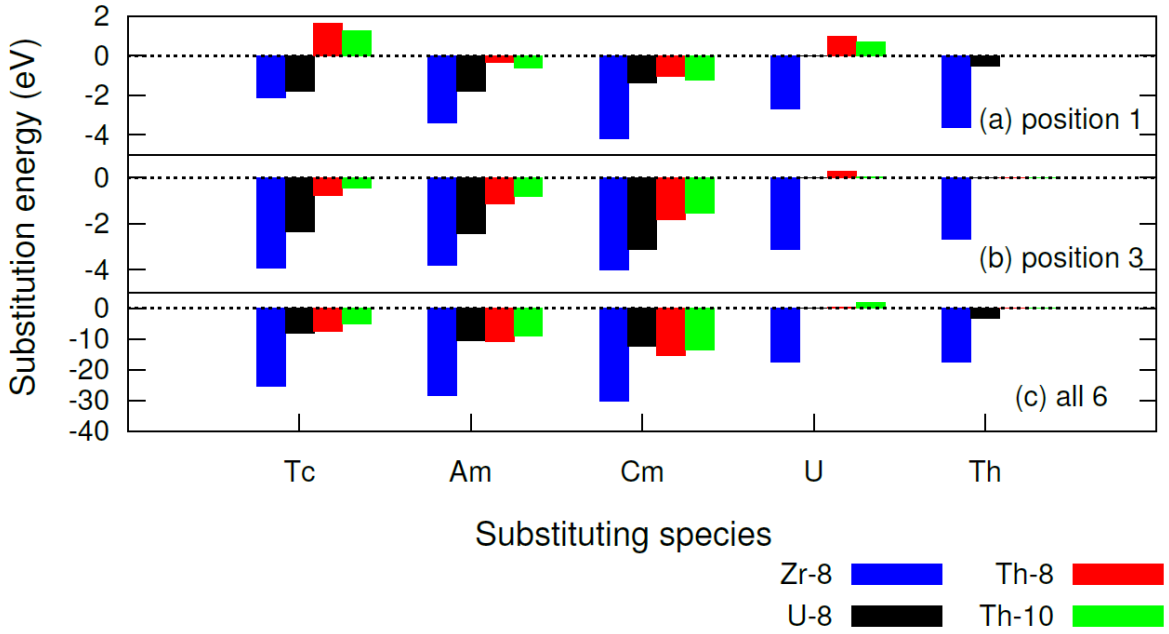

Figure 4-13. Non-spin polarized GGA-PBE (without DFT+*U*, SOC, vdW) substitution energies of substitution for Tc, Am, Cm, U, Th in four different parent MOFs at (a) position 1 (b) position 3 and (c) all six positions, calculated using hydrated ions (*n*=20) as reference.

We revisit the effects of various DFT methods on the substitution energies (position 1) with the correct reference state, i.e., hydrated water molecules (*n*=20). The error bar for the effects of XC-functionals on the substitution energies with ions in vacuum was less than 0.05 eV, as discussed previously in Section 4.3.3 and Fig. 4-6. Thus, XC-functionals need not be investigated further and we can still consider GGA-PBE functional to be robust for favorability

of substitution. The error bar for DFT+*U* and spin-polarization effects was up to the order of ~2 eV (Fig. 4-7 and Fig. 4-8) and thus we recalculate the substitution energies with these effects for *n*=20 water molecules. Table 4-8 shows the effect of DFT+*U* on the substitution energies at position 1 in Zr-8 MOF for *n*=20 water molecules. It can be seen that the DFT+*U* corrections does change the magnitude of substitution energies, with the magnitude for Tc substitution changing the most. However, in no case does the DFT+*U* corrections changes the sign of substitution energy, and thus the favorability of substitution is unaffected. Following this, we only investigate the spin-effects for Tc for its highest error bar among all the ions. We find that spin-polarization changes the substitution energy of Tc from -2.12 eV to -1.64 eV; however since the sign remains the same, the favorability of substitution remains unaffected. In conclusion, GGA-PBE XC functional without any sophisticated DFT methods is sufficient to establish the favorability of substitution even with hydrated water molecules as a reference state.

Table 4-8. Effect of DFT+*U* on the substitution energies at position 1 in Zr-8 MOF, calculated using hydrated (*n*=20) water molecules and GGA-PBE XC-functional

Substituting ion	Substitution energy (eV)	
	GGA-PBE	GGA+*U*
Tc	-2.12	-0.88
U	-2.70	-2.50
Am	-3.40	-3.87
Th	-3.65	-3.32

We would expect the substitution energies for all six positions to be the weighted sum of substitution energies at position 1 and position 3, i.e. ideally, $E_6 = (2 \times E_1) + (4 \times E_3)$. However, as can be seen in Fig. 4-13, the real substitution energies for all six positions are different from the ideal energies. Fig. 4-14 shows the magnitude of the difference between real and ideal substitution energies ($|\Delta E_{real\text{-}ideal}|$) for all 6 positions. Tc shows the maximum deviation from ideal energies in most of the cases, Am and Cm shows deviations of the same order, while

Th and U shows the least deviations. These deviations can be attributed to the relaxation of strain when all the metal atoms are the same in a MOF.

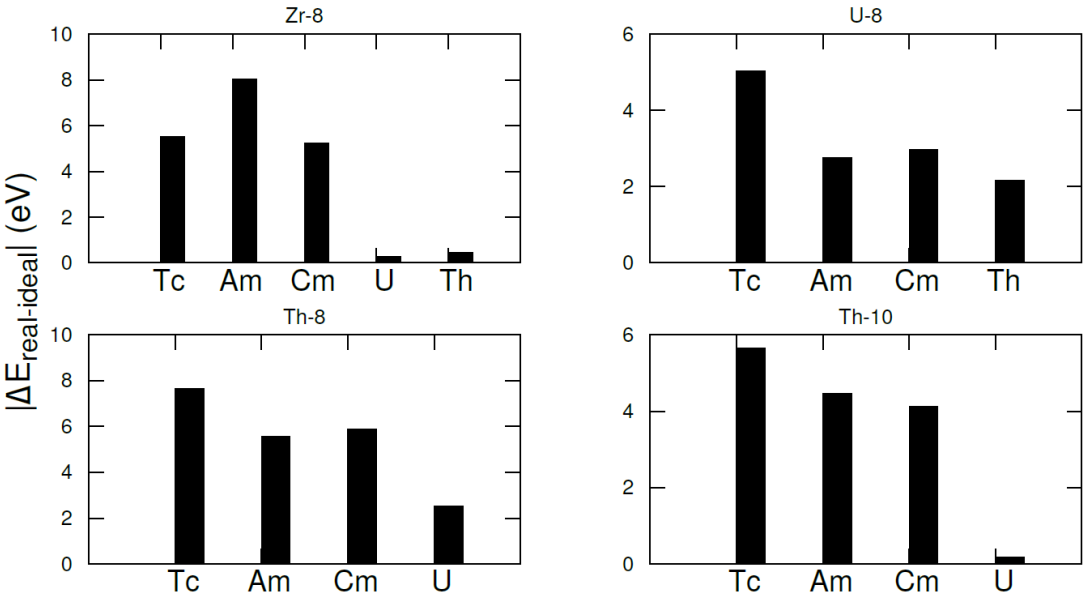

Figure 4-14. Non-spin polarized GGA-PBE (without DFT+*U*, SOC, vdW) calculated magnitude of differences between real and ideal substitution energies for all six positions in all the MOFs.

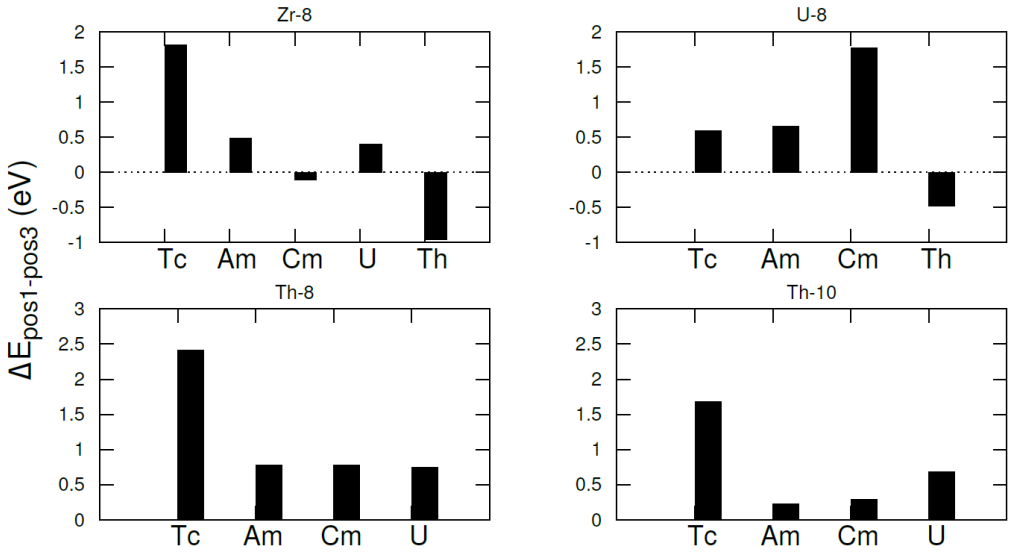

Figure 4-15. Non-spin polarized GGA-PBE (without DFT+*U*, SOC, vdW) calculated difference between substitution energies at position 1 and position 3.

Moreover, the substitution energies at position 3 are lower than those at position 1 for all the radionuclides except Th, as can be seen in Fig. 4-15 which shows the difference between substitution energies at position 1 and position 3 ($\Delta E_{pos1\text{-}pos3}$). The different local environment at position 1 (metal-to-oxygen coordination= 8 in both M-8 and M-10 MOFs) than position 3 (metal-to-oxygen coordination= 6 in M-8 and 7 in M-10) could be a possible reason for these energy differences, as the substitution energy difference between position 1 an position 3 is related to the preferred oxygen coordination of the substituting metals.

4.4 Conclusions

A detailed characterization of the thermodynamic favorability of substitution of radionuclides like Tc, Am, Cm, U, and Th in four different parent MOFs (Zr-8, U-8, Th-8, and Th-10) was carried out using DFT calculations. Substitution energies at the metal nodes were calculated to determine the thermodynamic favorability of substitution. Various DFT methods were used to establish robustness in results. The ion-exchange favorability was found to be robust with several XC-functionals (GGA→metaGGA→hybrids), vdW corrections, DFT+*U* corrections, spin-polarization and spin-orbit coupling. Different reference states of the exchanged ions namely, vacuum, continuum water medium, and explicit water molecules were explored. It was found that the choice of an appropriate reference state for the source and sink of the ions substituted in and out is critical. Thus, in conclusion, GGA-PBE level of theory without any additional factors (DFT+*U* corrections, spin-polarization, SOC, and vdW corrections) is sufficient to establish the preference of ion-exchange at the metal node in MOFs. Although these factors are important for accurate calculations of the bandstructure [110] they do not significantly affect either the substitution energies or the favorability of substitution. Moreover,

the truncated SBUs are adequate models to determine the ion-exchange favorability at the metal nodes of the full MOFs.

This work computationally characterized the thermodynamics driving the transmetalation process for the synthesis of actinide based MOFs carried out by Dolgopolova et al. [103], who prepared the first examples of actinide-bimetallic MOFs. Favorable Th substitution in U-8 MOF and unfavorable U substitution in Th MOFs is consistent with experiments. The prediction of favorable Th and U substitutions in Zr-8 MOF for hydrated ions (n>8) is not consistent with experiment. Although *N,N'-dimethylformamide* (DMF) is a common organic solvent used to synthesize these MOFs [103,140], our calculations indicate that the use of water as a solvent may also be possible. More complicated solvents, such as DMF, can be explored in future computational studies using this work as a benchmark. The cation-exchange method explored in this work could offer an alternative to some common techniques for radionuclide extraction such as Plutonium Uranium Redox EXtraction (PUREX), anion-exchange resins, and solvent-extraction based processes, which suffer from the drawbacks of the use of volatile and toxic organic diluents, generation of large amount of secondary waste, high radiation doses, low sorption capacity and slow kinetics [140].

CHAPTER 5
ELECTRONIC STRUCTURE DESCRIPTION OF METAL-ORGANIC FRAMEWORKS (MOFs)

5.1 Background

While the fundamental thermodynamic properties, such as substitution energies drive the sequestration of radionuclides in a material system, the electronic properties are equally critical to understand the role of chemical bonding. The non-actinide-based MOFs have been widely studied for their thermodynamic and electronic properties [111,141–145], however, a detailed understanding of the actinide-containing frameworks is lacking.

In this chapter, we investigate the electronic structures and magnetic properties of Zr-, Th-, and U-based MOFs, using density functional theory (DFT) calculations. These MOFs were investigated for their thermodynamics of cation exchange in Chapter 4. We systematically explore various DFT methods including (1) DFT+*U* to account for electron localization (2) spin-polarization to study magnetism (3) spin-orbit coupling (SOC) to account for relativistic effects, and (4) exchange-correlation (XC) functionals at different levels, to understand the role of *d*-, and *f*-electrons in determining the band gaps of MOFs studied. In particular, we study the case of U-MOF in detail, as it shows a number of magnetic configurations. Moreover, we identify the origin of band gap in a MOF (inorganic or organic groups), by modeling different truncated models of the extended MOF. We also compare our calculations to the experimental results, wherever available.

5.2 Structures and Computational Methods

5.2.1 MOF Structures

A unit cell of the MOF considered in most detail in this work is shown in Fig. 5-1(a). The MOFs consists of metal-containing nodes connected via ligands to organic inkers to form a

three-dimensional network by organic linkers. The metal nodes refer to the metal sites (Zr, Th, and U in this work) and their surrounding oxygen atoms. The ligands are organic groups connected to the metal sites and are –(COO)– units in this work. The metal-nodes and ligands together constitute repeating units in the three-dimensional periodic extended structure and are referred to as secondary building units (SBUs); one SBU is circled in Fig. 5-1(a). The linkers (Fig. 5-1(b)) are another type of organic groups, in this case Me_2BPDC^{2-} (2,2′-dimethylbiphenyl-4,4′-dicarboxylate). These MOFs have been explored experimentally by Dolgopolova et al. [103] and Ejegbavwo et al. [110]. The thermodynamics of ion exchange of radionuclides in these materials has been characterized computationally in Chapter 4 (Pandey et al. [146]), which provides a more detailed description of their structures.

The large system size of the extended MOF structures (~300 atoms) makes the DFT calculations extremely computationally intensive. For this reason, the truncated SBUs are modeled; this is a well-established method [125–127]. The SBUs can be categorized as M-8 and M-10, depending on the number of formic acid ligands they contain. The metal nodes of the M-8 SBU are connected to eight –(COO)– groups and those of M-10 SBU are connected to ten such groups.

One formula unit (f.u.) cluster representations of the M-8 $[M_6(COOH)_8O_8]$ and M-10 SBUs $[M_6(COOH)_{10}(OH)_2O_6]$ are shown in Fig. 5-2(a) and Fig. 5-2(b). The two axial metal atoms (labeled 1 and 2 in Fig. 5-2) in both M-8 and M-10 SBUs are coordinated to eight oxygen atoms each and thus are identical. The four equatorial metal atoms (labeled 3,4,5,6 in Fig. 5-2) in the M-8 SBU are coordinated to six oxygen atoms, while they are coordinated to seven oxygen atoms in the M-10 SBU; thus all equatorial atoms within a structure sites are identical to each other. Thus, four MOF-SBUs: Zr-8, U-8, Th-8 and Th-10 will be discussed in the present studies.

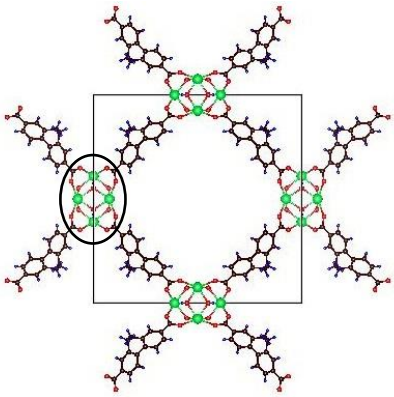

(a) Unit cell of MOF

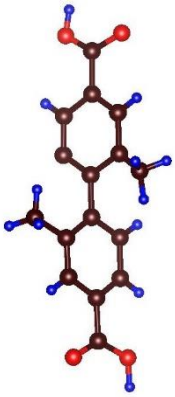

(b) Me_2BPDC^{2-} linker

Figure 5-1. (a) Unit cell of the extended MOF structure. The M-8 SBU, shown in more detail in Fig. 5-2, is circled in the unit cell. The black box denotes the edges of the unit cell. (b) Me_2BPDC^{2-} linker connecting the two SBUs in the unit cell. The green, red, black, and blue spheres represent the metal, oxygen, carbon and hydrogen atoms, respectively.

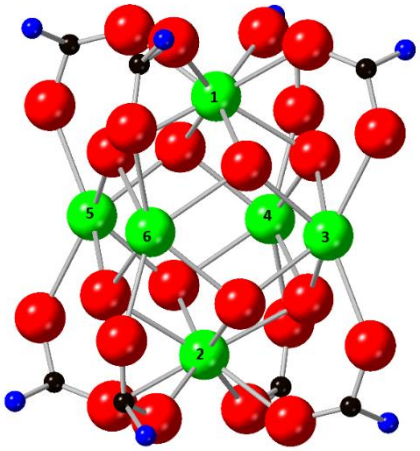

(a) M-8 SBU

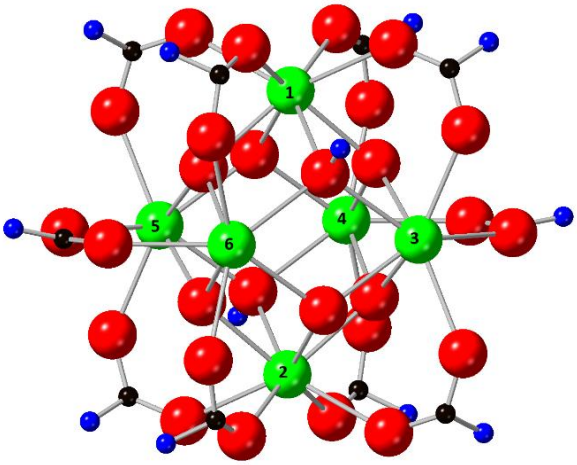

(b) M-10 SBU

Figure 5-2. Truncated models (SBUs) of the extended MOF: (a) M-8 (b) M-10. The green, red, black, and blue spheres represent M, O, C, and H, respectively. The metal atoms located in 1 and 2 positions have the same coordination environments as each other; the metal atom positions in 3, 4, 5, and 6 all have the same coordination environment.

All the SBUs considered are charged neutral and for simplicity and can be viewed as a combination of M^{4+} metal ions, units of –(COO)– formic acid, hydroxyl $(OH)^-$ functional groups, and O^{2-}. Indeed, the neutral M-8 SBU is a combination of 6 M^{4+} (charge = +24), 8 –

(COO)– units (charge= –8) and 8 O^{2-} anions (charge = –16). Similarly, the neutral M-10 MOF SBU is a combination of 6 M^{4+} metal ions (charge= +24), 10 –(COO)– units (charge = –10), 2 –$(OH)^{-}$ units (charge= –2), and 6 O^{2-} anions (charge= –12).

5.2.2 Density Functional Theory

The DFT calculations were performed using the Vienna *ab initio* simulation package (VASP) [82,83] with plane-wave basis sets, employing the Projector-augmented wave (PAW) [68,84] pseudopotentials. We have considered the following explicit electrons for each atomic species: Zr ($4s^2 5s^2 4p^6 4d^2$), U ($6s^2 7s^2 6p^6 6d^1 5f^3$), Th ($6s^2 7s^2 6p^6 6d^1 5f^1$), C ($2s^2 2p^2$), O ($2s^2 2p^4$) and H ($1s^1$), with the potentials taken from potpaw_PBE.54 library of VASP. The MOF clusters were treated as non-periodic and were equilibrated in a cubic box 30 Å on a side; this results in large vacuum regions around the SBU. The plane-wave energy cutoff was set to 520 eV and all calculations were performed at the Γ-point only. Structural optimization was performed until the forces on each ion were less than 25 meV/Å, using 0.0001 eV as the energy tolerance for each electronic step. Gaussian smearing with a width of 0.05 eV was applied to all optimizations. A conjugate-gradient algorithm [91,92] was used to relax all the ions. Both non spin-polarized and spin-polarized calculations were performed to determine the effect of spin on the electronic structure of the MOFs. Relativistic effects were investigated using spin-orbit coupling interactions [69]. Various levels of exchange-correlation functionals including GGA-PBE [41], the SCAN [55] variety of meta-GGA, and the B3LYP [60] and HSE [147] hybrid functionals were used to evaluate the robustness in electronic density of states (DOS) of the MOFs. The van der Waals interactions (vdW) were considered using the dispersion correction formula in the PBE-D3, B3LYP-D3, etc. functionals by Grimme et al. [116] with Becke-Johnson damping [117], and the rVV10 [118] vdW formalism for the SCAN functional. Additionally, DFT+*U*

corrections were also analyzed using the Dudarev et al. [64] formalism in order to better describe the strong correlation of *d* and *f* electrons. Atomic charges were determined using the Bader charge analysis code [119–122].

Electronic structure calculations were also performed with the Gaussian-type orbitals using the Gaussian09 [128] software package, in order to establish robustness in the methods for the molecules considered. B3LYP and HSE levels of DFT methods were used in conjunction with the 6-31G(d) basis sets [148–150] for the O, C, H atoms and Stuttgart/Dresden (SDD) Effective Core Potentials (ECPs) [151–153] for the metal atoms. This relativistic pseudopotential, uses 28 electrons as the core electrons and 12 as the valence electrons for Zr, 60 core electrons and 30 valence electrons for Th, and 60 core electrons and 32 valence electrons for U.

5.3 Results and Discussions

5.3.1 Structural Analysis

The structural optimization is discussed in detail in Chapter 4. The GGA-PBE optimized average M-O bond lengths in the MOFs were found to be Zr-O < U-O < Th-O, at both position 1 and position 3, which is expected because of the increasing atomic sizes in going from Zr to Th. Moreover, the M-O bond lengths for 8-fold metal sites (position 1) was found to be longer than for 6-fold metal sites (position 3) in all the MOFs, which is also an expected outcome of the different coordination environments of the metal sites.

The following sections focuses on the electronic structure of these MOFs. Specifically, we examine the effects of (1) electron localization using DFT+*U* corrections on the *d*- and *f*-electrons, (2) magnetic effects, (3) relativistic effects using spin-orbit coupling (SOC), (4) effects of the choice of exchange/correlation functional, and (5) analysis of “SBU+linker” models to

determine the origin of highest-occupied molecular orbital (HOMO) – lowest-unoccupied molecular orbital (LUMO) gap in MOFs. For simplicity, the HOMO-LUMO gap will be referred to as the band gap.

5.3.2 Effect of Electron Localization

The DFT+*U* corrections were employed to investigate the effects of electron localization on the band gaps of the Zr-, U-, and Th-MOFs. The non-spin polarized GGA-PBE calculated band gaps, with and without DFT+*U* corrections, are shown in Fig. 5-3. An on-site Coulomb interaction was added to the zirconium *d*-, and, uranium and thorium *f*-electrons. Based on previous studies [63,130,135–137], a *U*-*J* =4.0 eV for Zr and U, and *U*-*J*= 6.0 eV for Th was used.

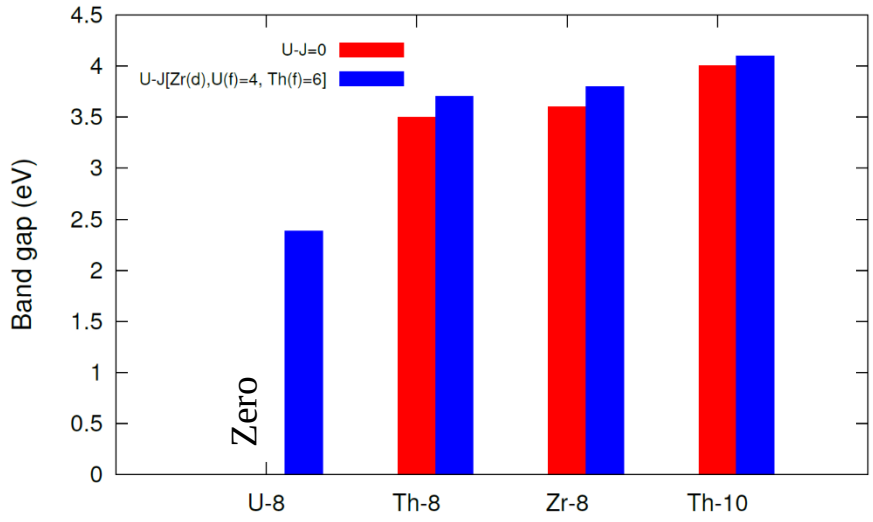

Figure 5-3. Non-spin polarized GGA+*U* calculated band gaps of the Zr-, U-, and Th-MOFs, with *U*-*J*= 0 (red), and *U*-*J*= 4 eV, 4 eV, and 6 eV respectively for Zr(4*d*), U(5*f*) and Th(5*f*) electrons (blue).

As can be seen from Fig. 5-3, the U-MOF has zero band gap and behaves as a metal with *U*-*J*=0 eV; the band gap increases to 2.38 eV with a *U*-*J*= 4.0 eV. A non-zero band gap of 3.50 eV is obtained for the Zr-8 and Th-8 MOFs even without a +*U* correction, which only increases

slightly to 3.7 eV with a $+U$ correction. The Zr-4*d* and Th-5*f* orbitals to which *U*-*J* is applied are unoccupied and already localized, and thus are only marginally affected by DFT+*U* corrections.

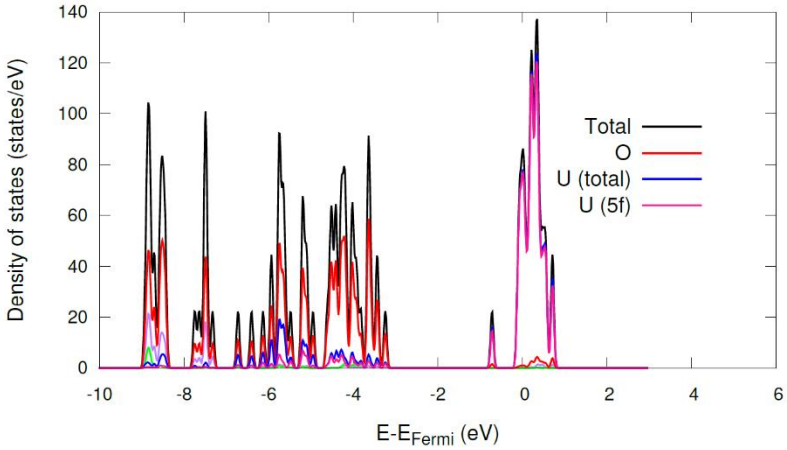

(a) *U*-*J*=0

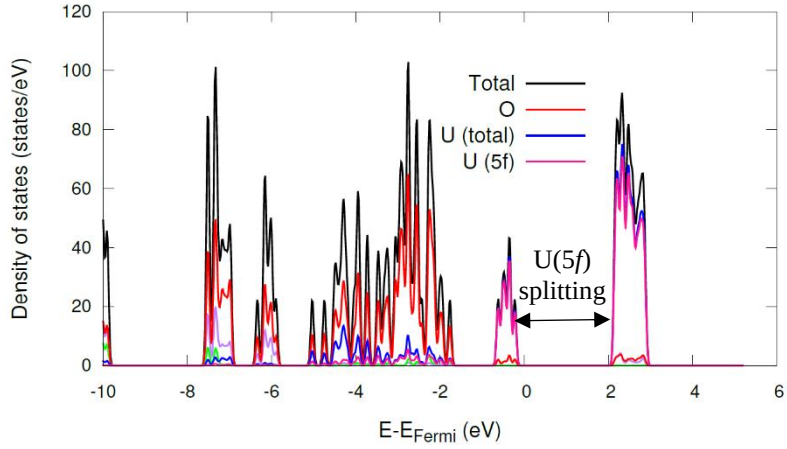

(b) *U*-*J*=4

Figure 5-4. Non-spin polarized GGA-PBE projected-DOS of the U-8 MOF with (a) *U*-*J*=0 and (b) *U*-*J*=4 eV. p-DOS of C (purple) and H (green) atoms are omitted in the legends for simplicity, as they are embedded deep in the bands.

The band gap of the U-MOF can be analyzed in terms of the projected-DOS (p-DOS), as shown in Fig. 5-4. *U*-*J*=0 leads to partial occupancies, because of self-interaction of highly delocalized uranium *5f*-electrons, which in turn gives rise to states at the Fermi level (Fig. 5-4(a)). Thus, the U-MOF behaves as a metal (zero-band gap) without any self-interaction

correction. This is very similar to the case of uranium oxides [136]; specifically for *U-J=0*, UO_2 is incorrectly predicted to be a metal.

The DFT+*U* corrections pushes the highest-occupied molecular orbitals (HOMO) and lowest-unoccupied molecular orbitals (LUMO) away from each other, resulting in a non-zero band gap (depending on the *U-J* value), 2.38 eV in this case. A non-zero *U-J* removes degeneracy of the 5*f* orbitals, thus splitting them into two energy regions, below and above the Fermi level. The uranium 5*f*-electrons dominate the band edges, regardless of the *U-J* value used, which indicates that the band gap is determined by the uranium metal.

The Th-10 MOF has a 0.50 eV greater band gap (4.0 eV) than its 8-coordinated counterpart (Th-8), which is presumably the result of the different local environment of the Th-sites at position 3 (and 4, 5, 6). The Th atoms at positions 3, 4, 5 and 6 are bonded to 6 oxygen atoms in the Th-8 MOF, in contrast to 7 oxygen atoms in the Th-10 MOF. The effect of coordination is further confirmed by the Bader charges, which increase in magnitude with higher-fold coordination. The Th-atoms at position 1 (8-fold) in both Th-8 and Th-10 MOFs have a Bader charge of +2.78, while have a charge of +2.66 at position 3 in Th-8 (6-fold) and +2.74 in Th-10 (7-fold) MOF. The Bader charges with and without +*U* corrections are given in Table 5-1. Application of DFT+*U* increases the Bader charges and thus decreases the covalency of the metal-oxygen bond.

Table 5-1. Bader charges of the metal-atoms in Zr-, Th-, and U-8, and Th-10 MOF SBUs, with and without DFT+*U* corrections

MOF	Charge State (Bader analysis)			
	U-J=0 eV		*U-J*=4.0 eV	
	position 1	position 3	position 1	position 3
Zr-8	+2.62	+2.53	+2.78	+2.68
U-8	+2.55	+2.44	+2.67	+2.55
Th-8	+2.78	+2.66	+2.90	+2.78
Th-10	+2.78	+2.74	+2.88	+2.84

Thus, DFT+*U* corrections are required to produce accurate electronic structure of the U-MOF, whereas are not necessary for the Zr-, and Th-MOFs. A *U-J*=4.0 eV will be used from now onwards for the U-MOF, and *U-J*=0 eV will be used for the Zr-, and Th-MOFs.

5.3.3 Magnetic Effects

The thorium and zirconium oxides (ThO_2 and ZrO_2) are known to be insensitive to spin and to be non-magnetic [137,154]. By contrast, the uranium oxide (UO_2) is known to be an anti-ferromagnet with a non-zero local magnetic moment (~2 μB) of uranium atoms [136,155]. With this in mind, we also investigate magnetism in the Zr-, Th-, and U-MOFs in this work using collinear spin-polarization. First, the default ferromagnetic (FM) configuration is used to probe the band gaps.

Table 5-2. GGA-PBE [*U-J* (Th, Zr) =0, (U)=4.0 eV] calculated majority-spin and minority-spin (↑/↓) orbital occupancies [Zr(d), Th(f) and U(f)], and magnetic moments per formula unit (f.u.) of the MOF-SBU and local moments per metal-atom in the SBU

MOF	Orbital occupancy (↑/↓)		Magnetic moment (μ_B)	
	position 1	position 3	total per f.u.	local moment per metal-atom
Zr-8	0.66/0.66	0.78/0.78	0.00	0.00
U-8	0.23/2.26	0.24/2.36	12.18	2.03
Th-8	0.26/0.26	0.31/0.31	0.00	0.00
Th-10	0.26/0.26	0.28/0.28	0.00	0.00

We find that, spin-polarization dramatically increases the band gap of U-MOF from 2.38 eV to 2.70 eV while, as we expect, not affecting the non-spin polarized band gaps of Zr-8, Th-8 and Th-10 MOFs (3.5, 3.5 and 4.0 eV respectively) at all. The origin of band gap in the U-MOF can be explained by unequal up-channel and down-channel orbital occupancies of the 5*f*-electrons.

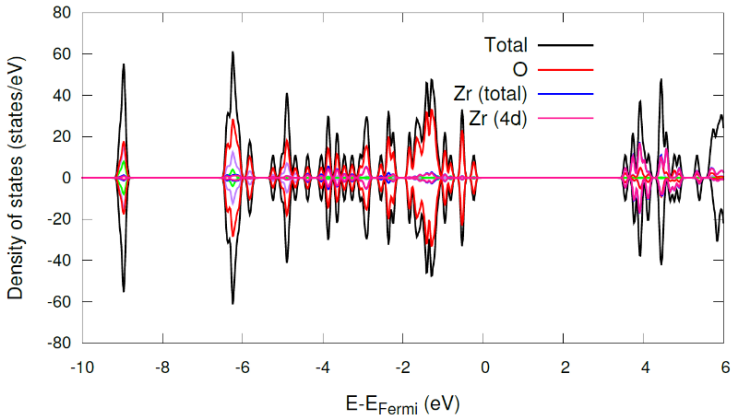

(a) Zr-8 MOF

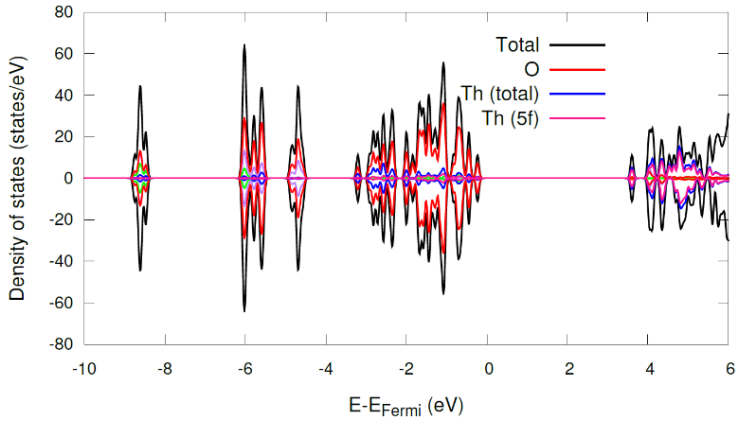

(b) Th-8 MOF

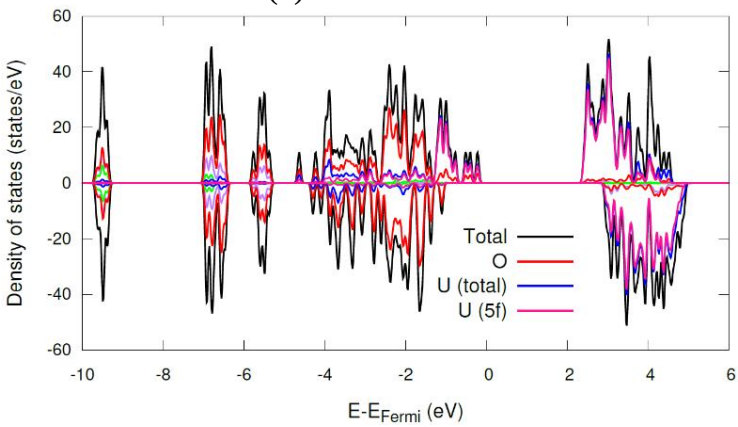

(c) U-8 MOF

Figure 5-5. Spin-polarized GGA+*U* [*U*-*J*=0, 0, and 4.0 eV for Zr, Th, and U respectively] calculated total-, and projected-DOS of the (a) Zr-8 (b) Th-8 and (c) U-8 MOFs. p-DOS of C (purple) and H (green) atoms are omitted in the legends for simplicity, as they are embedded deep in the bands

The orbital occupancies and magnetic moments are given in Table 5-2. The unequal majority-spin and minority-spin orbital occupation numbers for uranium atoms (at both position 1 and 3) gives rise to a local magnetic moment of 2.03 μB, and thus a net magnetic moment of 12.18 μB per formula unit of the SBU. By contrast, the Th and Zr atoms have equal up-, and down-channel orbital occupancies, which leads to a zero local magnetic moment of the metal atoms and thus a zero net magnetic moment of the SBU.

The total-, and p-DOS of the Zr-, Th-, and U-MOFs (FM ordering), with the zero-energy set to their Fermi levels (E_{Fermi}), are shown in Fig. 5-5. The Zr-, and Th-MOFs have similar DOSs, with identical majority and minority spin states, and have an equal band gap of 3.50 eV. Moreover, both of their HOMO levels mainly consist of the O(2*p*) states, and the LUMO levels are dominated by the metals i.e., Zr(4*d*) and Th(5*f*) states. Thus, the Zr-, and Th-MOFs can be classified as ligand-to-metal charge-transfer insulators (LMCT), where the gaps are associated with the O2*p* to Metal4*d* or Metal5*f* transitions. The similar behavior of Zr and Th can be attributed to their similar electronegativities (1.33 and 1.30 respectively) [156], with Th–O bonds being only slightly more ionic than the Zr–O bonds. For the same reason, there is some degree of hybridization between O(2*p*) and Zr(4*d*) states, which is negligible between the O(2*p*) and Th(5*f*) states.

The U-MOF has completely different bonding properties than the Zr-, and Th-MOFs. The majority and minority states of the U-MOF are not identical because of the FM ordering. Both the HOMO and LUMO levels in the majority spin state (having lower gap than the minority state) mainly consists of the U(5*f*) states, and thus the U-MOF can be classified as a Mott insulator, as the gap is associated with the Metal5*f* to Metal5*f* transition.

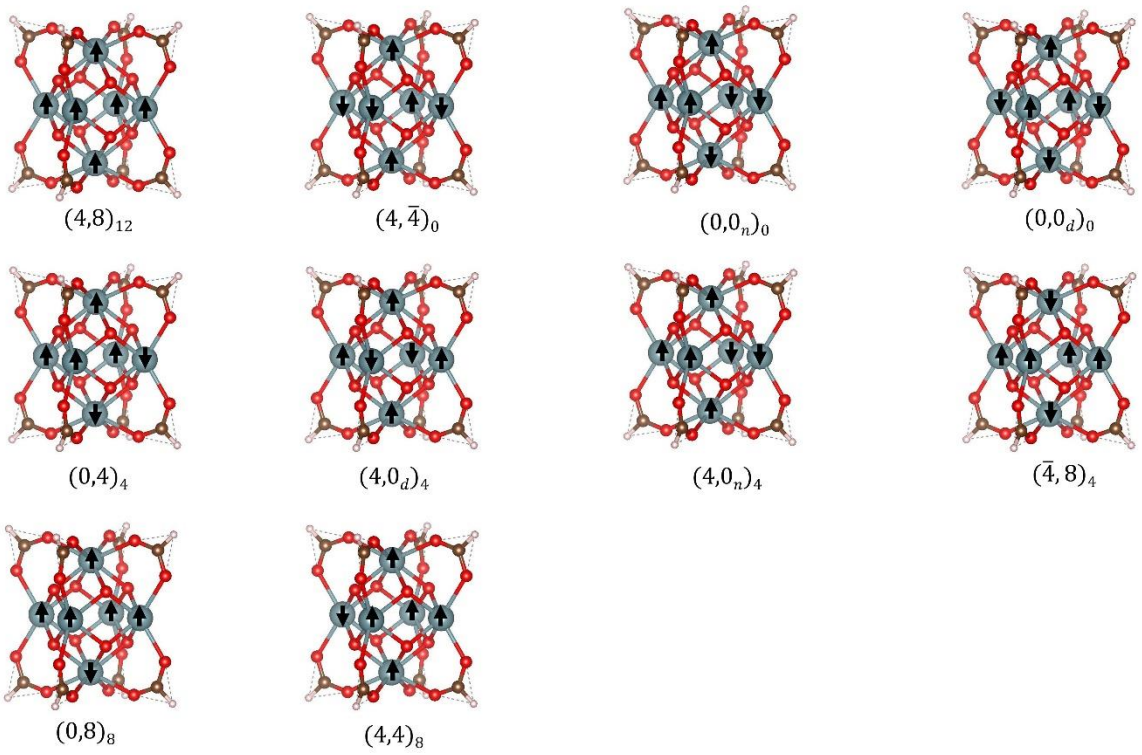

Figure 5-6. The ten different magnetic configurations possible in the U-8 MOF. The nomenclature of the configurations is described in the text.

We also investigate different possible magnetic configurations in the U-8 MOF, besides the ferromagnetic state, to find the lowest energy magnetic state. There are a total of six metal atoms (two axial and four equatorial) in the SBU, which can have different relative magnetic orientations (up-, or down-spin). There are 10 unique configurations that these spins can take including the FM state, as shown in Fig. 5-6. The labeling is defined in terms of the net magnetic moments of the two axial and four equatorial atoms, with the local moment of each atom being two units. The first number in the label of the magnetic ordering represents the net magnetic moment of the two axial atoms. There are thus two possibilities: the two spins are aligned in the same direction (4) and $(\bar{4})$, or the two spins are aligned anti-parallel (0).

The second number in the label represents the net magnetic moment of the four equatorial atoms. Here the first possibility is that all four spins are in the same direction (8) and $(\bar{8})$. The second possibility is that three spins are in one direction and one in the opposite direction (4) and $(\bar{4})$. The final possibility is that there are two up spins and two down spins, for which case the like spins can be neighbors (n) or diagonally opposite each other (d): (0_{n}) and (0_{d}) respectively. The differences between all these cases will become more evident when they are compared for their energies later in the text. The number outside the parentheses in the nomenclature denotes the net magnetic moment of the SBU.

In addition to the GGA+*U* functional, we also employed the meta-GGA SCAN+*U* functional to investigate the magnetic energies, magnetic moments and band gaps of all the different magnetic configurations. Though more expensive than GGA+*U*, the meta-GGA functionals are significantly more computationally efficient for calculations (geometry optimizations) than the very expensive hybrid functionals [57,157]. Although, the meta-GGA functionals are designed to self-consistently overcome any spurious self-interaction errors, we had to use SCAN+*U*, as the conventional SCAN functional results in an extremely low band gap of 0.33 eV, in comparison to GGA+*U* calculated value of 2.70 eV. In the absence of any guidance from the literature, we used the same *U*-*J* value of 4.0 eV for SCAN, which was fitted for GGA-PBE.

The GGA+*U* and SCAN+*U* energies of all the magnetic configurations relative to the FM state are shown in Fig. 5-7. The following discussion explains the differences in their GGA+*U* calculated energies by making flips in the spins of the axial and equatorial atoms in the FM state; first one at a time and then in combination. We take the ferromagnetic states as having all spins pointing upwards, that is $(4,8)_{12}$. A comparison of GGA+*U* and SCAN+*U* calculated

energies is then made later in the text. We find the GGA+*U* calculated collinear-AFM ordering UO_2 is lower in energy by 0.905 eV (per formula unit) than it's FM counterpart. The differences in magnetic energies of the U8-MOF presented below are in the range of 0–0.011 eV.

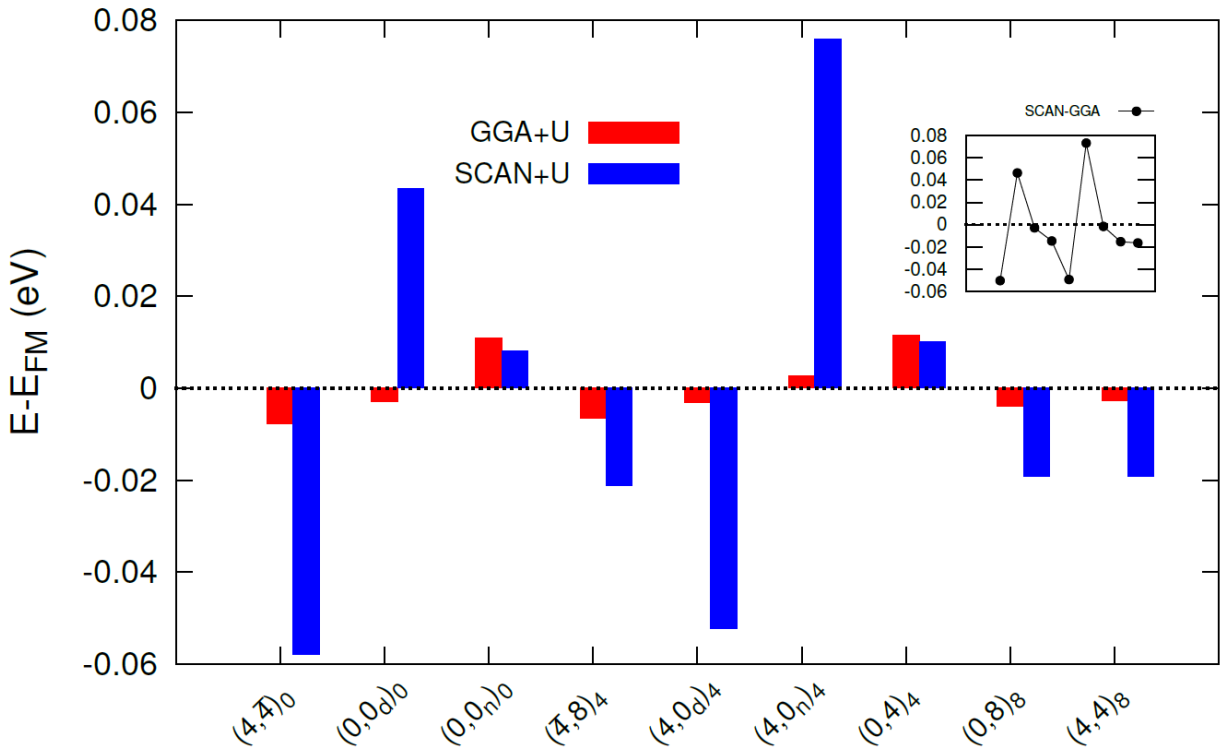

Figure 5-7. DFT energies of the 9 magnetic configurations of U-8 MOF relative to the ferromagnetic (FM) state, calculated using GGA+*U* and SCAN+*U* functionals. The inset shows the difference in the relative energies between SCAN+*U* and GGA+*U* functionals.

Flipping only axial spins: Flipping the spin of one of the axial atoms in the FM state, results in the configuration of $(0,8)_8$ which lowers the energy of FM state by 3.98 meV. Flipping the spins of both axial atoms in the FM state, resulting in the configuration of $(\bar{4},8)_4$, lowers the energy by 6.57 meV.

Flipping only equatorial spins: Flipping the spin of any one equatorial atom in the FM state, resulting in the configuration of $(4,4)_8$, lowers the energy by 2.75 meV. Thus, flipping one axial spin lowers the energy more than flipping one equatorial spin. Flipping the spins of two

equatorial atoms results in two distinct configurations i.e., $(4, 0_n)_4$ and $(4, 0_d)_4$ depending on whether the spins on neighboring or diagonally opposite uranium atoms are flipped. Flipping the spins of any two neighboring uranium atoms of the equatorial plane in the FM state, increases its energy by 2.64 meV. Whereas flipping the spins of any two diagonally opposite atoms lowers the energy by 3.18 meV. The energy increase by flipping the neighboring atom spins can be attributed to magnetic frustration, which is absent when the spins of two diagonally opposite atoms are flipped.

Flipping the spins of any three equatorial uranium atoms in the FM state, resulting in the configuration of $(4, \bar{4})_4$ lowers the energy by 7.76 meV. Flipping the spin of all four equatorial uranium atoms in the FM state is equivalent to flipping both the axial atoms which was discussed above and lowers the energy by 6.57 meV.

Flipping a combination of axial and equatorial spins: Flipping one axial and equatorial atomic spin each in the FM state, resulting in the configuration of $(0,4)_4$ increases the energy by 11.54 meV. Furthermore, flipping one more equatorial spin results in two distinct configurations, i.e., $(0, 0_d)_0$ and $(0, 0_n)_0$ depending on whether the spins on neighboring or diagonally opposite uranium atoms are flipped. The configuration of $(0, 0_d)_0$ is 3.01 meV lower in energy than the FM state, while the configuration of $(0, 0_n)_0$ is higher in energy than the FM state by 10.95 meV. This indicates that the two diagonally opposite equatorial atoms with the same spin are favored over two neighboring equatorial atoms with same spins, similar to the cases above, which is probably due to magnetic frustration. The distant ions are known to have stronger coupling constants than the neighboring ions, which causes the neighboring interactions to be frustrated [158].

Thus, there are six configurations with energies lower than the FM state: $(4,\bar{4})_0$, $(0,0_d)_0$, $(\bar{4},8)_4$, $(4,0_d)_4$, $(0,8)_8$, $(4,4)_8$ as can be seen in Fig. 5-8. However, all these configurations are more stable than the FM state by only less than 10 meV, which is well within the room temperature energy limits, and thus may not be distinguishable physically. Some general principles which can be extracted from these results are as follows. Flipping an axial spin can lower the energy more by an equatorial flip. Flipping the spins of both axial atoms further lowers the energy of the FM state. Any two diagonally opposite equatorial spins flipped together is more energetically favorable than the two neighboring equatorial spins flipped together.

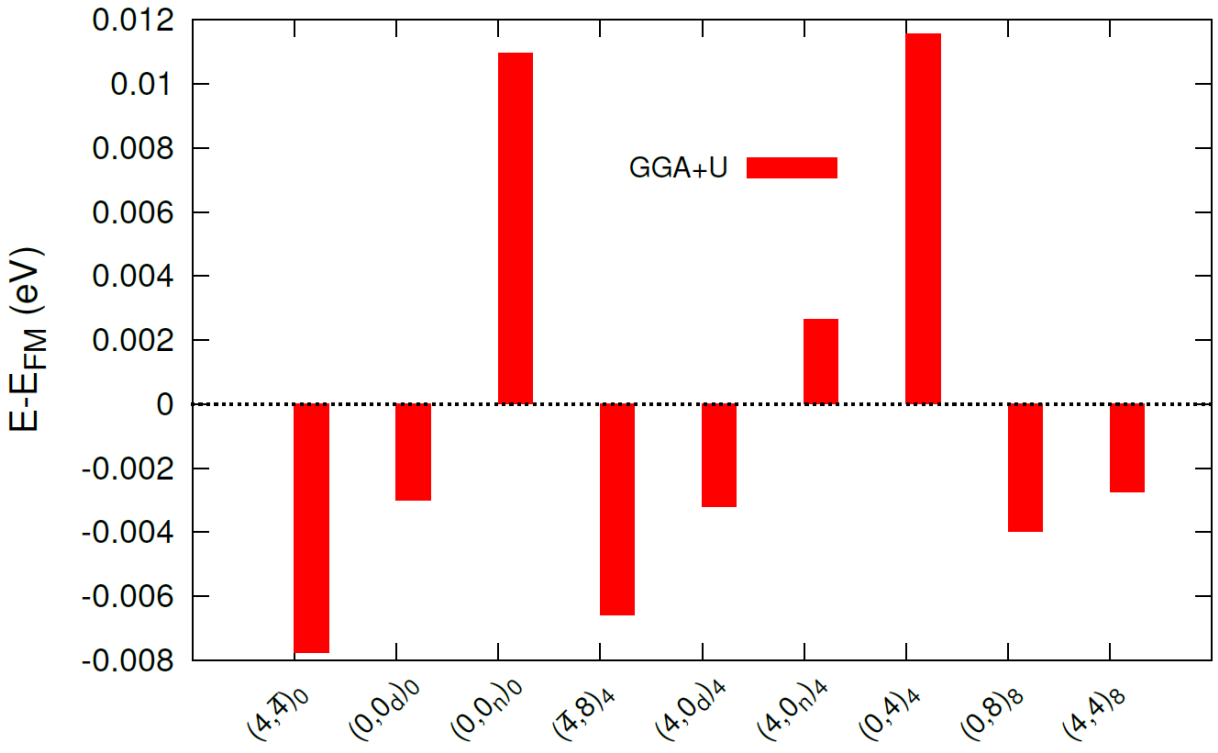

Figure 5-8. GGA+*U* calculated magnetic energies of all the 10 configurations relative to the FM state.

We also calculate the magnetic energies using SCAN+*U* functional, as mentioned earlier in this section. The GGA+*U* and SCAN+*U* calculated DFT energies of all the magnetic configurations of the U-8 MOF, relative to the FM state are shown in Fig. 5-7. While there is no

quantitative agreement between the GGA and SCAN functionals, for 8 out of 9 configurations both functionals make the same prediction as to their stability or instability relative to FM. The GGA+*U* functional results in these magnetic energies in a range of -8.0 meV to 11.0 meV, whereas the SCAN+*U* results in magnetic energies in a range of -60.0 meV to 75 meV. That is, the SCAN functional results in significantly higher magnitudes of magnetic energies than the GGA functional, as can be seen from the inset of Fig. 5-7, which shows the difference between SCAN+*U* and GGA+*U* calculated magnetic energies.

There is very limited literature on the comparison of GGA-PBE and SCAN functionals to probe magnetism in materials, and none for actinide compounds. However, Fu et al. [157] found that the SCAN functional is not able to provide a good description of magnetism in transition metal ferromagnets Fe, Co and Ni. They attributed this limitation of SCAN to its overestimated tendency towards magnetism and exaggeration of magnetic energies. Although, calculations done to this date [43,44,55,159,160] confirm a high accuracy of SCAN for describing thermodynamics and/or electronic structure of many materials, SCAN may not necessarily be a superior functional for magnetism. Based on this very limited information, we thus believe that the GGA-PBE results are more likely to reliable than the SCAN results.

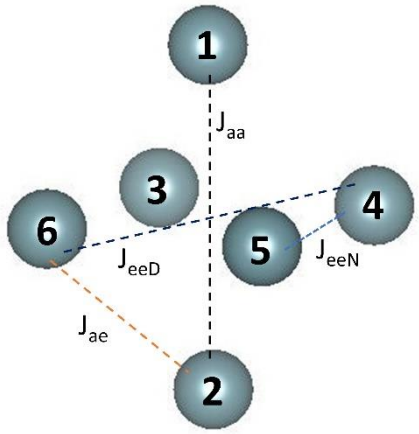

Figure 5-9. Four different magnetic interactions in the U-8 MOF. Only the metal-sites are shown for simplicity.

We also fitted the GGA+U magnetic energies of all ten configurations using the Ising spin configurations, and thus extracted the Heisenberg exchange coupling constants. The four different interactions between the metal sites are shown in Fig. 5-9. The Heisenberg Hamiltonian for the DFT magnetic states can be represented as,

$$\begin{aligned}\widehat{H} = E_0 - J_{aa}(S_1.S_2) \\ - J_{ae}(S_1.S_3 + S_1.S_4 + S_1.S_5 + S_1.S_6 + S_2.S_3 + S_2.S_4 + S_2.S_5 \\ + S_2.S_6) - J_{eeN}(S_3.S_4 + S_5.S_6) - J_{eeD}(S_3.S_5 + S_4.S_{6)}\end{aligned} \quad (5\text{-}1)$$

where, E_0 is the zero of the energy which is implicitly present in the calculations, J_{aa} is the coupling between two axial sites, J_{ae} is the axial-equatorial coupling, J_{eeN} is the coupling between two nearest neighbor equatorial sites, and J_{eeD} is the coupling between two diagonally opposite equatorial sites. $S_i.S_j$ is the dot product of the spins of two sites i and j. In this case, we have five unknowns, i.e., four exchange coupling constants and one zero of the energy, and ten equations, i.e., the Ising energies of ten magnetic configurations. Thus, we have an *overdetermined* system of equations. We have employed the least-squares method to extract the set of unknowns which minimizes the squared Euclidean 2-norm $||AX - B||_2^2$. Here, A is a 10×5 matrix representing the ten Heisenberg Hamiltonians as shown in Eq. 5-1, X is a 5×1 matrix representing five unknowns, and B is a 10×1 matrix representing the DFT magnetic energies.

The least-squared extracted exchange coupling constants are given in Table 5-3. The magnitude and sign of the coupling constant J_{ij} gives the coupling strength between sites i and j, and the nature of spin interaction (i.e., ferromagnetic or anti-ferromagnetic) respectively. The axial-axial interaction is the strongest, followed by the two equatorial-equatorial interactions, with the diagonally opposite interaction slightly stronger than the nearest-neighbor interaction, and the axial-equatorial interaction is the weakest. The axial-axial and diagonally opposite

equatorial interactions are predicted to be ferromagnetic, while the axial-equatorial and nearest-neighbor equatorial interactions are predicted to be anti-ferromagnetic. These spin-interactions can be used to justify the lowest energy configuration of $(4, \bar{4})_0$, where the axial-axial interaction is ferromagnetic, six out of eight axial-equatorial interactions are anti-ferromagnetic, one out of two diagonally opposite equatorial interaction is ferromagnetic, and two out of four nearest-neighbor interactions are anti-ferromagnetic. Similarly, the high magnetic configuration of $(0, 0_n)_0$ has unfavorable anti-ferromagnetic axial-axial interaction, four out of eight unfavorable ferromagnetic axial-equatorial interactions, both unfavorable anti-ferromagnetic diagonally opposite-, and nearest-neighbor-equatorial interactions.

Table 5-3. Least-squared extracted exchange coupling constants and their spin-interactions in the U-8 MOF

Coupling type J_{ij}	Coupling constant (cm^{-1})	Nature of spin interaction
J_{aa}	+12.96	Ferromagnetic
J_{ae}	-0.96	Anti-ferromagnetic
J_{eeN}	-3.34	Anti-ferromagnetic
J_{eeD}	+4.92	Ferromagnetic

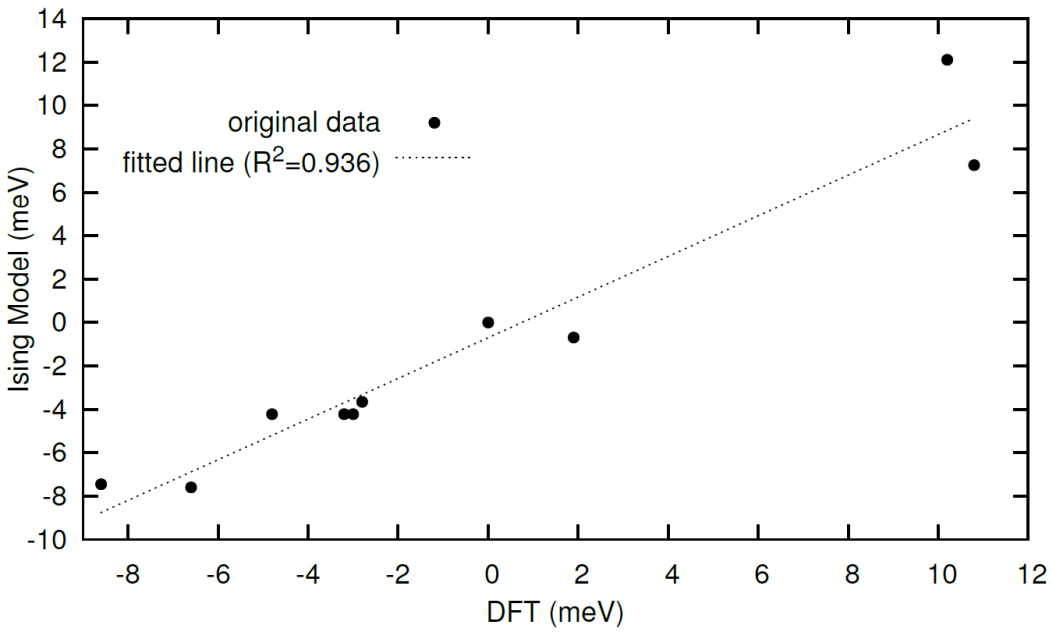

Figure 5-10. Comparison of DFT (GGA+*U*) calculated magnetic energies with those predicted by the Heisenberg Hamiltonian of the Ising configurations

We also compared the true DFT magnetic energies and the Ising model predicted magnetic energies of the nine magnetic states with respect to the ferromagnetic state, as shown in Fig. 5-10. The R^2 value of 0.936 indicates a decent fit to the magnetic energies, though the two highest energy states lie away from the fit.

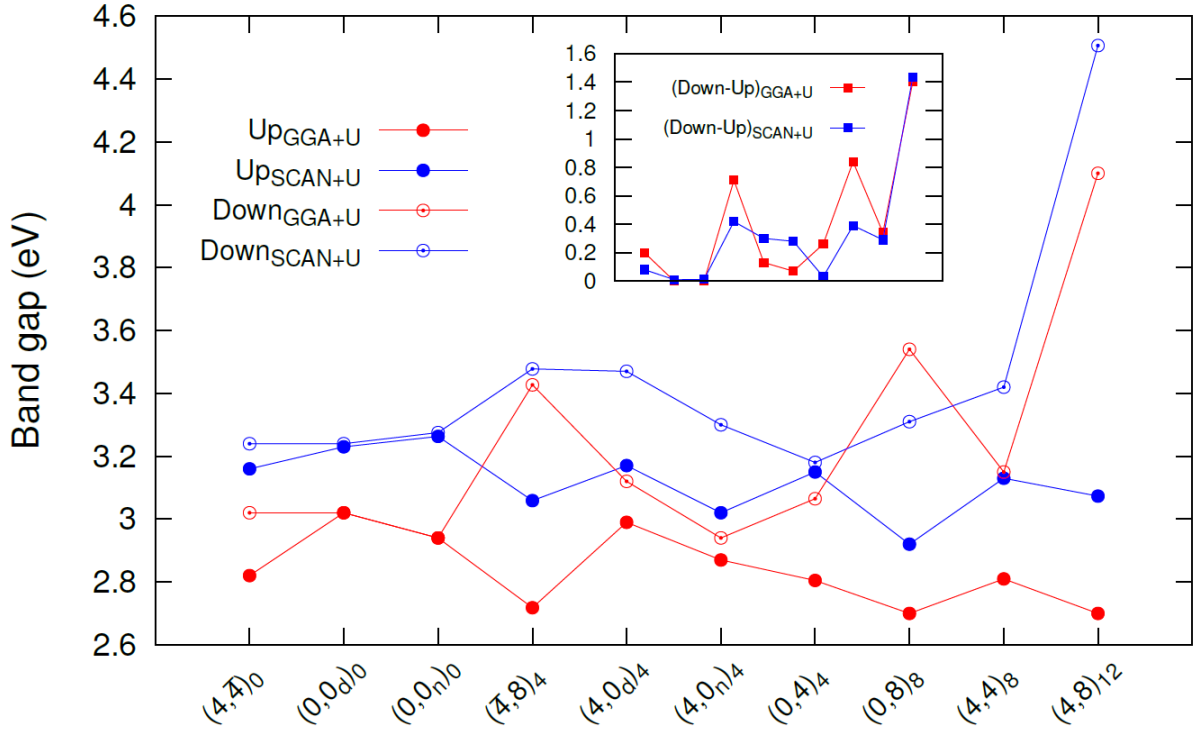

Figure 5-11. Up-, and down-spin band gaps of all the 10 magnetic configurations of the U-MOF, calculated using GGA+*U* and SCAN+*U*. The inset shows the difference between the down-, and up-spin band gaps for both GGA+*U* and SCAN+*U*

In addition to the thermodynamics, we also compared the GGA+*U* and SCAN+*U* calculated majority (up)-, and minority (down)-spin band gaps of the 10 magnetic configurations of the U-MOF, as shown in Fig. 5-11. The SCAN+*U* functional agrees well with the GGA+*U*, in contrast to the magnetic energies above, and results in band gaps 0.1–0.4 eV higher than the GGA+*U* functional, depending on the magnetic configuration. The higher magnitudes of SCAN+*U* band gaps than the GGA+*U* functional is expected, as SCAN is a semilocal meta-

GGA functional which does not suffer from the self-interaction errors of the *f*-electrons. Thus, the consistency of electronic structure description for a GGA and a meta-GGA system would largely depend upon the *U-J* value used. We have used the same *U-J* value (4.0 eV) for both GGA and SCAN functionals here, which might not be the accurate value for SCAN as it was fitted for the GGA XC-functional.

The inset of Fig. 5-11 shows the difference between down-, and up-spin band gaps, for both GGA+*U* and SCAN+*U* functionals, and these differences are also contained in a range of 0–0.4 eV for the two functionals. The minority and majority spin states generally tend to move apart more as the magnetic moment increases, with the ferromagnetic state (largest magnetic moment= 12 μ_B) having the largest difference (1.40 eV) between the two spin states.

Thus, the U-MOF needs spin-polarization, while the Zr-, and Th-MOFs are insensitive to spin and can be classified as diamagnetic in nature.

5.3.4 Relativistic Effects

We have also investigated the relativistic effects on the band gap and DOS using spin-orbit coupling (SOC) calculations. The inclusion of SOC did not change the band gaps of Zr-, and Th-MOFs, while decreasing the bandgap of U-MOF by only 0.04 eV.

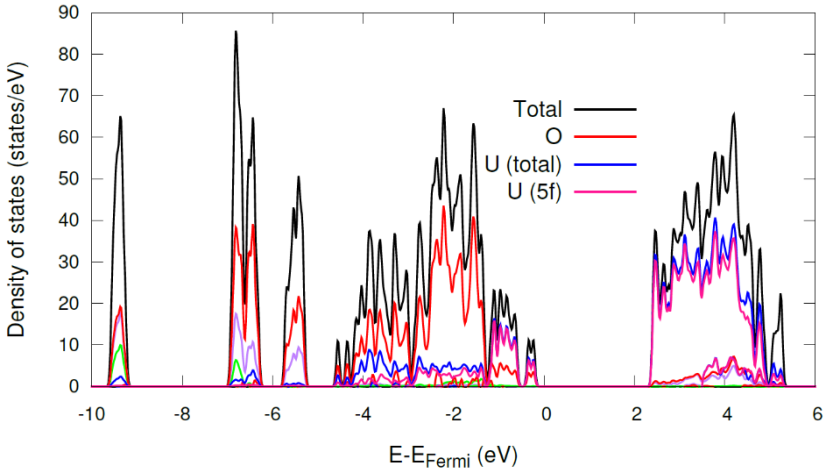

Figure 5-12. GGA+*U*+SOC calculated p-DOS of the ferromagnetic state of U-8 MOF

These results are consistent with the previous literature on the effects of SOC on the electronic structure of the corresponding oxides [161], where SOC only marginally affects their band-gaps. Fig. 5-12 shows the GGA+*U* calculated p-DOS of the ferromagnetic state of U-MOF, and it can be clearly seen, that the band edges still mainly consist of the U(5*f*) states, as was in the case of without SOC above. Thus, the DOS and band gaps of these MOFs are robust with SOC and will be treated without SOC inclusion in the rest of chapter.

5.3.5 Origin of Band Gap in MOFs

In order to determine the origin of band gaps in the MOFs in this work, i.e., to determine whether the gap originates from the metal-nodes (or SBU) or the linkers connecting the metal nodes, we considered a truncated model with one SBU connected with one Me_2BPDC^{2-} linker (Fig. 5-13). We then calculated the p-DOS of this "SBU+linker" model, and the isolated linker alone; these are compared these with the p-DOS of SBU. The ferromagnetic U-8 MOF is considered as a representative case. Initially, partial occupancies and an overestimated net magnetic moment (16 μB instead of 12 μB) were obtained, which were overcome by adding four $(OH)^-$ groups to the four equatorial metal atoms, as shown in Fig. 5-13. Two of those equatorial metal atoms are also attached to the linker via oxygen atoms of the linker.

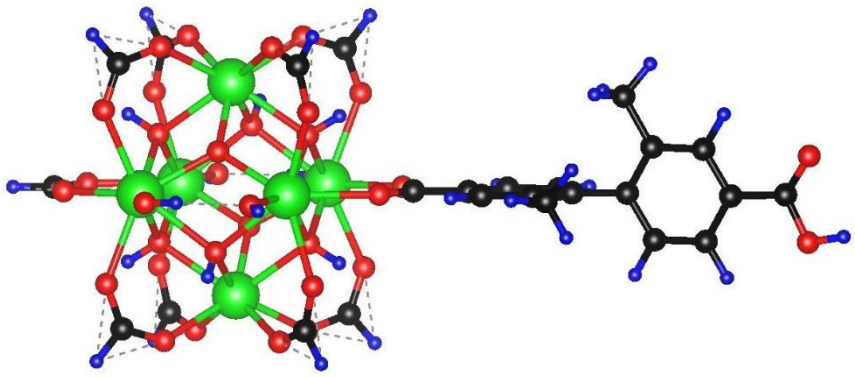

Figure 5-13. Truncated model of the M-8 MOF, with one SBU connected to a Me_2BPDC^{2-} linker. The green, red, black, and blue spheres represent M, O, C, and H, respectively

The GGA-PBE calculated band gap of the isolated Me_2BPDC^{2-} linker was found to be 3.80 eV. By contrast, the GGA+*U* calculated up-channel band gap of the uranium based SBU+linker truncated model was found to be only 3.0 eV, which is close to the 2.70 eV up-channel band gap of the U-8 SBU. The difference of 0.30 eV probably arises from the additional four $(OH)^-$ groups attached to the metal atoms, which are not present in the SBU. We verified this difference by calculating the band gap of the isolated SBU with four additional $(OH)^-$ groups and found it to be 3.0 eV as well. However, the down-channel band gap of the SBU+linker model was found to be 3.80 eV, which is interestingly the gap of the linker itself.

The up-channel band edges of the SBU+linker model were found to be dominated by U(5*f*) states, as shown in Fig. 5-14(a). This is almost identical to the up-channel U(5*f*) band edges in the case of U-8 SBU. While the down-channel HOMO band of the SBU+linker model is still dominated by the O(2*p*) states with some degree of hybridization with C(2*p*) orbitals, as in the case of the SBU, the LUMO band is now dominated by the C(2*p*) states, which in the case of the SBU was dominated by U(5*f*) states.

We further projected out the C(2*p*) states associated with only those carbon atoms present in the linker and compared with those making up the SBU, in the SBU+linker model, and found that the carbon atoms of the linker group dominate the LUMO edge, while those carbon atoms from the SBU lie further away from the LUMO edge, as shown in Fig. 5-14(b). The HOMO band of the linker is associated with O(2*p*) states hybridized with C(2*p*) states, while the LUMO band is associated with the C(2*p*) states, as shown in Fig. 5-15. Thus, the up-channel states (lower band gap) are dominated by the SBU, and the down-channel (higher band gap) states are dominated by the linker.

Thus, it can be concluded that, the lower band gap molecule (either of metal-node or organic linker) determines the band edges of the whole system, which are actually associated with any electronic transitions for conductivity.

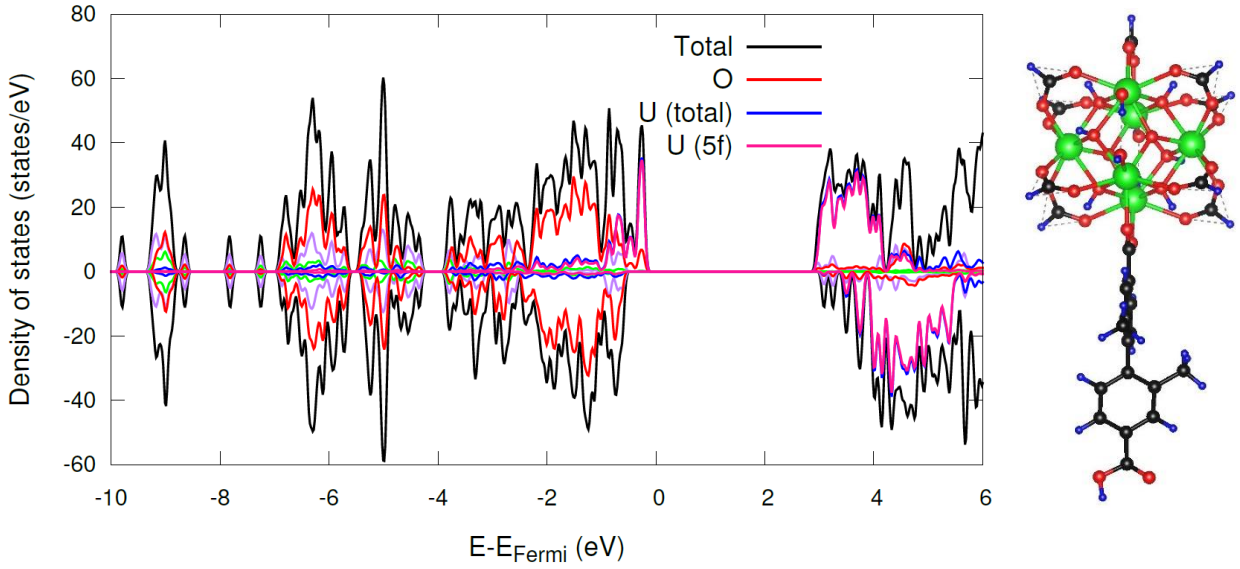

(a) p-DOS of U-8+Me$_2$BPDC^{2-} (SBU+linker)

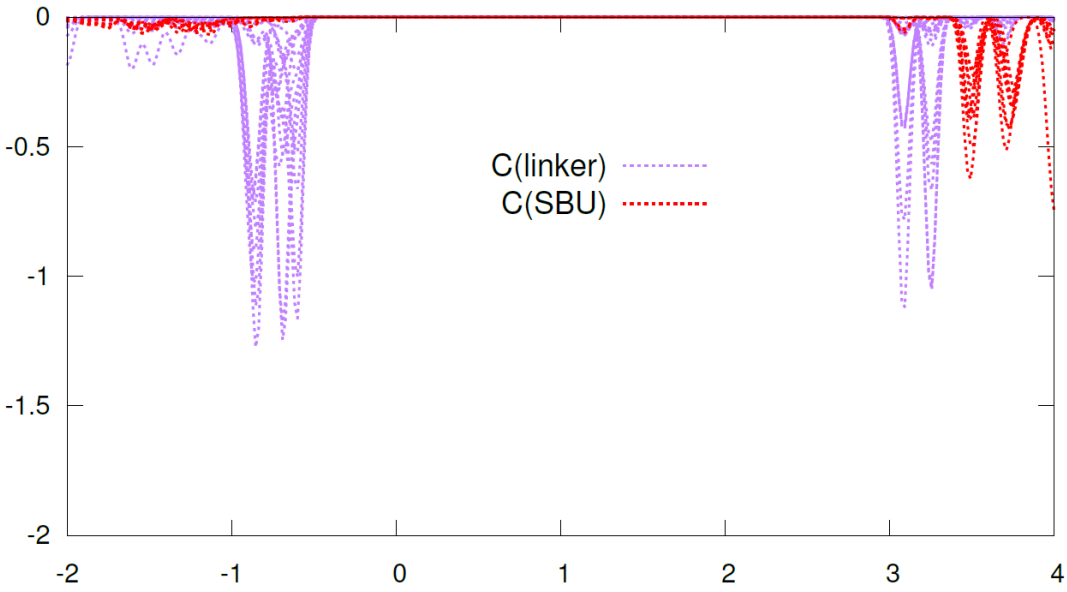

(b) p-DOS of carbon atoms of linker group and SBU projected separately, in the SBU+linker model

Figure 5-14. GGA+*U* calculated p-DOS of (a) U-8 SBU+Me$_2$BPDC^{2-} model (b) p-DOS of the carbon atoms associated with the linker group and SBU projected out separately

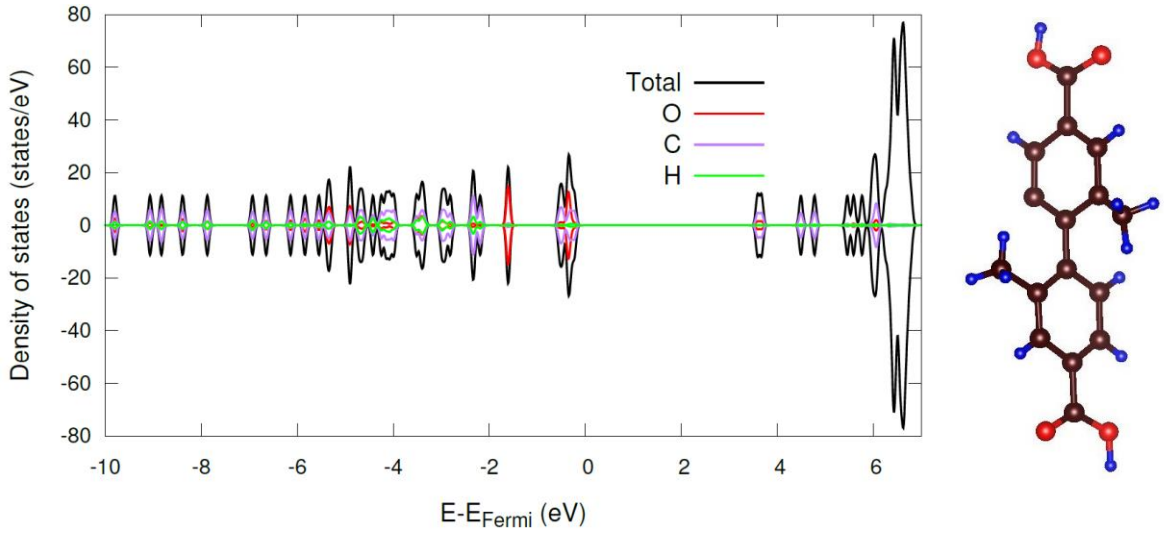

Figure 5-15. p-DOS of the isolated Me_2BPDC^{2-} linker

5.3.6 Effect of XC-Functionals

We have also investigated the band gaps of all the MOF SBUs, using different levels of XC-functionals, i.e., GGA-PBE→SCAN→hybrids. As in the previous conclusions, we employed spin-polarized GGA+*U* and SCAN+*U* methods for the ferromagnetic U-MOF, with a *U*-*J*=4.0 eV, whereas non-spin polarized method with no DFT+*U* corrections were used for the Zr-, and Th-MOFs. We employed the B3LYP and HSE hybrid functionals, as also described in the methods section earlier. Fig. 5-16 shows the band gaps of the SBUs for different XC-functionals. We find that, the SCAN and hybrid functional calculated band gaps are significantly higher than the GGA-PBE band gaps for Zr-, and Th-MOFs, unlike for the case of U-MOF. SCAN calculated band gaps for the Zr-, and Th-MOFs are 0.83 eV (~23%) higher than their corresponding GGA-PBE values. Similarly, the HSE calculated band gaps of Zr-, and Th-MOFs are 1.70 eV (~50%) higher than their GGA-PBE values, while the B3LYP calculated values deviate the most, by 2.0 eV (~57%). On the contrary, the U-MOF band gap calculated by

different levels of theories lie within an interval of 0.30 eV (~11%), with respect to the GGA+*U* functional.

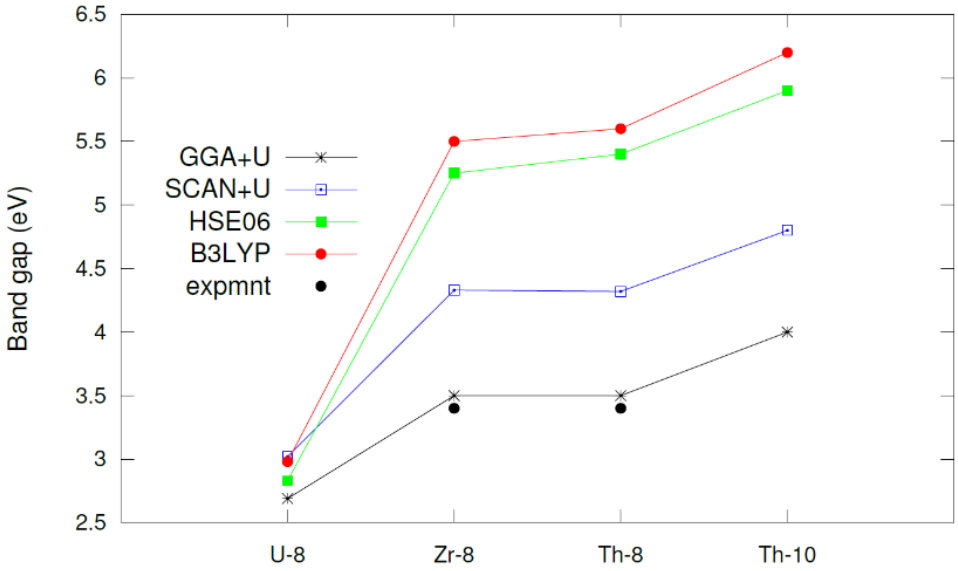

Figure 5-16. Band gaps of the U-8, Zr-8, Th-8 and Th-10 SBUs for different levels of XC-functionals.

We also compared these results to the optical band gaps for the Zr-, and Th-MOFs, as measured by Shustova and co-workers [103,110]. We find that, the GGA-PBE calculated values are consistent with the experimental values, while the SCAN and hybrid functionals largely overestimating their band gaps. Although, the hybrid functionals are known to typically perform well to describe the electronic structures of a material, we find that this is not the case in this for these systems. To further investigate the origin of this discrepancy, we compared our calculated band gap results for the MOFs to those of their corresponding oxides, present in the literature, as shown in Table 5-4.

The calculated band gaps of the MOF SBUs in this work using the various functionals, follows the same trend as that of their oxides, i.e., the hybrid calculated values are larger than the GGA-PBE values. The difference between GGA and hybrid values for the zirconium-, and

thorium oxides are larger than the those for the uranium oxides, as is also the case for their MOFs. Moreover, the order of the calculated band gaps of the MOF SBUs is similar to that of their oxides, i.e., 4.0–4.5 eV for the GGA-PBE calculated values for Zr-, and Th-systems, and 5.5–6.0 eV for their hybrid values. Similarly, the GGA-PBE calculated values for the U-systems are of the order of 2–2.50 eV, and their hybrid calculated values (2.7–3.2 eV) not being significantly higher than the GGA-PBE values, as is the case for the U-MOF. The same order of the band gaps of the MOF SBUs and their oxides can be attributed to the similar coordination of the metal in both the systems.

We also did a test calculation on the Th-MOF using the *Gaussian* [128] electronic structure code, which employs orbital basis sets, to isolate the effects of periodic boundary conditions as present in the case of plane-wave basis sets in VASP. Using the B3LYP level of theory and the basis sets as described in the methods section earlier, we found the Gaussian calculated band gap to be 5.66 eV, which is only marginally smaller than the 5.71 eV gap calculated by VASP. Thus, the two suites of basis sets are robust.

Table 5-4. Calculated and experimental band gaps of the Zr-, U-, and Th-MOFs in this work, compared to the band gaps of their corresponding oxides, in the literature. Numbers in the brackets denotes the coordination number of the metal atoms present in that system.

MOF SBU (coordination number)	Band gap (this work) (eV)	Oxide (coordination number)	Oxide band gap (literature) (eV)
Zr-8 (8 and 6)	3.50^{GGA}, 5.26^{HSE06}, 5.54^{B3LYP}, 3.4^{exp}	ZrO_2 (8)	[130]: 4.43^{GGA}, 6.13^{PBE0}, 5.5^{exp}
		UO_2 (8)	[162]: 2.27^{LDA+U}, 2.71^{HSE06}, 2.0^{exp}
		U_4O_9 (8)	[162]: 1.68^{LDA+U}
		U_3O_7 (8)	[162]: 1.59^{LDA+U}
U-8 (8 and 6)	2.69^{GGA+U}, 2.83^{HSE06}, 2.98^{B3LYP}	α-U_3O_8 (7)	[162]: 3.43^{LDA+U}, 1.67^{exp}
		α-UO_3 (8)	[162]: 0.94^{LDA+U}, 3.10^{HSE06}, 2.60^{exp}
		ɣ-UO_3 (6)	[162]: 2.35^{LDA+U}, 2.38^{exp}
Th-8 (8 and 6)	3.50^{GGA}, 5.32^{HSE06}, 5.71^{B3LYP}, 3.4^{exp}	ThO_2 (8)	[137]: $4.8^{PBE-sol}$, 5.90^{exp}
Th-10 (8 and 7)	4.0^{GGA}, 5.95^{HSE06}, 6.22^{B3LYP}		[163]: 4.7^{GGA+U}, 6.2^{HSE06}

5.4 Conclusions

A detailed characterization of the electronic structures of Zr-, Th-, and U-based MOFs was carried out using DFT calculations. The band gaps and p-DOSs were investigated using various DFT methods such as DFT+*U*, spin-polarization, SOC, and different XC-functionals (GGA→metaGGA→hybrids). The Zr-, and Th-MOFs were found to be robust with DFT+*U* and spin-polarization, while all the MOFs were found to be robust with SOC. As expected, the U-MOF needs DFT+*U* corrections for accurate description of the electronic structures and was found to be sensitive to spin. The Zr-, and Th-MOFs have similar band gaps and electronic structures and are found to be ligand-to-metal (LMCT) charge transfer insulators. The GGA-PBE calculated band gaps of both these MOFs are of the order of 3.5-4.0 eV which are consistent with their insulating properties as also observed experimentally by Shustova and co-workers [103,110]. The U-MOF on the contrary has a GGA+*U* calculated band gap of 2.69 eV and can be characterized as a Mott insulator.

The U-MOF was found to show 10 different magnetic configurations based on relative spins of the six metal ions. Of these 10 configurations, there is one high-spin state i.e., the FM state with net-magnetic moment of 12 μB, three low-spin states with perfect anti-ferromagnetic ordering and zero net-magnetic-moments, and six intermediate-spin states with net-magnetic moments of 4 μB and 8 μB. We characterized all these spin configurations for their energies relative to the FM state and band gaps, using the GGA+*U* and SCAN+*U* XC-functionals. There was no quantitative agreement found between the GGA and SCAN functionals to determine the ground state magnetic configuration. However, for 8 out of 9 configurations both functionals make same predictions for their relative stabilities with respect to the FM state. The SCAN functional is known to overestimate the magnetic energies as described earlier in the text, and

thus GGA-PBE predicted states can be expected to be more reasonable. By contrast to the magnetic energies, the GGA+*U* and SCAN+*U* functionals agree pretty well for the band gaps of all the magnetic configurations.

Our DFT calculations show that the origin of band gap in a MOF can be identified by modeling the isolated metal-nodes (SBUs) and the organic linkers separately and comparing them to a truncated model of SBU+linker. The p-DOS of all these models can further help in disentangling the HOMO and LUMO edges and thus give an insight to the bonding characteristics of a MOF. The MOFs thus can be tuned for their electronic structures taking advantage of the reticular chemistry [164] and using these predictions.

The SCAN and hybrid (HSE and B3LYP) functional calculated band gaps were found to be significantly higher (up to 50%) than the GGA-PBE calculated values, for Zr-, and Th-MOFs. By contrast, the band gap of U-MOF calculated by different XC-functionals lie within 11% with respect to the GGA+*U* functional. Furthermore, we found the band gaps of the MOFs to be of the same order as their oxides, which can be attributed to the similar coordination environment of the metal nodes in both the systems.

CHAPTER 6
BAND-GAP ENGINEERING IN METAL-ORGANIC FRAMEWORKS (MOFs)

6.1 Background

Chapter 5 discussed the electronic structures of pure Zr-, Th-, and U-MOFs and the origin of band gap in MOFs. This chapter discusses various ways in which the band gap of a MOF can be engineered or modulated. Cutting-edge research is being done on MOFs utilizing their electronic structure tunability, for many applications, including semiconductor technologies, supercapacitors, high surface area conductors, photocatalysis [21,165,166]. One of the challenges that has to be overcome for such applications is preparation of conductive hybrid materials, that preserve MOF crystallinity without blocking their pores.

There have been studies showing accommodation of a second metal in a MOF matrix without loss of crystallinity, which also resulted in band gap modulation of the MOFs [143,167,168]. Thus, the electronic properties of a MOF can be tailored through "guest metal" immobilization at the metal nodes. In this chapter, we demonstrate three different ways to modulate the band gap of a MOF, (1) metal node substitution; (2) metal node extension with a transition metal; and (3) choice of linker.

6.2 Computational Methods and Structures

6.2.1 Structures

The MOF structures discussed in this chapter can be divided into three groups, (1) MOF SBUs to be used for metal ion substitution; (2) metal node extension of the M-8 MOF (SBU) using Co-ions; and (3) type of linkers, namely Spiropyran and Merocyanine [169,170]. The MOF SBUs have already been described in detail in Chapters 4 and 5. The metal atoms used for doping are Am, Cm, Th, U and Tc, which are the same species used in the ion-exchange process in Chapter 4. Description of metal node extension and linkers is as follows.

Metal-node extension: The metal nodes at the equatorial positions of the M-8 SBU are unsaturated, which is a requirement for metal node extension [110]. They can thus be extended using four transition metal ions such as cobalt, to result in M-Co-8 structure, as shown in Fig. 6-1. Each cobalt atom is linked to two carboxyl groups (−COO−) via oxygen atoms. This also results in unlinking of the carboxyl groups attached to the axial atoms, and thus the axial atoms are now only coordinated to four oxygen atoms, rather than to eight oxygens in the M-8 SBU. The cobalt atoms in addition to being linked to the carboxyl groups are also linked to two oxygen atoms each in the equatorial plane. Thus, each cobalt atom is linked to four oxygen atoms.

One formula unit stoichiometry of the M-Co-8 SBU can be represented as $M_6(COOH)_8O_8Co_4O_4$, which is four formula units of cobalt-oxide (CoO) added to one formula unit of M-8 SBU. The additional (CoO) units thus preserves the charge neutrality of the M-8 SBU.

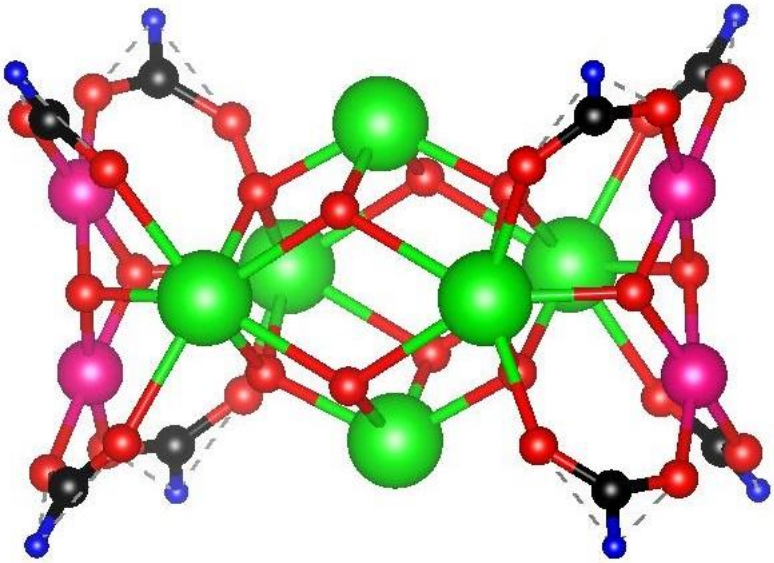

Figure 6-1. M-Co-8 structure resulting from node extension of M-8 SBU. The green, red, black, blue, and pink spheres represent M, O, C, H, and Co respectively.

Spiropyran and Merocyanine linkers: Similar to the Me_2BPDC^{2-} linker joining two SBUs, as discussed previously in Chapters 4 and 5, the Spiropyran and Merocyanine linkers can also join two SBUs, as shown in Fig. 6-2. These two linkers are actually structural isomers of each other and can undergo thermal reversion. The UV irradiation of Spiropyran motif at room temperature, is known to open its photochemical ring which converts it to the Merocyanine motif [171]. The removal of irradiated light decreases the absorbance in the red spectral range and the motif switches back to its original form. The duration of switching back process is determined by the thermal relaxation time which is of the order of 20-400 s. The Merocyanine linker is known to be photo-activated, i.e., conducting, and switches to the resistive state of Spiropyran upon thermal reversion [170].

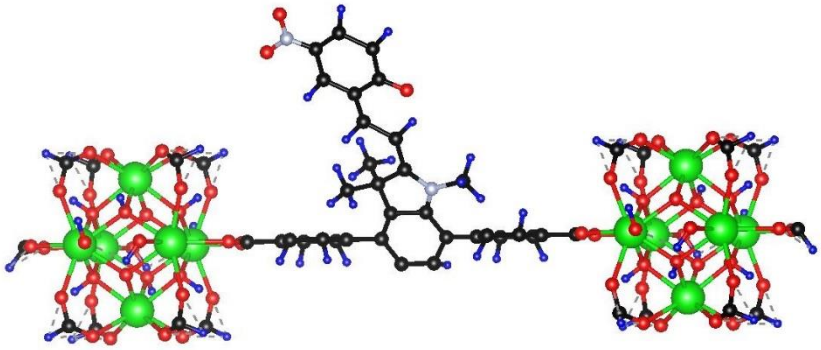

(a) Merocyanine linker joining two SBUs

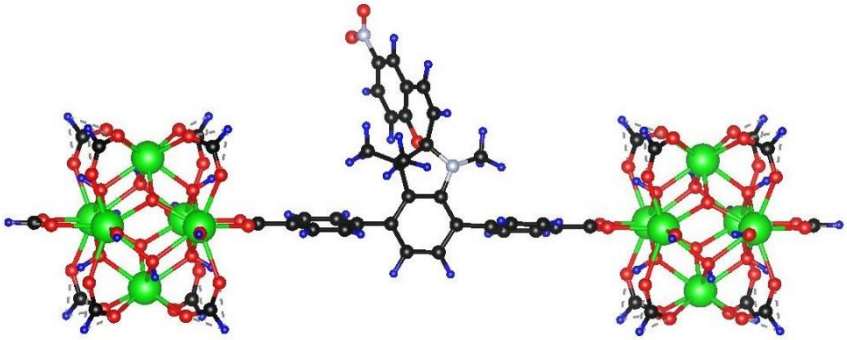

(b) Spiropyran linker joining two SBUs

Figure 6-2. Two SBUs joined by (a) Merocyanine linker and (b) Spiropyran linker. The green, red, black, blue, and gray spheres represent M, O, C, H, and N respectively.

The merocyanine linker (Fig. 6-2(a)) is a group of three phenyl rings, with the central ring orthogonal to the two terminal rings. The central phenyl ring is attached to two carbon atoms and a $–(CH_3N)–$ group, via two of its adjacent carbon atoms, which all together forms a penta-ring. One of the carbon atoms of this penta-ring is terminated by two methyl groups $–(CH_3)–$. The other carbon atom is attached to a $–(C_2H_2)–$ group, which is further terminated by another phenyl ring. This terminal phenyl ring is attached to a $–(NO_2)–$ group via one of the carbon atoms, and also to an $O^{2–}$ group via another carbon atom, such that the $–(NO_2)–$ and $O^{2–}$ groups are on opposite sides of the ring. The two terminal phenyl rings, part of the group of three phenyl rings attached in series, are terminated by (−COO−) groups. These formic acid groups connect the linker to the two SBUs via oxygen atoms. One formula unit stoichiometry of the merocyanine linker is $C_{33}N_2O_7H_{26}$.

The Spiropyran linker (Fig. 6-2(b)) is just a structural isomer of the Merocyanine linker and can be described as the closed state of Merocyanine. Specifically, the $–(C_2H_2)–$ group of the Merocyanine linker closes to form a hexa-ring with the $O^{2–}$ group attached to the terminal phenyl ring. These two linkers attached to the two SBUs will be investigated for their electronic structures in the later sections.

6.2.2 DFT Methods

The DFT settings are the same as used in Chapters 4 and 5. The *U-J* values are specified later in the text, wherever necessary.

6.3 Results and Discussions

6.3.1 Substitution at Metal-Node

Substitutions of the metal atoms with Am, Cm, Tc, Th and U were carried out in the Zr-, Th-, and U-MOFs, to determine the effects of substitution on their electronic structures. Up-

channel and down-channel GGA+*U* calculated band gaps of Am, Cm, Tc, Th and U substituted (position 1) Zr-, Th-, and U-8 SBUs are shown in Fig. 6-3, Fig. 6-4 and Fig. 6-5 respectively. Band gaps of pure MOF SBUs are also shown for comparison. A *U-J* value of 4.0 eV was used for U, Am, and Cm atoms and a *U-J* value of 1.13 eV was used for Tc, for accurate description of Coulomb interactions, based on previous literature [138,172].

Am and Cm substitution decreases the up-channel band gap of Zr-8 MOF the most, i.e., from 3.50 eV to 0.30 eV and 0.25 eV respectively, while not affecting the down-channel gap of 3.50 eV. Tc substitution decreases both the up-, and down-channel band gaps of Zr-8 MOF almost by the same amounts, i.e., to 1.27 eV and 1.37 eV respectively. U substitution decreases the up-channel band gap to 2.92 eV, while not affecting the down-channel gap.

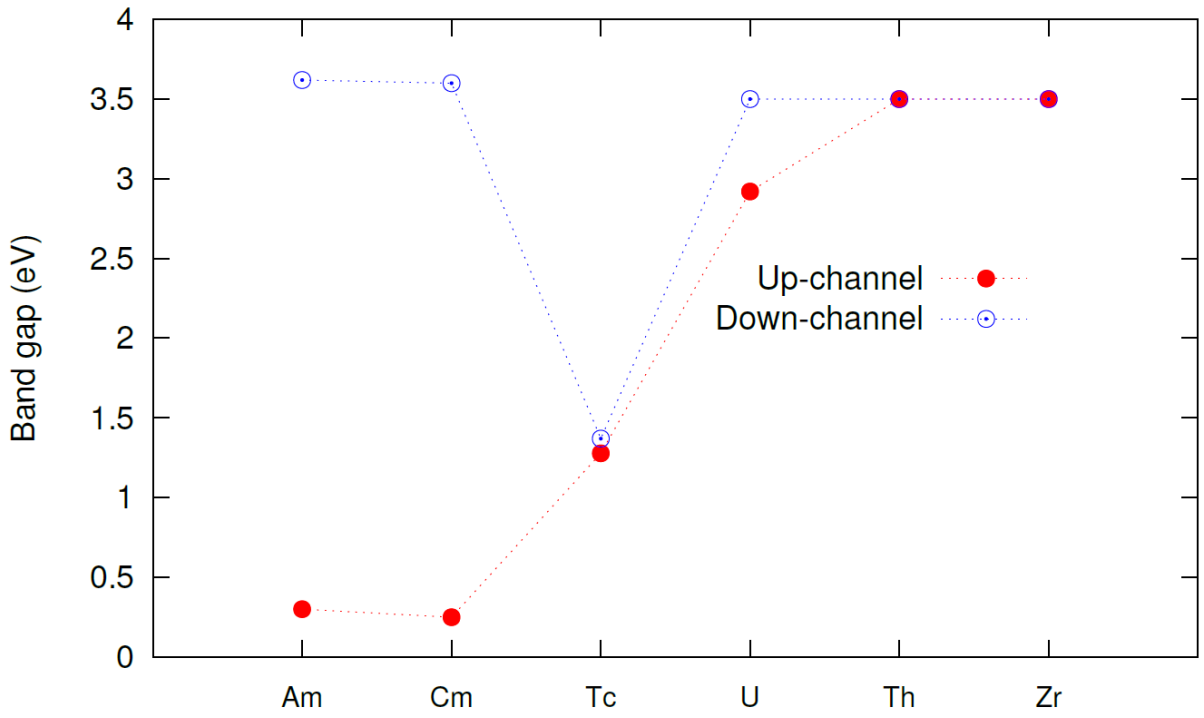

Figure 6-3. GGA+*U* calculated up-channel and down-channel band gaps of Am, Cm, Tc, U and Th substituted (position 1) Zr-8 MOF

Substitution of Th with Am, Cm, Tc, and U in the Th-8 MOF gives similar results to the Zr-8 MOF. Am and Cm substitution decreases the up-channel band gap from 3.50 eV to 0.30 eV and 0.15 eV respectively, while not affecting the down-channel band gap. Tc substitution decreases the up-channel band gap to 1.55 eV and the down-channel gap to 0.94 eV. U substitution decreases the up-channel band gap to 3.30 eV without changing the down-channel gap.

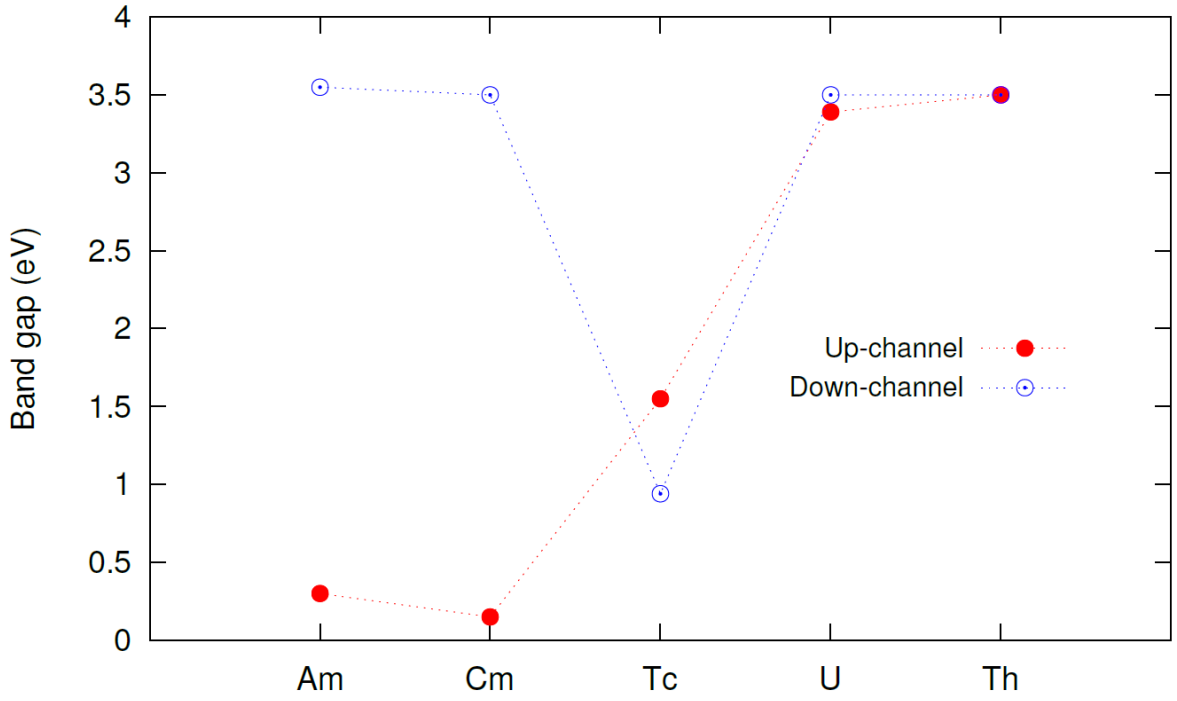

Figure 6-4. GGA+*U* calculated up-channel and down-channel band gaps of Am, Cm, Tc, and U substituted (position 1) Th-8 MOF

Substitution in the U-8 MOF behaves differently than the Zr-, and Th-8 MOFs. Am and Cm substitution in U-8 MOF decreases the up-channel band gap from 2.69 eV to 1.83 eV and 1.65 eV respectively, while decreasing the down-channel gap from 4.10 eV to 2.66 eV and 2.71 eV respectively. Tc substitution decreases the up-channel band gap from 2.66 eV to 0.88 eV and

the down-channel band gap from 4.10 to 1.52 eV. Th substitution does not change the band gap of U-8 MOF.

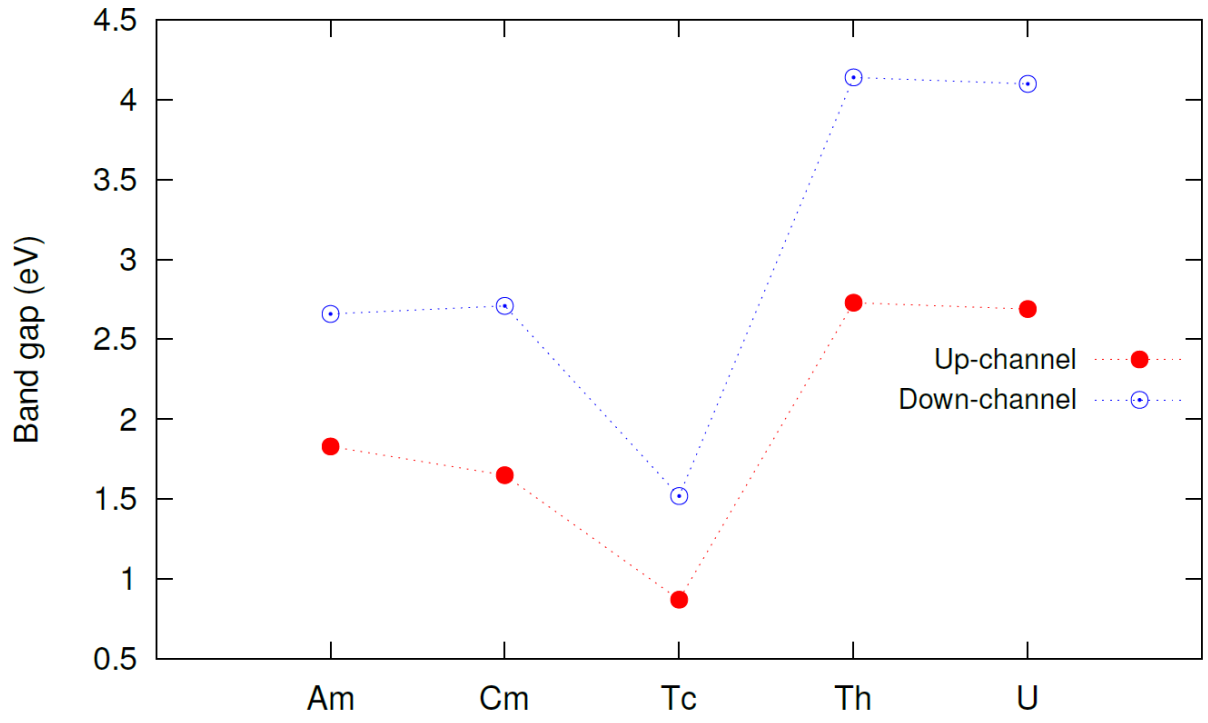

Figure 6-5. GGA+*U* calculated up-channel and down-channel band gaps of Am, Cm, Tc, and U substituted (position 1) U-8 MOF

All of the above results can be explained by analysis of the partial density of states (p-DOS). Since Zr-, and Th-MOFs have similar behavior, the p-DOS results are discussed only for the Th-MOF. Fig. 6-6 shows the p-DOS plot of Am substituted Th-MOF, with the zero of energy set to Fermi level. It can be seen that the HOMO and LUMO bands lie very close to each other in the up-channel, and thus results in a small gap of only 0.30 eV. The DOS near the HOMO is dominated by the O(2*p*) orbitals with a little hybridization from the Am(5*f*) orbitals. The LUMO is dominated by both the O(2*p*) and Am(5*f*) orbitals. Thus, the charge transfer can be considered to occur from the occupied O(2*p*) states to unoccupied Am(5*f*) states. By contrast, in the down-channel, the HOMO and LUMO bands are 3.5 eV apart. The down-channel HOMO band is also

dominated by the O(2*p*) orbitals, however, the LUMO band is dominated by the Th(5*f*) orbitals. Thus, the down-channel states are similar to the down-channel states of the pure Th-MOF. Moreover, the close to zero up-channel band gap and a wide down-channel band gap makes the Am substituted Th-MOF close to half-metallic in nature.

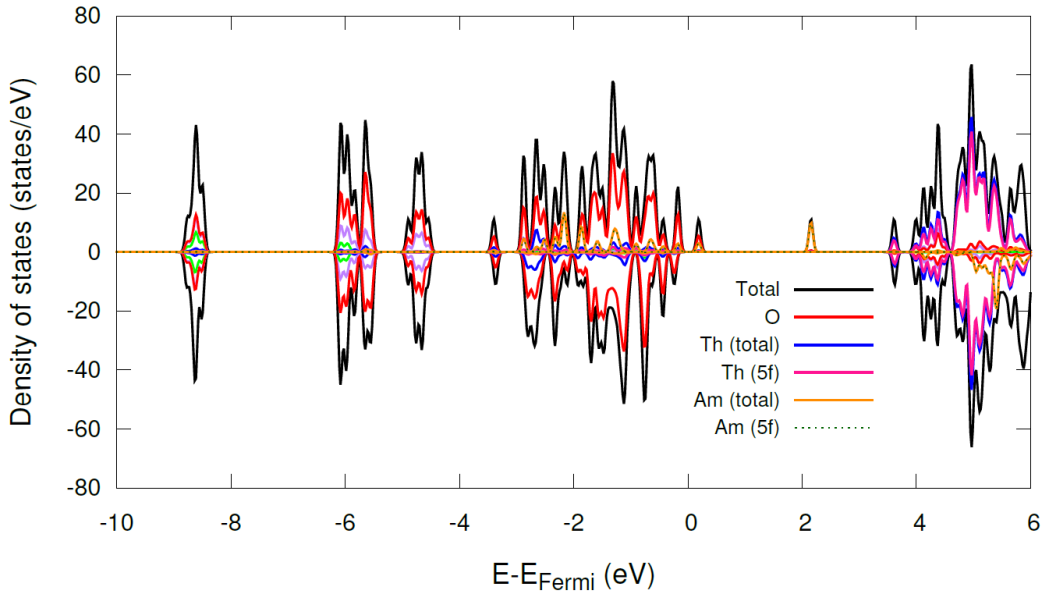

Figure 6-6. GGA+*U* calculated p-DOS of Am substituted (position 1) Th-8 MOF

Fig. 6-7 shows the p-DOS of Tc substituted Th-MOF. It can be seen that the HOMO bands which were dominated by the O(2*p*) orbitals in the pure Th-MOF, are now dominated by the Tc(4*d*) orbitals, in both the up-, and down-channels. Similarly, the LUMO bands which were dominated by the Th(5*f*) orbitals in the pure Th-MOF, are now dominated by Tc(4*d*) orbitals as well, and the Th(5*f*) orbitals now lie deep in the conduction bands.

Fig. 6-8 shows the p-DOS of U substituted Th-MOF. It can be seen that the both the HOMO and LUMO bands in the up-channel are dominated by U(5*f*) orbitals, which lowers the gap to 3.30 eV from 3.50 eV. The down-channel HOMO and LUMO bands are still dominated

by O(2*p*) and Th(5*f*) orbitals, as in the case of pure Th-MOF, and thus the down-channel band gap remains the same (3.50 eV).

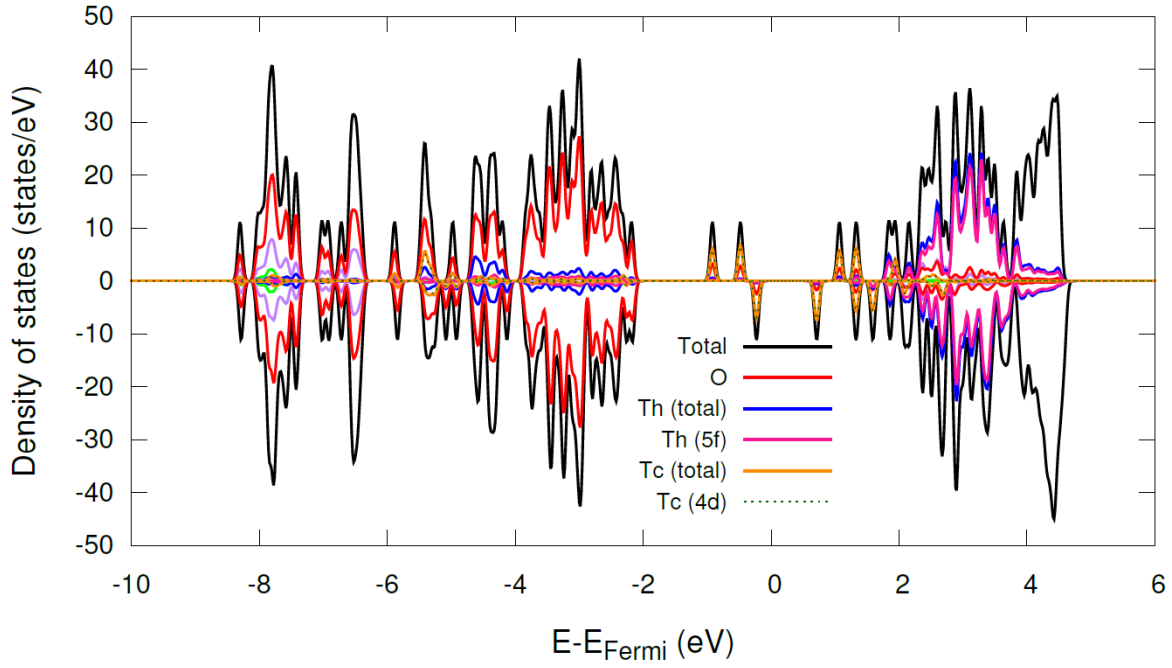

Figure 6-7. GGA+*U* calculated p-DOS of Tc substituted (position 1) Th-8 MOF

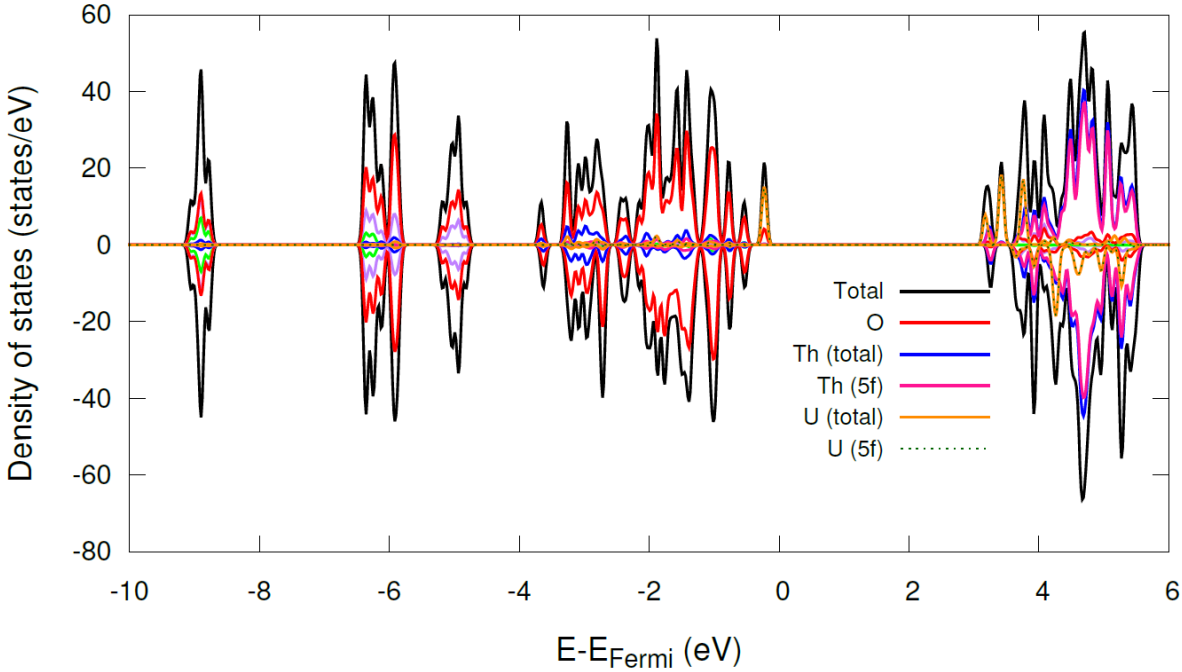

Figure 6-8. GGA+*U* calculated p-DOS of U substituted (position 1) Th-8 MOF

Fig. 6-9 shows the p-DOS of Am substituted U-MOF. It can be seen that there are two peaks near the Fermi level, in the up-channel state. The larger peak is composed of Am(5*f*) orbitals, while the smaller peak is dominated by U(5*f*) orbitals hybridized with O(2*p*) states. This is in contrast to the pure U-MOF, where the it's only the U(5*f*) orbitals dominating the HOMO band in the up-channel state. The LUMO band is still dominated by U(5*f*) orbitals as in the case of pure U-MOF. Mixing of Am(5*f*) and U(5*f*) states thus decreases the up-channel band gap of pure U-MOF from 2.69 to 1.83 eV. Whereas, the HOMO band in the down-channel state is dominated by Am(5*f*) orbitals with equal degree of hybridization with O(2*p*) orbitals. This is in contrast to the down-channel HOMO band of pure U-MOF which was dominated only by O(2*p*) states. The down-channel LUMO band is still dominated by U(5*f*) orbitals similar to the case of pure U-MOF. Thus, charge transfer in the Am substituted U-MOF would still occur from Metal5*f* to Metal5*f* transition as in the case of pure U-MOF, however, now with mixed state of Am(5*f*).

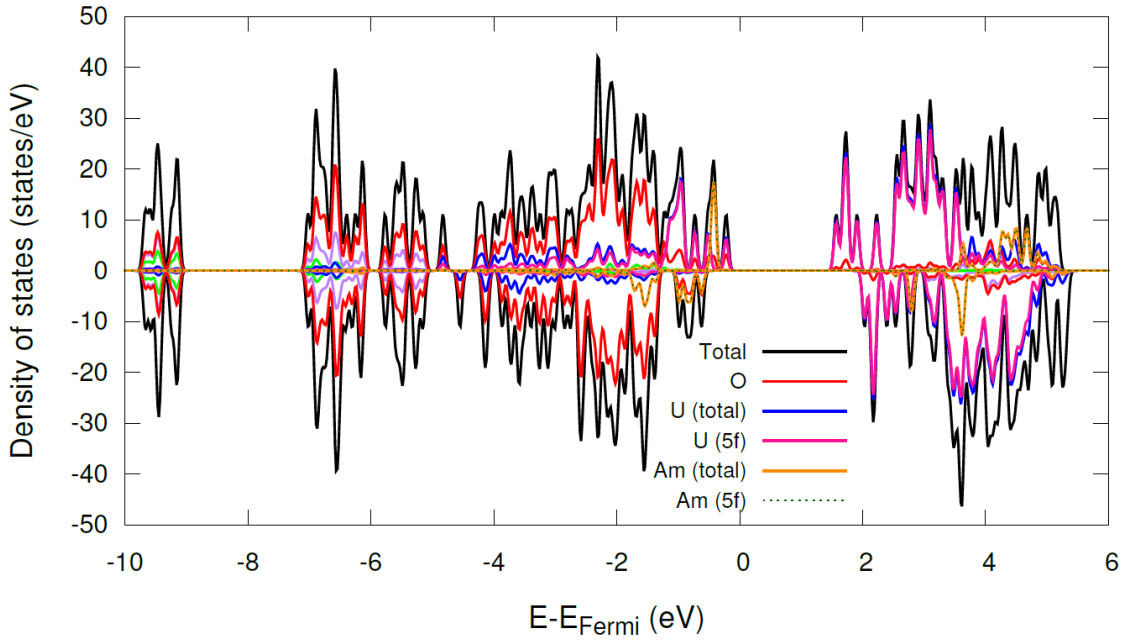

Figure 6-9. GGA+*U* calculated p-DOS of Am substituted (position 1) U-8 MOF

Fig. 6-10 shows the p-DOS of Tc substituted U-MOF. It can be seen that the up-channel HOMO and LUMO bands which were dominated by the U(5*f*) orbitals in the pure Th-MOF, are now dominated by the Tc(4*d*) orbitals. The U5*f* orbitals now lie deeper in the occupied and unoccupied states. Similarly, the down-channel HOMO and LUMO bands are now also dominated by Tc(4*d*) orbitals, which were dominated by O(2*p*) and U(5*f*) orbitals respectively, in the pure U-MOF.

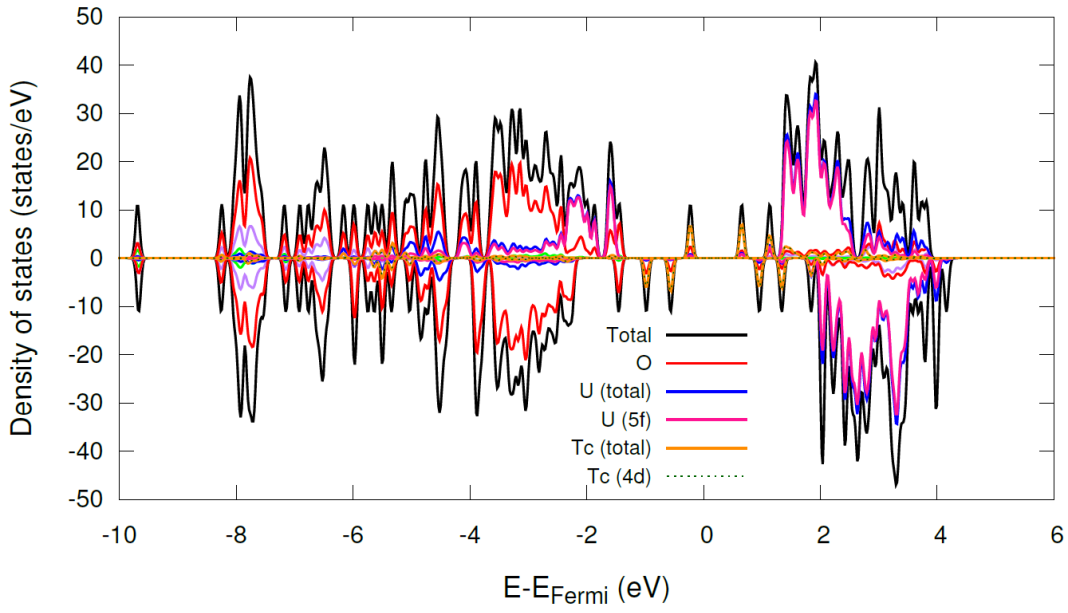

Figure 6-10. GGA+*U* calculated p-DOS of Tc substituted (position 1) U-8 MOF

Fig. 6-11 shows the p-DOS of Th substituted U-MOF. It can be seen that both the up-, and down-channel HOMO and LUMO edges are identical to the pure U-MOF. The up-channel HOMO and LUMO bands are both dominated by U(5*f*) orbitals. The down-channel HOMO band is dominated by O(2*p*) orbitals, while the LUMO band is dominated by U(5*f*) orbitals. This explains the no change in band gap of the U-MOF by Th substitution.

In summary, band gaps of Zr-, Th-, and U-MOFs can be modulated by substituting their metal atoms with Am, Cm, Tc, Th and U. The band gaps of the MOFs either decrease or remain

the same depending on the substituting species. Am and Cm lowers the band gaps of the Zr-, and Th-MOFs the most, followed by Tc and then U, while Th substitution has no effect on the band gap of the Zr-MOF. Tc substitution lowers the band gap of U-MOF the most, followed by Am and Cm, while Th substitution has no effect on the band gap.

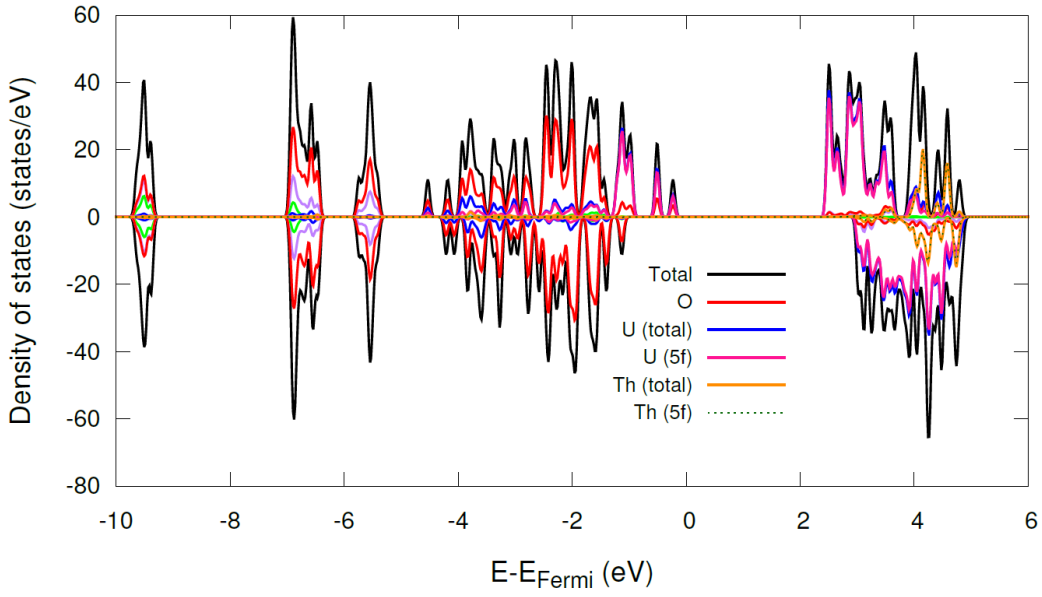

Figure 6-11. GGA+*U* calculated p-DOS of Tc substituted (position 1) U-8 MOF

6.3.2 Metal-Node Extension

Extending the metal-node of Th-MOF by a transition metal such as Co has experimentally been proven to decrease the band gap significantly and thus increasing the conductivity of the MOF [110]. This section explains the origin of the decrease in band gap using p-DOS analysis.

The band gap of Th-MOF was found to decrease from 3.50 eV to 2.0 eV with the extension of Th-metal node with cobalt. Moreover, non-magnetic Th-MOF becomes magnetic after Co-node extension, with a net magnetic moment of 12 μB. The majority of the magnetic moment is contributed by the 3*d* orbitals of Co atoms, having a local magnetic moment of 2.71

μB each. The reduction in band gap can be explained by the p-DOS as shown in Fig. 6-12. A *U*-*J*=4.0 eV was used for Co atoms to obtain consistent band gap with the experimental results of Ejegbavwo et al. [110], although a *U*-*J*=3.0 eV has been used in the previous literatures.

The up-channel and down-channel HOMO bands are found to be dominated by O(2*p*) orbitals hybridized with Co(3*d*) orbitals, in contrast to the Th-MOF without any node extension, where only O(2*p*) orbitals contribute to the HOMO bands. The LUMO bands however are still dominated by the Th(5*f*) orbitals as in the case of pure Th-MOF. The mixing of Co(3*d*) orbitals with the O(2*p*) orbitals in the HOMO bands thus causes the band gap to reduce by 1.5 eV.

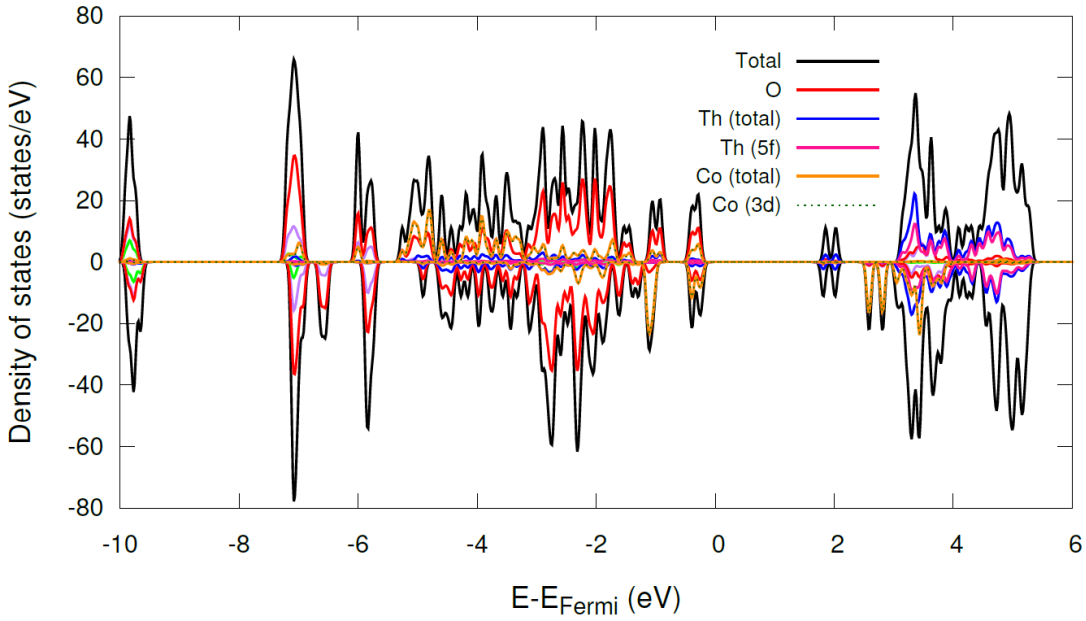

Figure 6-12. GGA+*U* calculated p-DOS of Th-Co-8 MOF

6.3.3 Choice of Linkers

This section describes the effect of linker on the band gap of a MOF. The Me_2BPDC^{2-} linker, as described in Chapter 5, has a high band gap of 3.80 eV. Such a high band gap of the linker only contributes to the insulating properties of the parent MOFs discussed in this work. The parent MOFs can either be doped or extended at the metal node with another metallic

species which can reduce the band gap of the MOF as described in the previous two sections. Another way of band gap modulation of a MOF is to install a linker having a band gap lower than the metal-node (SBU) itself. The experimental group of Shustova were experimentally able to install the linkers of Spiropyran and Merocyanine in the Th-MOF, which dramatically increased its conductivity (Shustova et al., private communication).

First, the two isolated linkers were modeled. The band gap of Spiropyran linker was found to be 1.95 eV, and that of the Merocyanine linker was found to be 1.55 eV. The lower band gap of the Merocyanine molecule than the Spiropyran molecule, despite the two molecules having same stoichiometry, reflects the conducting nature of Merocyanine molecule and the resistive nature of Spiropyran molecule. A truncated model of the extended MOF, with two Th-SBUs joined by Spiropyran or Merocyanine linkers (as shown previously in Section 6.2) were then modeled to investigate the effect of the linkers. The two Th-SBUs joined by a Spiropyran linker was found to have a band gap of 1.95 eV, which is identical to the band gap of isolated Spiropyran molecule. Similarly, the band gap of two Th-SBUs joined by a Merocyanine linker was found to be 1.55 eV which is identical to the band gap of isolated Merocyanine molecule. These results can be explained by the p-DOS analysis.

Fig. 6-13 shows the p-DOS of the two Th-SBUs joined by a Spiropyran linker and that of the isolated Spiropyran linker. It can be seen that the HOMO and LUMO band edges of both the models look identical. The HOMO band is dominated by the O(2*p*) and N(2*p*) orbitals and the LUMO band is dominated by H(1*s*) orbitals with hybridized N(2*p*) and O(2*p*) states. A zoomed-in version of the band edges is shown in Fig. 6-14(a).

Similarly, Fig. 6-15 shows the p-DOS of the two Th-SBUs joined by a Merocyanine linker and that of the isolated Merocyanine linker. It can be seen that the HOMO and LUMO

band edges of both the models look identical, as in the case of Spiropyran above. The HOMO band is dominated by the H(1*s*) and O(2*p*) orbitals and the LUMO band is dominated by O(2*p*) orbitals with hybridized N(2*p*) and H(1*s*) states. A zoomed-in version of the band edges is shown in Fig. 6-14(b).

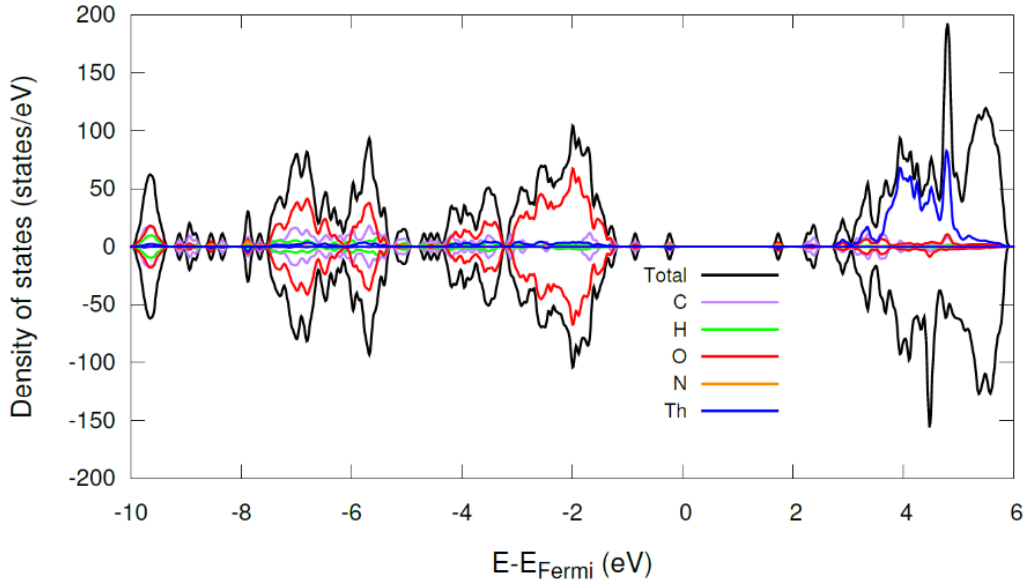

(a) SBUs+Spiropyran

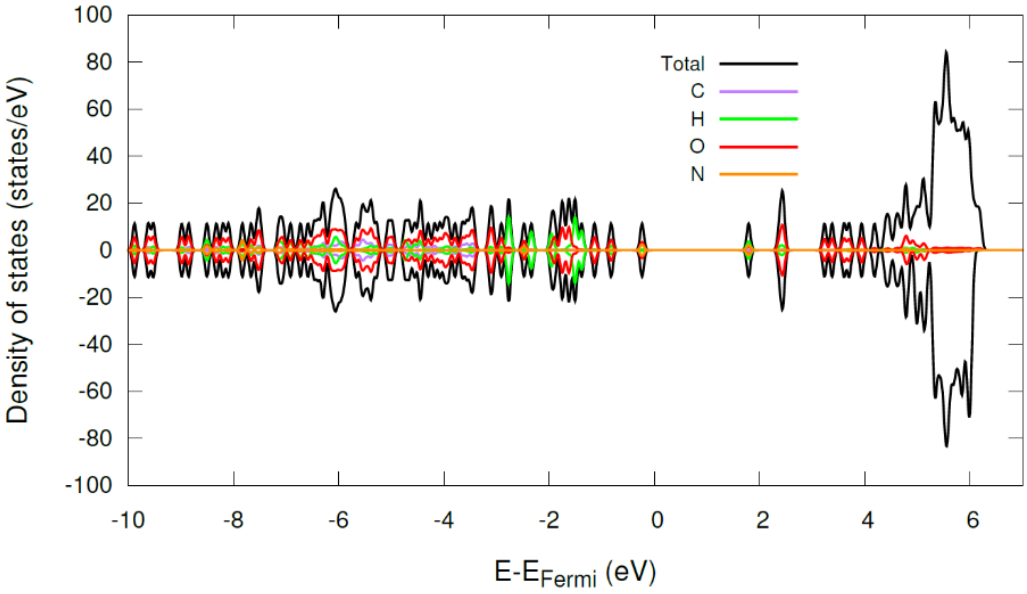

(b) Spiropyran

Figure 6-13. GGA-PBE calculated p-DOS of (a) two Th-SBUs joined by Spiropyran linker and (b) isolated Spiropyran linker

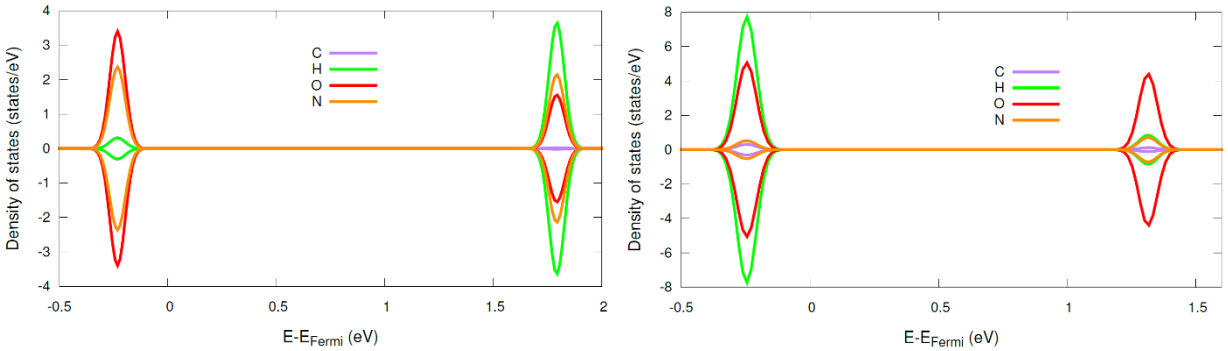

(a) Spiropyran (b) Merocyanine

Figure 6-14. Band edges of two Th-SBUs joined by (a) Spiropyran linker (b) Merocyanine linker

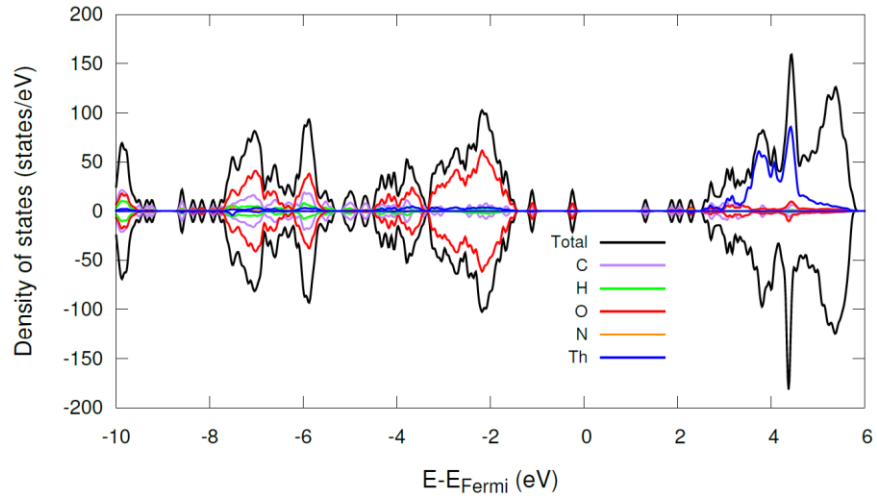

(a) SBUs+Merocyanine

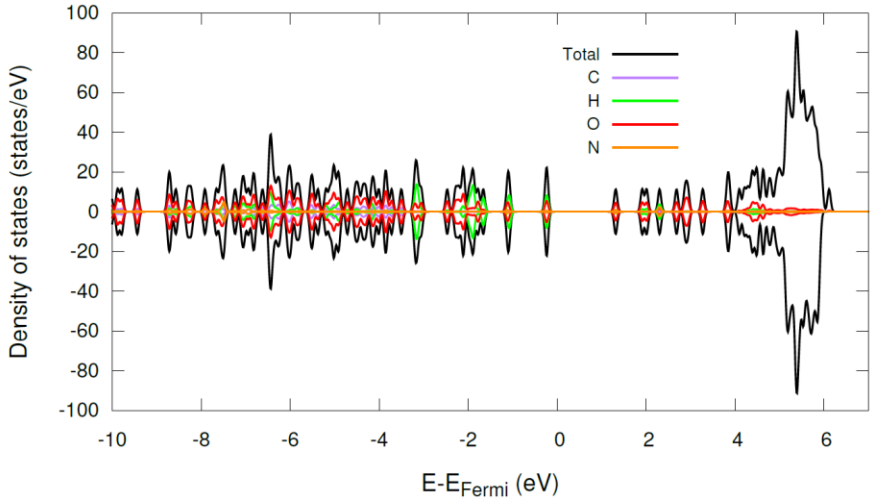

(b) Merocyanine

Figure 6-15. GGA-PBE calculated p-DOS of (a) two Th-SBUs joined by Merocyanine linker and (b) isolated Merocyanine linker

In no case the orbitals of Th metal lie near the band edges. Thus, the band gap is coming only from the oxygen, nitrogen, hydrogen and carbon atoms, of the linkers. Moreover, the lower band gap of the Merocyanine linker than the Spiropyran linker, is originating from the different band edges as shown in Fig. 6-14.

Thus, the band gap of a MOF can be modulated by installing linkers of different band gaps.

6.4 Conclusions

Three routes to band gap modulation in MOFs: (1) substitution of metal node; (2) metal-node extension; and (3) linker installation were investigated using DFT calculations. In particular, substitutions in Zr-, Th-, and U-MOFs with Am, Cm, Tc, Th and U were studied. Am, Cm and Tc were found to the reduce the band gaps of the all the MOFs the most, followed by U, while Th did not change the band gaps. Thus, assuming that accommodation of these second metals maintains the crystallinity of the MOF, conductivity of the MOFs can be significantly improved by transmetalation process, as also previously shown by Ejegbavwo et al. [110] for the transmetalation of Th-MOF with U ions. Doping with a secondary metal changes the density of states near the Fermi level, depending on the guest metal, and thus changes the band gap.

Extension of the metal node with a transition metal such as cobalt, can also drastically increase the conductivity of a MOF. The Th-MOF extended with Co lowers its band gap from 3.50 eV to 2.0 eV, thus changing the insulating Th-MOF to conducting, as also experimentally shown by Ejegbavwo et al. [110].

Another way of band gap modulation of a MOF without altering its metal node is to install appropriate linkers. It was shown that the Spiropyran and Merocyanine linkers having much lower band gaps than the insulating Me_2BPDC^{2-} linker, can reduce the band gap of Th-

MOF drastically. Moreover, the thermally reversible Spiropyran and Merocyanine linkers can function as molecular switches. It is also known that these two molecules are interconvertible by irradiation with visible light [170]. Thus, a MOF installed with such linkers can have potential applications of sensing, data-storage at the molecular-scale, and electronic signal modulation. These applications could be complementary to the primary use of these MOFs for nuclear waste storage as discussed in Chapter 5.

CHAPTER 7
SUMMARY AND FUTURE WORK

In Chapter 3, the fundamental thermodynamic and kinetic factors responsible for the evolution of Cu-Au alloys were investigated using DFT calculations. The question of the stability of the controversial $CuAu_3$ phase is answered, while the experimentally observed Cu_3Au and CuAu phases are confirmed by convex-hull calculations. A thorough investigation of the numerous phases lying close to the hull in the Au-rich region was done. The Cu rich phases were found to be more stable as L_{12} type structures, which have planes of mixed Cu and Au atoms separated by planes of pure Cu atoms, while the Au rich phases were found to be more stable as the L_{10} type structures, which have alternate planes of Cu and Au atoms. This is because of the high strain caused to the smaller Cu atoms when their planes are placed in the L_{10} configuration. By contrast, the bigger Au atoms and smaller Cu atoms can easily be placed in the L_{10} configuration without any strain penalties in the Au-rich domain of the convex-hull. The numerous Au-rich phases lying close to the hull were found to be superstructures of the L_{10} phase and lie above the hull by only <3 meV. Thus, these phases are likely to be manifested in the experiments as the room temperature corresponds to 25 meV.

The work in Chapter 3 also investigated the effects of epitaxy on the ordered Cu-Au alloys when the underlying substrate is Au. The Cu rich phases were found to destabilize when grown epitaxially on the Au substrate, while the Au rich phases maintain their stability depending on the growth plane. These results confirm the experimental observations of (1) nucleation of Au rich alloy concurrently with the reduction of Cu_2O to metallic Cu independent of the Cu content of the system and (2) selective etching of Cu from the Cu-Au matrices.

Chapter 3 also investigated the kinetics in ordered and disordered Cu-Au alloys, in terms of activation energies of diffusion and minimum energy paths. The unequal rates of diffusion in

intermetallic matrices, i.e., the Kirkendall effect is indicated by the lower activation energies for diffusion of Cu than for Au, in both the L_{12} and L_{10} phases. The higher vacancy formation energies of Au atoms lead to higher activation barriers for Au diffusion than for Cu, despite of lower migration barriers of Au vacancies because more thermal energy is required to form Au vacancies than Cu vacancies. It was found that both the Au and Cu vacancies prefer a Au rich environment in the disordered alloy, with the vacancy formation energy of Au higher than that of Cu in any given local environment. The activation energies of both Cu and Au diffusion show a normal distribution in the disordered alloy, which can be attributed to the non-distinguishable self-diffusion and anti-site diffusion of the species in disordered alloys. However, the migration barriers show a wide distribution with different local environments of vacancies.

Future work motivated by the work in Chapter 3 could be investigation of thermodynamics and kinetics in the core-shell structures of Cu-Au, which do not have any mixing of species. The thermodynamic parameters such as, work of adhesion and interfacial energies could be modeled to understand the effects of epitaxy. Moreover, appropriate minimum energy paths could be identified, and migration barriers could be modeled across the Cu-Au interface.

In Chapter 4, the thermodynamics of ion-exchange in the MOFs was investigated for the purpose of radionuclide sequestration. In particular, the substitution energies of Am, Cm, Tc, Th, and U were calculated in the Zr-, Th-, and U-MOFs at the metal-nodes, using various DFT methods. The favorability of ion-exchange was found to be robust with different flavors of XC-functionals (GGA→metaGGA→hybrids), vdW corrections, DFT+*U* corrections, spin-polarization, and relativistic effects using spin-orbit coupling. It was concluded that GGA-PBE level of theory without any of the sophisticated DFT methods like DFT+*U*, spin-polarization,

vdW, and SOC is sufficient to establish the preference of ion-exchange at the metal node in MOFs. Reference states of the ions participating in the ion-exchange process was found to be critical in determining the substitution energies. Three different reference states, (1) vacuum, (2) continuum water medium, and (3) explicit water molecules were investigated to calculate the substitution energies. The explicit water molecules were found to give the most reasonable values for the substitution energies, the magnitudes for which were highly overestimated by vacuum and continuum water media as reference states. It was also found that the SBUs of a MOF are sufficient truncated structures to model the ion-exchange process in MOFs at the metal-nodes.

Tc, Am, and Cm substitutions were found to be energetically favorable in all the MOFs. U substitution was found to be favorable in the Zr-8 MOF, but unfavorable in the Th-MOFs. Th substitution was found to be favorable in both Zr-, and U-MOFs. The favorable Th substitution in U-MOF and unfavorable U substitution in the Th-MOF were found to be consistent with the transmetalation reactions performed by Ejegbavwo et al. [110].

The work done in Chapter 4 can thus prove to be a benchmark for future DFT calculations of ion-exchange in MOFs. This work can also guide the experiments on choosing the radionuclides for transmetalation and thus optimizing time and resources involved in dealing with such toxic radionuclides. The ion-exchange in MOFs can also serve as an alternative to the traditional methods of plutonium uranium redox extraction (PUREX), anion-exchange resins, and solvent-extraction processes which suffer from the drawbacks of the use of volatile diluents, high radiation doses, low sorption capacity, and slow kinetics.

Future work motivated by work done in Chapter 4 could be exploring different solvents for the ion-exchange process other than water. *N*,*N*′-dimethylformadide (DMF) is a common

organic solvent used for synthesis of MOFs. Moreover, the pores of the MOFs could be utilized too to contain the radionuclides, other than their metal nodes. Binding energy calculation of the radionuclides with the pores could be done to determine the favorability of sequestration.

In Chapter 5, electronic structures of Zr-, Th-, and U-MOFs were systematically investigated using DFT calculations. Various DFT methods including, different XC-functionals, DFT+*U*, spin-polarization, and SOC were used to determine the robustness in band gaps and electronic density of states of the MOFs. The band gaps and DOSs of the Zr-, and Th-MOFs were found to be robust with DFT+*U* and spin-polarization, while the electronic structures of all three MOFs were found to be robust with SOC. The band gap and DOS of U-MOF was found to be sensitive to DFT+*U* and spin, as expected. The Zr-, and Th-MOFs were found to have a high band gaps in the range of 3.50-4.0 eV and thus have insulating properties. The DOS of Zr-, and Th-MOFs reveals that the HOMO and LUMO band edges are dominated by Zr(4*d*) and Th(4*f*), and O(2*p*) orbitals respectively. By contrast, the U-MOF was found to have a lower band gap of 2.69 eV, using the *U*-*J*=4.0 eV which was initially fitted for UO_2.

The U-MOF was found to show 10 different spin-orientations, based on relative spins of the six metal ions. All the configurations were characterized for their relative energies with respect to the ferromagnetic state and band gaps, using GGA+*U* and SCAN+*U* XC-functionals. For 8 out of 9 configurations both the GGA and SCAN functionals make same predictions for their relative stabilities with respect to the FM state. The SCAN functional is known to overestimate the magnetic energies and thus GGA-PBE results can be considered to be more reliable. However, the GGA+*U* and SCAN+*U* XC-functionals were found to be robust for the band gaps of all the 10 configurations.

Chapter 5 also identifies the origin of band gap in a MOF. It was found that the metal-node (SBU) or the organic linker, whichever has the lower band gap determines the band gap of the MOF. These results were further confirmed by the DOS results which indicate that either the functional groups of the organic linker or the metal-nodes contribute to the band edges. This identification of the origin of the band gap can guide the experiments in modulating the electronic structures of a MOF by installing linkers or metal-nodes of desired conductivities.

Chapter 5 also compared the GGA, metaGGA-SCAN and hybrid (HSE and B3LYP) functionals for the band gaps of the MOFs. It was found that, the SCAN and hybrid functionals highly overestimate the band gaps of the Zr-, and Th-MOFs. The GGA-PBE functionals was found to produce accurate band gaps of the Zr-, and Th-MOFs with respect to the experiments. By contrast, the all the XC-functionals were found to give band gaps within 11% with respect to the GGA+*U* functional, for the U-MOF.

Future work motivated by Chapter 5 could be to further explore the 14 magnetic states of the U-MOF, to construct an Ising-like model. The exchange coupling constants for interactions between different metal sites could be extracted to verify the accuracy of the DFT calculations. The problem of SCAN XC-functional overestimating the magnetic energies could be further addressed by making improvements to the functional. Moreover, appropriate *U-J* values for SCAN functional which does not exist for the actinides, could be fitted.

In Chapter 6, three different ways to engineer the band gaps of a MOF were investigated: (1) substitution at metal-node (2) metal-node extension and (3) choice of linker. The substitutions in Zr-, Th-, and U-MOFs were carried out using Am, Cm, Th, U, and Tc. It was found that Am, Cm, and Tc lower the band gaps of these MOFs the most, followed by U, while Th does not change the band gaps. The DOS analysis showed that Am and Cm substituted Zr-,

and Th-MOFs are half-metallic in nature. The half-metals could potentially be used in spintronics and energy conversion applications [173,174]. They might also be suitable materials to manufacture electrodes to be used in magnetic tunnel junctions and to inject spin-polarized currents into semiconductors [175–177]. Thus, the Zr-, and Th-MOFs could find applications in the semiconductor industry, complementing to the primary application of radionuclide sequestration considered in this work.

Another way of band gap modulation discussed in Chapter 6 is metal-node extension. Metal-node extension of the Th-MOF with cobalt ions was found to dramatically decrease the band gap to 2.0 eV from 3.50 eV, thereby increasing the conductivity.

Chapter 6 also investigated the effect of linker on the electronic density of states. It was found that, just by installing a linker of desired band gap alone can modify the band gap of the entire MOF, without introduction of a second metal in the MOF. The Spiropyran and Merocyanine linkers joining the SBUs were investigated for their band gaps and DOS. The two linkers are known to be structural isomers of each other and thermally reversible. The conductive nature of the Merocyanine linker over resistive Spiropyran linker was confirmed by lower and gap of the Merocyanine linker. The band gaps of the SBUs joined by these linkers were found to be determined by the linkers, as the linkers have band gaps lower band gap than any of the MOF-SBU considered in this work.

LIST OF REFERENCES

[1] G. Makov, C. Gattinoni, A. De Vita, Ab initio based multiscale modelling for materials science, Model. Simul. Mater. Sci. Eng. 17 (2009). doi:10.1088/0965-0393/17/8/084008.

[2] J.A. Elliott, Novel approaches to multiscale modelling in materials science, Int. Mater. Rev. 56 (2011) 207–225. doi:10.1179/1743280410Y.0000000002.

[3] C. Corkhill, N. Hyatt, Nuclear Waste Management, 2018. doi:10.1088/978-0-7503-1638-5.

[4] S.K. Ghosh, Metal-Organic Frameworks (MOFs) for Environmental Applications, 2019. doi:10.1016/c2017-0-01721-4.

[5] M.J. Hudson, L.M. Harwood, D.M. Laventine, F.W. Lewis, Use of soft heterocyclic N-donor ligands to separate actinides and lanthanides, Inorg. Chem. 52 (2013) 3414–3428. doi:10.1021/ic3008848.

[6] C.L. Xiao, Q.Y. Wu, C.Z. Wang, Y.L. Zhao, Z.F. Chai, W.Q. Shi, Quantum chemistry study of uranium(VI), neptunium(V), and plutonium(IV,VI) complexes with preorganized tetradentate phenanthrolineamide ligands, Inorg. Chem. 53 (2014) 10846–10853. doi:10.1021/ic500816z.

[7] A. Leoncini, J. Huskens, W. Verboom, Ligands for f-element extraction used in the nuclear fuel cycle, Chem. Soc. Rev. 46 (2017) 7229–7273. doi:10.1039/c7cs00574a.

[8] J.O. Blomeke, A.G. Croff, Nuclear Waste Partitioning and Transmutation, Nucl. Technol. 56 (1982) 361–371. doi:https://doi.org/10.13182/NT82-A32864.

[9] C. Xiao, A. Zhang, Z. Chai, Synthesis and characterization of novel macroporous silica-polymer-calixcrown hybrid supramolecular recognition materials for effective separation of cesium, J. Hazard. Mater. 267 (2014) 109–118. doi:10.1016/j.jhazmat.2013.12.048.

[10] C. Xiao, A. Zhang, Z. Chai, Synthesis and characterization of a novel organic-inorganic hybrid supramolecular recognition material and its selective adsorption for cesium, J. Radioanal. Nucl. Chem. 299 (2014) 699–708. doi:10.1007/s10967-013-2798-y.

[11] B. Gu, G.M. Brown, P. V. Bonnesen, L. Liang, B.A. Moyer, R. Ober, S.D. Alexandratos, Development of novel bifunctional anion-exchange resins with improved selectivity for pertechnetate sorption from contaminated groundwater, Environ. Sci. Technol. 34 (2000) 1075–1080. doi:10.1021/es990951g.

[12] J.L.C. Rowsell, O.M. Yaghi, Metal-organic frameworks: A new class of porous materials, Microporous Mesoporous Mater. 73 (2004) 3–14. doi:10.1016/j.micromeso.2004.03.034.

[13] H. Furukawa, K.E. Cordova, M. O'Keeffe, O.M. Yaghi, The chemistry and applications of metal-organic frameworks, Science (80-.). 341 (2013). doi:10.1126/science.1230444.

[14] H. Wang, W.P. Lustig, J. Li, Sensing and capture of toxic and hazardous gases and vapors by metal-organic frameworks, Chem. Soc. Rev. 47 (2018) 4729–4756. doi:10.1039/c7cs00885f.

[15] J.R. Li, J. Sculley, H.C. Zhou, Metal-organic frameworks for separations, Chem. Rev. 112 (2012) 869–932. doi:10.1021/cr200190s.

[16] S.T. Meek, J.A. Greathouse, M.D. Allendorf, Metal-organic frameworks: A rapidly growing class of versatile nanoporous materials, Adv. Mater. 23 (2011) 249–267. doi:10.1002/adma.201002854.

[17] P. Kumar, A. Pournara, K.H. Kim, V. Bansal, S. Rapti, M.J. Manos, Metal-organic frameworks: Challenges and opportunities for ion-exchange/sorption applications, Prog. Mater. Sci. 86 (2017) 25–74. doi:10.1016/j.pmatsci.2017.01.002.

[18] E.A. Dolgopolova, A.M. Rice, N.B. Shustova, Actinide-based MOFs: A middle ground in solution and solid-state structural motifs, Chem. Commun. 54 (2018) 6472–6483. doi:10.1039/c7cc09780h.

[19] J. Li, X. Wang, G. Zhao, C. Chen, Z. Chai, A. Alsaedi, T. Hayat, X. Wang, Metal-organic framework-based materials: Superior adsorbents for the capture of toxic and radioactive metal ions, Chem. Soc. Rev. 47 (2018) 2322–2356. doi:10.1039/c7cs00543a.

[20] M. Mon, R. Bruno, J. Ferrando-Soria, D. Armentano, E. Pardo, Metal-organic framework technologies for water remediation: Towards a sustainable ecosystem, J. Mater. Chem. A. 6 (2018) 4912–4947. doi:10.1039/c8ta00264a.

[21] S. Horike, S. Shimomura, S. Kitagawa, Soft porous crystals, Nat. Chem. 1 (2009) 695–704. doi:10.1038/nchem.444.

[22] J. Yang, W. Zhu, W. Qu, Z. Yang, J. Wang, M. Zhang, H. Li, Selenium Functionalized Metal-Organic Framework MIL-101 for Efficient and Permanent Sequestration of Mercury, Environ. Sci. Technol. 53 (2019) 2260–2268. doi:10.1021/acs.est.8b06321.

[23] Y. Zhao, H. Wu, T.J. Emge, Q. Gong, N. Nijem, Y.J. Chabal, L. Kong, D.C. Langreth, H. Liu, H. Zeng, J. Li, Enhancing gas adsorption and separation capacity through ligand functionalization of microporous metal-organic framework structures, Chem. - A Eur. J. 17 (2011) 5101–5109. doi:10.1002/chem.201002818.

[24] Y. Yue, R.T. Mayes, J. Kim, P.F. Fulvio, X.G. Sun, C. Tsouris, J. Chen, S. Brown, S. Dai, Seawater uranium sorbents: Preparation from a mesoporous copolymer initiator by atom-transfer radical polymerization, Angew. Chemie - Int. Ed. 52 (2013) 13458–13462. doi:10.1002/anie.201307825.

[25] L. Zhou, M. Bosscher, C. Zhang, S. Özçubukçu, L. Zhang, W. Zhang, C.J. Li, J. Liu, M.P. Jensen, L. Lai, C. He, A protein engineered to bind uranyl selectively and with femtomolar affinity, Nat. Chem. 6 (2014) 236–241. doi:10.1038/nchem.1856.

[26] M. Carboni, C.W. Abney, S. Liu, W. Lin, Highly porous and stable metal-organic frameworks for uranium extraction, Chem. Sci. 4 (2013) 2396–2402. doi:10.1039/c3sc50230a.

[27] N. Zhang, L.Y. Yuan, W.L. Guo, S.Z. Luo, Z.F. Chai, W.Q. Shi, Extending the Use of Highly Porous and Functionalized MOFs to Th(IV) Capture, ACS Appl. Mater. Interfaces. 9 (2017) 25216–25224. doi:10.1021/acsami.7b04192.

[28] D. Banerjee, D. Kim, M.J. Schweiger, A.A. Kruger, P.K. Thallapally, Removal of TcO4- ions from solution: Materials and future outlook, Chem. Soc. Rev. 45 (2016) 2724–2739. doi:10.1039/c5cs00330j.

[29] H. Fei, M.R. Bresler, S.R.J. Oliver, A new paradigm for anion trapping in high capacity and selectivity: Crystal-to-crystal transformation of cationic materials, J. Am. Chem. Soc. 133 (2011) 11110–11113. doi:10.1021/ja204577p.

[30] C. Gao, Y. Hu, M. Wang, M. Chi, Y. Yin, Fully alloyed Ag/Au nanospheres: Combining the plasmonic property of Ag with the stability of Au, J. Am. Chem. Soc. 136 (2014) 7474–7479. doi:10.1021/ja502890c.

[31] G.G. Li, D.A. Blom, S. Pandey, R.J. Koch, S.T. Misture, S.R. Phillpot, H. Wang, Overcoming the Interfacial Lattice Mismatch: Geometry Control of Gold–Nickel Bimetallic Heteronanostructures, Part. Part. Syst. Charact. 35 (2018) 1–7. doi:10.1002/ppsc.201700361.

[32] G.G. Li, E. Villarreal, Q. Zhang, T. Zheng, J.J. Zhu, H. Wang, Controlled Dealloying of Alloy Nanoparticles toward Optimization of Electrocatalysis on Spongy Metallic Nanoframes, ACS Appl. Mater. Interfaces. 8 (2016) 23920–23931. doi:10.1021/acsami.6b07309.

[33] K.D. Gilroy, A. Ruditskiy, H.C. Peng, D. Qin, Y. Xia, Bimetallic nanocrystals: Syntheses, properties, and applications, Chem. Rev. 116 (2016) 10414–10472. doi:10.1021/acs.chemrev.6b00211.

[34] Y. Yan, J.S. Du, K.D. Gilroy, D. Yang, Y. Xia, H. Zhang, Intermetallic Nanocrystals : Syntheses and Catalytic Applications, (2017). doi:10.1002/adma.201605997.

[35] H.C. Zur Loye, T. Besmann, J. Amoroso, K. Brinkman, A. Grandjean, C.H. Henager, S. Hu, S.T. Misture, S.R. Phillpot, N.B. Shustova, H. Wang, R.J. Koch, G. Morrison, E. Dolgopolova, Hierarchical Materials as Tailored Nuclear Waste Forms: A Perspective, Chem. Mater. 30 (2018) 4475–4488. doi:10.1021/acs.chemmater.8b00766.

[36] W. Chen, R. Yu, L. Li, A. Wang, Q. Peng, Y. Li, A seed-based diffusion route to monodisperse intermetallic CuAu nanocrystals, Angew. Chemie - Int. Ed. 49 (2010) 2917–2921. doi:10.1002/anie.200906835.

[37] A.K. Sra, R.E. Schaak, Synthesis of atomically ordered AuCu and AuCu3 nanocrystals from bimetallic nanoparticle precursors, J. Am. Chem. Soc. 126 (2004) 6667–6672. doi:10.1021/ja031547r.

[38] M. Born, R. Oppenheimer, Zur Quantentheorie der Molekeln, Ann. Phys. 389 (1927) 457–484. doi:10.1002/andp.19273892002.

[39] P. Hohenberg, W. Kohn, Inhomogeneous Electron Gas*, Phys. Rev. 136 (1964) 864–871. doi:https://doi.org/10.1103/PhysRev.136.B864.

[40] W. Kohn, L.J. Sham, Self-Consistent Equations Including Exchange and Correlation Effects*, Phys. Rev. 140 (1965) A1133-1138. doi:https://doi.org/10.1103/PhysRev.140.A1133.

[41] J.P. Perdew, K. Burke, M. Ernzerhof, Generalized gradient approximation made simple, Phys. Rev. Lett. 77 (1996) 3865–3868. doi:10.1103/PhysRevLett.77.3865.

[42] J. Tao, J.P. Perdew, V.N. Staroverov, G.E. Scuseria, Climbing the density functional ladder: Nonempirical meta–generalized gradient approximation designed for molecules and solids, Phys. Rev. Lett. 91 (2003) 3–6. doi:10.1103/PhysRevLett.91.146401.

[43] J. Sun, R.C. Remsing, Y. Zhang, Z. Sun, A. Ruzsinszky, H. Peng, Z. Yang, A. Paul, U. Waghmare, X. Wu, M.L. Klein, J.P. Perdew, Accurate first-principles structures and energies of diversely bonded systems from an efficient density functional, Nat. Chem. 8 (2016) 831–836. doi:10.1038/nchem.2535.

[44] E.B. Isaacs, C. Wolverton, Performance of the strongly constrained and appropriately normed density functional for solid-state materials, Phys. Rev. Mater. 2 (2018) 1–11. doi:10.1103/PhysRevMaterials.2.063801.

[45] S. Kurth, J.P. Perdew, P. Blaha, Molecular and solid-state tests of density functional approximations: LSD, GGAs, and Meta-GGAs, Int. J. Quantum Chem. 75 (1999) 889–909. doi:10.1002/(SICI)1097-461X(1999)75:4/5<889::AID-QUA54>3.0.CO;2-8.

[46] R. Ahlrichs, F. Furche, S. Grimme, Comment on “assessment of exchange correlation functionals” [A.J. Cohen, N.C. Handy, Chem. Phys. Lett. 316 (2000) 160-166], Chem. Phys. Lett. 325 (2000) 317–321. doi:10.1016/S0009-2614(00)00654-0.

[47] J.P. Perdew, Y. Wang, Accurate and simple analytic representation of the electron-gas correlation energy, Phys. Rev. B. 45 (1992) 244–249. doi:https://doi.org/10.1103/PhysRevB.45.13244.

[48] J.P. Perdew, W. Yue, Accurate and simple density functional for the electronic exchange energy: Generalized gradient approximation, Phys. Rev. B. 33 (1986) 8800–8802. doi:10.1103/PhysRevB.33.8800.

[49] J.P. Perdew, K. Burke, Y. Wang, Generalized gradient approximation for the exchange-correlation hole of a many-electron system, Phys. Rev. B. 54 (1996) 533–539. doi:https://doi.org/10.1103/PhysRevB.54.16533.

[50] J.P. Perdew, K. Burke, M. Ernzerhof, Perdew, Burke, and Ernzerhof Reply, Phys. Rev. Lett. 80 (1998) 891. doi:10.1103/PhysRevLett.80.891.

[51] R. Armiento, A.E. Mattsson, Functional designed to include surface effects in self-consistent density functional theory, Phys. Rev. B - Condens. Matter Mater. Phys. 72 (2005) 1–5. doi:10.1103/PhysRevB.72.085108.

[52] A.E. Mattsson, R. Armiento, J. Paier, G. Kresse, J.M. Wills, T.R. Mattsson, The AM05 density functional applied to solids, J. Chem. Phys. 128 (2008). doi:10.1063/1.2835596.

[53] J. Sun, J.P. Perdew, A. Ruzsinszky, Semilocal density functional obeying a strongly tightened bound for exchange, Proc. Natl. Acad. Sci. U. S. A. 112 (2015) 685–689. doi:10.1073/pnas.1423145112.

[54] J. Sun, B. Xiao, A. Ruzsinszky, Communication: Effect of the orbital-overlap dependence in the meta generalized gradient approximation, J. Chem. Phys. 137 (2012). doi:10.1063/1.4742312.

[55] J. Sun, A. Ruzsinszky, J. Perdew, Strongly Constrained and Appropriately Normed Semilocal Density Functional, Phys. Rev. Lett. 115 (2015) 1–6. doi:10.1103/PhysRevLett.115.036402.

[56] Y. Zhao, D.G. Truhlar, A new local density functional for main-group thermochemistry, transition metal bonding, thermochemical kinetics, and noncovalent interactions, J. Chem. Phys. 125 (2006). doi:10.1063/1.2370993.

[57] J.P. Perdew, A. Ruzsinszky, J. Sun, K. Burke, Gedanken densities and exact constraints in density functional theory, J. Chem. Phys. 140 (2014) 18A533. doi:10.1063/1.4870763.

[58] J. Heyd, G.E. Scuseria, M. Ernzerhof, Erratum: Hybrid functionals based on a screened Coulomb potential (Journal of Chemical Physics (2003) 118 (8207)), J. Chem. Phys. 124 (2006) 2005–2006. doi:10.1063/1.2204597.

[59] A. V. Krukau, O.A. Vydrov, A.F. Izmaylov, G.E. Scuseria, Influence of the exchange screening parameter on the performance of screened hybrid functionals, J. Chem. Phys. 125 (2006). doi:10.1063/1.2404663.

[60] A.D. Becke, Density-functional thermochemistry. III. The role of exact exchange, J. Chem. Phys. 98 (1993) 5648–5652. doi:10.1063/1.464913.

[61] J. Paier, R. Hirschl, M. Marsman, G. Kresse, The Perdew-Burke-Ernzerhof exchange-correlation functional applied to the G2-1 test set using a plane-wave basis set, J. Chem. Phys. 122 (2005) 0–13. doi:10.1063/1.1926272.

[62] T. Petit, B. Morel, C. Lemaignan, A. Pasturel, B. Bigot, Cohesive properties of UO2, Philos. Mag. B. 73 (1996) 893–904. doi:doi.org/10.1080/01418639608240321.

[63] S.L. Dudarev, M.R. Castell, G.A. Botton, S.Y. Savrasov, C. Muggelberg, G.A.D. Briggs, A.P. Sutton, D.T. Goddard, Understanding STM images and EELS spectra of oxides with strongly correlated electrons: A comparison of nickel and uranium oxides, Micron. 31 (2000) 363–372. doi:10.1016/S0968-4328(99)00115-8.

[64] S.L. Dudarev, G.A. Botton, S.Y. Savrasov, C.J. Humphreys, A.P. Sutton, Electron-energy-loss spectra and the structural stability of nickel oxide: An LSDA+U study, Phys. Rev. B. 57 (1998) 1505–1509. doi:https://doi.org/10.1103/PhysRevB.57.1505.

[65] J.C. Slater, Atomic shielding constants, Phys. Rev. 36 (1930) 57–64. doi:10.1103/PhysRev.36.57.

[66] S.F. Boys, A General Method of Calculation for the Stationary States of Any Molecular System, Proc. R. Soc. Lond. A. Math. Phys. Sci. 200 (1950) 542–554.

[67] F. Jensen, Atomic orbital basis sets, Wiley Interdiscip. Rev. Comput. Mol. Sci. 3 (2013) 273–295. doi:10.1002/wcms.1123.

[68] P.E. Blöchl, Projector augmented-wave method, Phys. Rev. B. 50 (1994) 17953–17979. doi:10.1103/PhysRevB.50.17953.

[69] S. Steiner, S. Khmelevskyi, M. Marsmann, G. Kresse, Calculation of the magnetic anisotropy with projected-augmented-wave methodology and the case study of disordered Fe1-xCox alloys, Phys. Rev. B. 93 (2016) 224425. doi:10.1103/PhysRevB.93.224425.

[70] E. Van Lenthe, R. Van Leeuwen, E.J. Baerends, J.G. Snijders, Relativistic regular two-component hamiltonians, Int. J. Quantum Chem. 57 (1996) 281–293. doi:10.1002/(SICI)1097-461X(1996)57:3<281::AID-QUA2>3.0.CO;2-U.

[71] D. Hobbs, G. Kresse, J. Hafner, Fully unconstrained noncollinear magnetism within the projector augmented-wave method, Phys. Rev. B - Condens. Matter Mater. Phys. 62 (2000) 11556–11570. doi:10.1103/PhysRevB.62.11556.

[72] A. Zunger, S. Wei, L.G. Ferreira, J.E. Bernard, Special quasirandom structures, Phys. Rev. Lett. 65 (1990) 353–356. doi:https://doi.org/10.1103/PhysRevLett.65.353.

[73] A. Van De Walle, P. Tiwary, M. De Jong, D.L. Olmsted, M. Asta, A. Dick, D. Shin, Y. Wang, L. Chen, Z. Liu, M. Carlo, CALPHAD : Computer Coupling of Phase Diagrams and Thermochemistry Ef fi cient stochastic generation of special quasirandom structures, Calphad. 42 (2013) 13–18. doi:10.1016/j.calphad.2013.06.006.

[74] Y. Sun, Y. Xia, M.J. Science, Mechanistic Study on the Replacement Reaction between Silver Nanostructures and Chloroauric Acid in Aqueous Medium, (2004) 3892–3901. doi:10.1021/ja039734c.

[75] E. Gonzalez, J. Arbiol, V.F. Puntes, Carving at the Nanoscale : Sequential, Science (80-.). 334 (2011) 1377–1381. doi:10.1126/science.1212822.

[76] A.K. Sra, T.D. Ewers, R.E. Schaak, Direct solution synthesis of intermetallic AuCu and AuCu3 nanocrystals and nanowire networks, Chem. Mater. 17 (2005) 758–766. doi:10.1021/cm0484450.

[77] R. Koch, G. Li, S. Pandey, S. Phillpot, H. Wang, S.T. Misture, Thermally induced transformations of Au@Cu $_2$ O core–shell nanoparticles into Au–Cu nanoparticles from temperature-programmed *in situ* powder X-ray diffraction, J. Appl. Crystallogr. 52 (2019) 1–8. doi:10.1107/S1600576719004497.

[78] G.G. Li, M. Sun, E. Villarreal, S. Pandey, S.R. Phillpot, H. Wang, Galvanic Replacement-Driven Transformations of Atomically Intermixed Bimetallic Colloidal Nanocrystals : Effects of Compositional Stoichiometry and Structural Ordering, Langmuir. 34 (2018) 4340–4350. doi:10.1021/acs.langmuir.8b00448.

[79] J. Erlebacher, M.J. Aziz, A. Karma, N. Dimitrov, K. Sieradzki, Evolution of nanoporosity in dealloying, Nature. 410 (2001) 450–453.

[80] H. Nakajima, The Discovery and Acceptance of the Kirkendall Effect: The Result of a Short Research Career, JOM. 49 (1997) 15–19. doi:https://doi.org/10.1007/BF02914706.

[81] W. Ostwald, Lehrbuch der Allgemeinen Chemie, vol. 2, part 1, Leipzig, Germany, 1896.

[82] G. Kresse, J. Hafner, Ab initio molecular dynamics for liquid metals, Phys. Rev. B. 47 (1993) 558–561. doi:10.1103/PhysRevB.47.558.

[83] G. Kresse, J. Furthmüller, Efficient iterative schemes for ab initio total-energy calculations using a plane-wave basis set, Phys. Rev. B - Condens. Matter Mater. Phys. 54 (1996) 11169–11186. doi:10.1103/PhysRevB.54.11169.

[84] D. Joubert, From ultrasoft pseudopotentials to the projector augmented-wave method, Phys. Rev. B - Condens. Matter Mater. Phys. 59 (1999) 1758–1775. doi:10.1103/PhysRevB.59.1758.

[85] M. Sanati, L.G. Wang, A. Zunger, Adaptive Crystal Structures : CuAu and NiPt, Phys. Rev. Lett. 90 (2003). doi:10.1103/PhysRevLett.90.045502.

[86] Y. Zhang, G. Kresse, C. Wolverton, Nonlocal First-Principles Calculations in Cu-Au and Other Intermetallic Alloys, Phys. Rev. Lett. 112 (2014). doi:10.1103/PhysRevLett.112.075502.

[87] D.A. Andersson, S.I. Simak, Monovacancy and divacancy formation and migration in copper: A first-principles theory, Phys. Rev. B - Condens. Matter Mater. Phys. 70 (2004) 1–7. doi:10.1103/PhysRevB.70.115108.

[88] Y. Mishin, M.J. Mehl, D.A. Papaconstantopoulos, A.F. Voter, J.D. Kress, Structural stability and lattice defects in copper: Ab initio, tight-binding, and embedded-atom calculations, Phys. Rev. B - Condens. Matter Mater. Phys. 63 (2001) 2241061–22410616. doi:10.1103/PhysRevB.63.224106.

[89] H.J. Monkhorst, J.D. Pack, Special points for Brillouin-zone integrations, Phys. Rev. B. 13 (1976) 5188–5192. doi:https://doi.org/10.1103/PhysRevB.13.5188.

[90] M. Methfessel, A. Paxton, High-precision sampling for Brillouin-zone integration in metals, 40 (1989) 3616–3621. doi:https://doi.org/10.1103/PhysRevB.40.3616.

[91] M.P. Teter, M.C. Payne, D.C. Allan, Solution of Schrodinger's equation for large systems, Phys. Rev. B. 40 (1989) 12255–12263. doi:10.1103/PhysRevB.40.12255.

[92] D.M. Bylander, L. Kleinman, S. Lee, Self-consistent calculations of the energy bands and bonding properties of B12C3, Phys. Rev. B. 42 (1990) 1394–1403. doi:10.1103/PhysRevB.42.1394.

[93] G. Henkelman, H. Jónsson, Improved tangent estimate in the nudged elastic band method for finding minimum energy paths and saddle points, J. Chem. Phys. 113 (2000). doi:10.1063/1.1323224.

[94] G. Henkelman, B.P. Uberuaga, H. Jónsson, G. Henkelman, A climbing image nudged elastic band method for finding saddle points and minimum energy paths, J. Chem. Phys. 113 (2000). doi:10.1063/1.1329672.

[95] H. Okamoto, D.J. Chakrabartl, D.E. Laughlin, T.B. Masselski, The Au-Cu (Gold-Copper) System, J. Phase Equilibria. 8 (1987) 454–474. doi:https://doi.org/10.1007/BF02893155.

[96] L. Tian, H. Levämäki, M. Ropo, K. Kokko, Á. Nagy, L. Vitos, Exchange-Correlation Catastrophe in Cu-Au : A Challenge for Semilocal Density Functional Approximations, 066401 (2016) 1–5. doi:10.1103/PhysRevLett.117.066401.

[97] T. Hoshino, N. Papanikolaou, R. Zeller, P.. Dederichs, M. Asato, T. Asada, N. Stefanou, First-principles calculations for vacancy formation energies in Cu and Al ; non-local e € ect beyond the LSDA and lattice distortion, Comput. Mater. Sci. 14 (1999) 56–61. doi:10.1016/S0927-0256(98)00072-X.

[98] T. Hehenkamp, Absolute vacancy concentrations in noble metals and some of their alloys, J. Phys. Chem. Solids. 55 (1994) 907–915. doi:10.1016/0022-3697(94)90110-4.

[99] R.. Siegel, Vacancy concentrations in metals, J. Nucl. Mater. 69–70 (1978) 117–146. doi:10.1016/0022-3115(78)90240-4.

[100] G. Neumann, V. Tölle, C. Tuijn, Monovacancies and divacancies in copper, Phys. B Condens. Matter. 271 (2002) 21–27. doi:10.1016/s0921-4526(99)00209-4.

[101] Q. Han, Z. Zhou, Y. Ma, Y. Liu, A comparative investigation of the behaviors of H in Au and Ag from first principles A comparative investigation of the behaviors of H in Au and Ag from first principles, Model. Simul. Mater. Sci. Eng. 24 (2016). doi:10.1088/0965-0393/24/4/045009.

[102] N. Lam, L. Dagens, N. Doan, Calculations of the properties of self-interstitials and vacancies in the face-centred cubic metals Cu, Ag and Au, J. Phys. F Met. Phys. (1983) 2503–2516. doi:doi.org/10.1088/0305-4608/13/12/009.

[103] E.A. Dolgopolova, O.A. Ejegbavwo, C.R. Martin, M.D. Smith, W. Setyawan, S.G. Karakalos, C.H. Henager, H.C. Zur Loye, N.B. Shustova, Multifaceted Modularity: A Key for Stepwise Building of Hierarchical Complexity in Actinide Metal-Organic Frameworks, J. Am. Chem. Soc. 139 (2017) 16852–16861. doi:10.1021/jacs.7b09496.

[104] L. Zhu, D. Sheng, C. Xu, X. Dai, M.A. Silver, J. Li, P. Li, Y. Wang, Y. Wang, L. Chen, C. Xiao, J. Chen, R. Zhou, C. Zhang, O.K. Farha, Z. Chai, T.E. Albrecht-Schmitt, S. Wang, Identifying the Recognition Site for Selective Trapping of99TcO4-in a Hydrolytically Stable and Radiation Resistant Cationic Metal-Organic Framework, J. Am. Chem. Soc. 139 (2017) 14873–14876. doi:10.1021/jacs.7b08632.

[105] V. Stavila, A.A. Talin, M.D. Allendorf, MOF-based electronic and opto-electronic devices, Chem. Soc. Rev. 43 (2014) 5994–6010. doi:10.1039/c4cs00096j.

[106] H.-C. Zhou, J.R. Long, O.M. Yaghi, Introduction to Metal–Organic Frameworks, Chem. Rev. 112 (2012) 673–674. doi:10.1021/cr300014x.

[107] Y. He, W. Zhou, G. Qian, B. Chen, Methane storage in metal–organic frameworks, Chem. Soc. Rev. 43 (2014) 5657–5678. doi:10.1039/c4cs00032c.

[108] D.E. Williams, N.B. Shustova, Metal-Organic Frameworks as a Versatile Tool to Study and Model Energy Transfer Processes, Chem. - A Eur. J. 21 (2015) 15474–15479. doi:10.1002/chem.201502334.

[109] E.A. Dolgopolova, N.B. Shustova, Metal-organic framework photophysics: Optoelectronic devices, photoswitches, sensors, and photocatalysts, MRS Bull. 41 (2016) 890–895. doi:10.1557/mrs.2016.246.

[110] O.A. Ejegbavwo, C.R. Martin, O.A. Olorunfemi, G.A. Leith, R.T. Ly, A.M. Rice, E.A. Dolgopolova, M.D. Smith, S.G. Karakalos, N. Birkner, B.A. Powell, S. Pandey, R.J. Koch, S.T. Misture, H.-C. zur Loye, S.R. Phillpot, K.S. Brinkman, N.B. Shustova, Thermodynamics and Electronic Properties of Heterometallic Multinuclear Actinide-Containing Metal–Organic Frameworks with “Structural Memory,” J. Am. Chem. Soc. 141 (2019) 11628–11640. doi:10.1021/jacs.9b04737.

[111] D. Sheng, L. Zhu, X. Dai, C. Xu, P. Li, C.I. Pearce, C. Xiao, J. Chen, R. Zhou, T. Duan, O.K. Farha, Z. Chai, S. Wang, Successful Decontamination of 99 TcO 4− in Groundwater at Legacy Nuclear Sites by a Cationic Metal-Organic Framework with Hydrophobic Pockets, Angew. Chemie - Int. Ed. 58 (2019) 4968–4972. doi:10.1002/anie.201814640.

[112] J. Zhang, L. Chen, X. Dai, L. Zhu, C. Xiao, L. Xu, Z. Zhang, E. V. Alekseev, Y. Wang, C. Zhang, H. Zhang, Y. Wang, J. Diwu, Z. Chai, S. Wang, Distinctive Two-Step Intercalation of Sr 2+ into a Coordination Polymer with Record High 90 Sr Uptake Capabilities, Chem. 5 (2019) 977–994. doi:10.1016/j.chempr.2019.02.011.

[113] W. Liu, X. Dai, Z. Bai, Y. Wang, Z. Yang, L. Zhang, L. Xu, L. Chen, Y. Li, D. Gui, J. Diwu, J. Wang, R. Zhou, Z. Chai, S. Wang, Highly Sensitive and Selective Uranium Detection in Natural Water Systems Using a Luminescent Mesoporous Metal-Organic Framework Equipped with Abundant Lewis Basic Sites: A Combined Batch, X-ray Absorption Spectroscopy, and First Principles Simulation Inv, Environ. Sci. Technol. 51 (2017) 3911–3921. doi:10.1021/acs.est.6b06305.

[114] S. Yuan, W. Lu, Y.P. Chen, Q. Zhang, T.F. Liu, D. Feng, X. Wang, J. Qin, H.C. Zhou, Sequential linker installation: Precise placement of functional groups in multivariate metal-organic frameworks, J. Am. Chem. Soc. 137 (2015) 3177–3180. doi:10.1021/ja512762r.

[115] J. Sun, M. Marsman, G.I. Csonka, A. Ruzsinszky, P. Hao, Y.S. Kim, G. Kresse, J.P. Perdew, Self-consistent meta-generalized gradient approximation within the projector-augmented-wave method, Phys. Rev. B - Condens. Matter Mater. Phys. 84 (2011) 1–12. doi:10.1103/PhysRevB.84.035117.

[116] S. Grimme, J. Antony, S. Ehrlich, H. Krieg, A consistent and accurate ab initio parametrization of density functional dispersion correction (DFT-D) for the 94 elements H-Pu, J. Chem. Phys. 132 (2010). doi:10.1063/1.3382344.

[117] S. Grimme, S. Ehrlich, L. Goerigk, Effect of the Damping Function in Dispersion Corrected Density Functional Theory, J. Comput. Chem. 32 (2011) 1456–1465. doi:https://doi.org/10.1002/jcc.21759.

[118] H. Peng, Z.H. Yang, J.P. Perdew, J. Sun, Versatile van der Waals density functional based on a meta-generalized gradient approximation, Phys. Rev. X. 6 (2016) 1–15. doi:10.1103/PhysRevX.6.041005.

[119] G. Henkelman, A. Arnaldsson, H. Jónsson, A fast and robust algorithm for Bader decomposition of charge density, Comput. Mater. Sci. 36 (2006) 354–360. doi:10.1016/j.commatsci.2005.04.010.

[120] E. Sanville, S.D. Kenny, R. Smith, G. Henkelman, Improved Grid-Based Algorithm for Bader Charge Allocation, J. Comput. Chem. 28 (2007) 899–908. doi:10.1002/jcc.20575.

[121] W. Tang, E. Sanville, G. Henkelman, A grid-based Bader analysis algorithm without lattice bias, J. Phys. Condens. Matter. 21 (2009). doi:10.1088/0953-8984/21/8/084204.

[122] M. Yu, D.R. Trinkle, Accurate and efficient algorithm for Bader charge integration, J. Chem. Phys. 134 (2011) 1–8. doi:10.1063/1.3553716.

[123] B.B. Owen, R.C. Miller, C.E. Milner, H.L. Cogan, The Dielectric Constant of Water as a function of Temperature And Pressure 1,2, J. Phys. Chem. 65 (1961) 2065–2070. doi:10.1021/j100828a035.

[124] G. Makov, R. Shah, M. Payne, Periodic boundary conditions in ab initio calculations. II. Brillouin-zone sampling for aperiodic systems, Phys. Rev. B - Condens. Matter Mater. Phys. 53 (1996) 15513–15517. doi:10.1103/PhysRevB.53.15513.

[125] M. Eddaoudi, D.B. Moler, H. Li, B. Chen, T.M. Reineke, M. O'Keeffe, O.M. Yaghi, Modular chemistry: secondary building units as a basis for the design of highly porous and robust metal-organic carboxylate frameworks., Acc. Chem. Res. 34 (2001) 319–30. doi:10.1021/ar000034b.

[126] S. Schwalbe, K. Trepte, G. Seifert, J. Kortus, Screening for high-spin metal organic frameworks (MOFs): Density functional theory study on DUT-8(M1,M2) (with Mi = V,...,Cu), Phys. Chem. Chem. Phys. 18 (2016) 8075–8080. doi:10.1039/c5cp07662e.

[127] M.J. Kalmutzki, N. Hanikel, O.M. Yaghi, Secondary building units as the turning point in the development of the reticular chemistry of MOFs, Sci. Adv. 4 (2018) eaat9180. doi:10.1126/sciadv.aat9180.

[128] M.J. Frisch, G.W. Trucks, H.B. Schlegel, G.E. Scuseria, M.A. Robb, J.R. Cheeseman, G. Scalmani, V. Barone, B. Mennucci, G.A. Petersson, H. Nakatsuji, M. Caricato, X. Li, Gaussian 09, (2009) 2009.

[129] D.A. Pantazis, F. Neese, All-electron scalar relativistic basis sets for the 6p elements, Theor. Chem. Acc. 131 (2012) 1–7. doi:10.1007/s00214-012-1292-x.

[130] A.R. Puigdollers, F. Illas, G. Pacchioni, Structure and Properties of Zirconia Nanoparticles from Density Functional Theory Calculations, J. Phys. Chem. C. 120 (2016) 4392–4402. doi:10.1021/acs.jpcc.5b12185.

[131] Y. Yun, J. Rusz, M.T. Suzuki, P.M. Oppeneer, First-principles investigation of higher oxides of uranium and neptunium: U3O8 and Np2O5, Phys. Rev. B - Condens. Matter Mater. Phys. 83 (2011) 1–10. doi:10.1103/PhysRevB.83.075109.

[132] N.A. Brincat, S.C. Parker, M. Molinari, G.C. Allen, M.T. Storr, Density functional theory investigation of the layered uranium oxides U_3O_8 and U_2O_5, Dalt. Trans. 44 (2015) 2613–2622. doi:10.1039/C4DT02493A.

[133] B.T. Wang, H. Shi, W.D. Li, P. Zhang, First-principles study of ground-state properties and high pressure behavior of ThO2, J. Nucl. Mater. 399 (2010) 181–188. doi:10.1016/j.jnucmat.2010.01.017.

[134] R.D. Shannon, Revised Effective Ionic Radii and Systematic Studies of Interatomic Distances in Halides and Chalcogenides, Acta. Cryst. 32 (1976) 751–767.

[135] B. Dorado, G. Jomard, M. Freyss, M. Bertolus, Stability of oxygen point defects in UO2 by first-principles DFT+U calculations: Occupation matrix control and Jahn-Teller distortion, Phys. Rev. B - Condens. Matter Mater. Phys. 82 (2010) 1–11. doi:10.1103/PhysRevB.82.035114.

[136] B. Dorado, B. Amadon, M. Freyss, M. Bertolus, DFT+U calculations of the ground state and metastable states of uranium dioxide, Phys. Rev. B - Condens. Matter Mater. Phys. 79 (2009) 1–8. doi:10.1103/PhysRevB.79.235125.

[137] J.T. Pegg, X. Aparicio-Anglès, M. Storr, N.H. de Leeuw, DFT+U study of the structures and properties of the actinide dioxides, J. Nucl. Mater. 492 (2017) 269–278. doi:10.1016/j.jnucmat.2017.05.025.

[138] H.R. Fuh, Y.P. Liu, Z.R. Xiao, Y.K. Wang, New type of ferromagnetic insulator: Double perovskite La2NiMO6(M=Mn, Tc, Re, Ti, Zr, and Hf)., J. Magn. Magn. Mater. 357 (2014) 7–12. doi:10.1016/j.jmmm.2013.12.049.

[139] M. Pavlov, P.E.M. Siegbahn, M. Sandström, Hydration of beryllium, magnesium, calcium, and zinc ions using density functional theory, J. Phys. Chem. A. 102 (1998) 219–228. doi:10.1021/jp972072r.

[140] C. Xiao, M.A. Silver, S. Wang, Metal-organic frameworks for radionuclide sequestration from aqueous solution: A brief overview and outlook, Dalt. Trans. 46 (2017) 16381–16386. doi:10.1039/c7dt03670a.

[141] C.T. Lollar, J. Pang, J.S. Qin, S. Yuan, J.A. Powell, H.C. Zhou, Thermodynamically Controlled Linker Installation in Flexible Zirconium Metal-Organic Frameworks, Cryst. Growth Des. 19 (2019) 2069–2073. doi:10.1021/acs.cgd.8b01637.

[142] M.W. Logan, J.D. Adamson, D. Le, F.J. Uribe-Romo, Structural Stability of N-Alkyl-Functionalized Titanium Metal-Organic Frameworks in Aqueous and Humid Environments, ACS Appl. Mater. Interfaces. 9 (2017) 44529–44533. doi:10.1021/acsami.7b15045.

[143] E.A. Dolgopolova, A.J. Brandt, O.A. Ejegbavwo, A.S. Duke, T.D. Maddumapatabandi, R.P. Galhenage, B.W. Larson, O.G. Reid, S.C. Ammal, A. Heyden, M. Chandrashekhar, V. Stavila, D.A. Chen, N.B. Shustova, Electronic Properties of Bimetallic Metal-Organic Frameworks (MOFs): Tailoring the Density of Electronic States through MOF Modularity, J. Am. Chem. Soc. 139 (2017) 5201–5209. doi:10.1021/jacs.7b01125.

[144] B. Pattengale, D.J. Santalucia, S. Yang, W. Hu, C. Liu, X. Zhang, J.F. Berry, J. Huang, Direct Observation of Node-to-Node Communication in Zeolitic Imidazolate Frameworks, J. Am. Chem. Soc. 140 (2018) 11573–11576. doi:10.1021/jacs.8b06727.

[145] H.Q. Pham, T. Mai, N.N. Pham-Tran, Y. Kawazoe, H. Mizuseki, D. Nguyen-Manh, Engineering of band gap in metal-organic frameworks by functionalizing organic linker: A systematic density functional theory investigation, J. Phys. Chem. C. 118 (2014) 4567–4577. doi:10.1021/jp405997r.

[146] S. Pandey, Z. Jia, B. Demaske, O.A. Ejegbavwo, W. Setyawan, C.H. Henager, N. Shustova, S.R. Phillpot, Sequestration of Radionuclides in Metal-Organic Frameworks from Density Functional Theory Calculations, J. Phys. Chem. C. 123 (2019) 26842–26855. doi:10.1021/acs.jpcc.9b08256.

[147] A. V. Krukau, O.A. Vydrov, A.F. Izmaylov, G.E. Scuseria, Influence of the exchange screening parameter on the performance of screened hybrid functionals, J. Chem. Phys. 125 (2006). doi:10.1063/1.2404663.

[148] R. Ditchfield, W.J. Hehre, J.A. Pople, Self-Consistent Molecular-Orbital Methods. IX. An Extended Gaussian-Type Basis for Molecular-Orbital Studies of Organic Molecules, J. Chem. Phys. 54 (1971) 724–728. doi:10.1063/1.1674902.

[149] W.J. Hehre, R. Ditchfield, J.A. Pople, Self — Consistent Molecular Orbital Methods . XII . Further Extensions of Gaussian — Type Basis Sets for Use in Molecular Orbital Studies of Organic Molecules Published by the AIP Publishing Articles you may be interested in Self - consistent molecular or, 2257 (1977). doi:10.1063/1.1677527.

[150] V.A. Rassolov, M.A. Ratner, J.A. Pople, P.C. Redfern, L.A. Curtiss, 6-31G* basis set for third-row atoms, J. Comput. Chem. 22 (2001) 976–984. doi:10.1002/jcc.1058.

[151] W. Küchle, M. Dolg, H. Stoll, H. Preuss, Energy-adjusted pseudopotentials for the actinides. Parameter sets and test calculations for thorium and thorium monoxide, J. Chem. Phys. 100 (1994) 7535–7542. doi:10.1063/1.466847.

[152] D. Andrae, U. Häußermann, M. Dolg, H. Stoll, H. Preuß, Energy-adjusted ab initio pseudopotentials for the second and third row transition elements, Theor. Chim. Acta. 77 (1990) 123–141. doi:10.1007/BF01114537.

[153] X. Cao, M. Dolg, H. Stoll, Valence basis sets for relativistic energy-consistent small-core actinide pseudopotentials, J. Chem. Phys. 118 (2003) 487–496. doi:10.1063/1.1521431.

[154] M. Boujnah, H. Labrim, K. Allam, A. Belhaj, A. Benyoussef, A. El Kenz, B. Belhorma, A. El Bouari, Magnetic and electronic properties of point defects in ZrO2, J. Supercond. Nov. Magn. 26 (2013) 2429–2434. doi:10.1007/s10948-012-1826-4.

[155] J. Yu, R. Devanathan, W.J. Weber, First-principles study of defects and phase transition in UO2, J. Phys. Condens. Matter. 21 (2009). doi:10.1088/0953-8984/21/43/435401.

[156] L. Pauling, The chemical bond; a brief introduction to modern structural chemistry, Cornell University Press, Ithaca, N.Y., 1967.

[157] Y. Fu, D.J. Singh, Applicability of the Strongly Constrained and Appropriately Normed Density Functional to Transition-Metal Magnetism, Phys. Rev. Lett. 121 (2018) 207201. doi:10.1103/PhysRevLett.121.207201.

[158] I. Rudra, Q. Wu, T. Van Voorhis, Predicting exchange coupling constants in frustrated molecular magnets using density functional theory, Inorg. Chem. 46 (2007) 10539–10548. doi:10.1021/ic700871f.

[159] F. Tran, J. Stelzl, P. Blaha, Rungs 1 to 4 of DFT Jacob's ladder: Extensive test on the lattice constant, bulk modulus, and cohesive energy of solids, J. Chem. Phys. 144 (2016). doi:10.1063/1.4948636.

[160] Y. Zhang, D.A. Kitchaev, J. Yang, T. Chen, S.T. Dacek, R.A. Sarmiento-Pérez, M.A.L. Marques, H. Peng, G. Ceder, J.P. Perdew, J. Sun, Efficient first-principles prediction of solid stability: Towards chemical accuracy, Npj Comput. Mater. 4 (2018). doi:10.1038/s41524-018-0065-z.

[161] X.D. Wen, R.L. Martin, L.E. Roy, G.E. Scuseria, S.P. Rudin, E.R. Batista, T.M. McCleskey, B.L. Scott, E. Bauer, J.J. Joyce, T. Durakiewicz, Effect of spin-orbit coupling on the actinide dioxides AnO 2 (An=Th, Pa, U, Np, Pu, and Am): A screened hybrid density functional study, J. Chem. Phys. 137 (2012). doi:10.1063/1.4757615.

[162] H. He, D.A. Andersson, D.D. Allred, K.D. Rector, Determination of the insulation gap of uranium oxides by spectroscopic ellipsometry and density functional theory, J. Phys. Chem. C. 117 (2013) 16540–16551. doi:10.1021/jp401149m.

[163] C. Mo, Y. Yang, W. Kang, P. Zhang, Electronic and optical properties of (U,Th)O2 compound from screened hybrid density functional studies, Phys. Lett. Sect. A Gen. At. Solid State Phys. 380 (2016) 1481–1486. doi:10.1016/j.physleta.2016.02.020.

[164] O.M. Yaghi, Reticular Chemistry - Construction, Properties, and Precision Reactions of Frameworks, J. Am. Chem. Soc. 138 (2016) 15507–15509. doi:10.1021/jacs.6b11821.

[165] M.D. Allendorf, A. Schwartzberg, V. Stavila, A.A. Talin, A roadmap to implementing metal-organic frameworks in electronic devices: Challenges and critical directions, Chem. - A Eur. J. 17 (2011) 11372–11388. doi:10.1002/chem.201101595.

[166] L. Sun, M.G. Campbell, M. Dinca, Electrically Conductive Porous Metal-Organic Frameworks, Angew. Chemie - Int. Ed. 55 (2016) 3566–3579. doi:10.1002/anie.201506219.

[167] M. Kim, J.F. Cahill, H. Fei, K.A. Prather, S.M. Cohen, Postsynthetic Ligand and Cation Exchange in Robust Metal-Organic Frameworks, J. Am. Chem. Soc. 134 (2012) 18082–18088. doi:10.1021/ja3079219.

[168] P. Deria, J.E. Mondloch, O. Karagiaridi, W. Bury, J.T. Hupp, O.K. Farha, Beyond post-synthesis modification: Evolution of metal-organic frameworks via building block replacement, Chem. Soc. Rev. 43 (2014) 5896–5912. doi:10.1039/c4cs00067f.

[169] M. Natali, S. Giordani, Molecular switches as photocontrollable “smart” receptors, Chem. Soc. Rev. 41 (2012) 4010–4029. doi:10.1039/c2cs35015g.

[170] M.C. Walkey, L.T. Byrne, M.J. Piggott, P.J. Low, G.A. Koutsantonis, Enhanced bi-stability in a ruthenium alkynyl spiropyran complex, Dalt. Trans. 44 (2015) 8812–8815. doi:10.1039/c5dt01107h.

[171] H. Görner, Photochromism of nitrospiropyrans: Effects of structure, solvent and temperature, Phys. Chem. Chem. Phys. 3 (2001) 416–423. doi:10.1039/b007708i.

[172] S.A. Dar, V. Srivastava, U.K. Sakalle, A First-Principles Calculation on Structural, Electronic, Magnetic, Mechanical, and Thermodynamic Properties of SrAmO3, J. Supercond. Nov. Magn. 30 (2017) 3055–3063. doi:10.1007/s10948-017-4155-9.

[173] C. Felser, G.H. Fecher, B. Balke, Spintronics: A challenge for materials science and solid-state chemistry, Angew. Chemie - Int. Ed. 46 (2007) 668–699. doi:10.1002/anie.200601815.

[174] H. Zhu, J. Mao, Y. Li, J. Sun, Y. Wang, Q. Zhu, G. Li, Q. Song, J. Zhou, Y. Fu, R. He, T. Tong, Z. Liu, W. Ren, L. You, Z. Wang, J. Luo, A. Sotnikov, J. Bao, K. Nielsch, G. Chen, D.J. Singh, Z. Ren, Discovery of TaFeSb-based half-Heuslers with high thermoelectric performance, Nat. Commun. 10 (2019) 1–8. doi:10.1038/s41467-018-08223-5.

[175] M.A. Sattar, S.A. Ahmad, F. Hussain, C. Cazorla, First-principles prediction of magnetically ordered half-metals above room temperature, J. Mater. 5 (2019) 404–412. doi:10.1016/j.jmat.2019.04.003.

[176] S.P. Dash, S. Sharma, R.S. Patel, M.P. De Jong, R. Jansen, Electrical creation of spin polarization in silicon at room temperature, Nature. 462 (2009) 491–494. doi:10.1038/nature08570.

[177] S.G. Bhat, P.S. Anil Kumar, Demonstration of efficient spin injection and detection in various systems using Fe3O4 based spin injectors, AIP Adv. 6 (2016). doi:10.1063/1.4944346.

BIOGRAPHICAL SKETCH

Shubham Pandey was born in Bhopal, Madhya Pradesh, India. He received his Bachelor of Technology in Materials Science and Metallurgical Engineering from Maulana Azad National Institute of Technology, Bhopal, in 2015. He joined Department of Materials Science and Engineering at University of Florida, in August 2015 and began his Ph.D. under supervision of Prof. Simon R. Phillpot in January 2017. Before beginning his Ph.D., Shubham also worked as a master's volunteer with Prof. Phillpot throughout the Summer and Fall semesters of 2016. He received his Master of Science from the University of Florida in May 2017. During his doctoral research he primarily worked on the EFRC project of Center for Hierarchical Wasteform Materials (CHWM), centered at University of South Carolina, on the project of nuclear waste sequestration. In May 2020, he graduated from UF with a Ph.D. in Materials Science and Engineering.